HIGH-HARMONIC GENERATION WITH LAGUERRE-GAUSSIAN BEAMS

Dissertation
zur Erlangung des akademischen Grades
doctor rerum naturalium (Dr. rer. nat.)

vorgelegt dem Rat der Physikalisch-Astronomischen Fakultät
der Friedrich-Schiller-Universität Jena

von Willi Paufler
geboren am 06.11.1991 in Lichtenstein

GUTACHTER:

1. Prof. Dr. Stephan Fritzsche
   Friedrich-Schiller-Universität Jena
2. Prof. Dr. Jan-Michael Rost
   Technische Universität Dresden
3. Prof. Dr. Andrey Surzhykov
   Technische Universität Braunschweig

Tag der Disputation: 28. Mai 2020

If people sat outside and
looked at the stars each night,
I’ll bet they’d live a lot differently.

— Bill Watterson

KURZFASSUNG

Die Erzeugung hoher Harmonischer ist ein vielseitig nutzbarer Prozess, der einerseits atomare und molekulare Strukturen während der Erzeugung selbst untersucht und andererseits eine Quelle heller, kurzer sowie kohärenter, extrem-ultravioletter Strahlung ist. Hierbei kann die harmonische Strahlung durch die Form des antreibenden Lasers hinsichtlich ihrer Polarisation oder Frequenzen kontrolliert werden. Die neusten Fortschritte zeigen, dass Laguerre-Gaußsche Strahlen, die zusätzlich zu ihrem Spin- auch Bahndrehimpuls tragen, ebenso für die Erzeugung hoher Harmonischer genutzt werden können.

In der vorliegenden Arbeit analysieren wir die Erzeugung hoher Harmonischer mit Laguerre-Gaußschen Strahlen im Rahmen der Starkfeld-Approximation und zeigen, dass hierzu sowohl die Betrachtung der Wechselwirkung eines einzelnen Atoms mit dem antreibenden Laser sowie die Überlagerung aller Beiträge der einzelnen Atome notwendig ist.

Zunächst untersuchen wir die Erzeugung hoher Harmonischer mit linear polarisierten Laguerre-Gaußschen Strahlen. Wir zeigen, wie der Bahndrehimpuls des antreibenden Lasers auf die erzeugten Harmonischen übertragen wird. Hierzu haben wir anschauliche Photonendiagramme entwickelt, um die Erhaltung des Bahndrehimpulses darzustellen. Im Anschluss untersuchen wir die Phasenanpassung der erzeugten Harmonischen, um die Umwandlungseffizienz zu erhöhen. Wir betrachten dazu insbesondere die Kohärenzlänge an verschiedenen Positionen des erzeugenden Lasers. Wir zeigen zum Beispiel, dass die Kohärenzlänge vor dem Fokus größer ist als hinter dem Fokus des Lasers.

Des weiteren untersuchen wir die Erzeugung hoher Harmonischer mit einem Paar von gegenläufig zirkular polarisierten Laguerre-Gaußschen Strahlen. Dazu leiten wir Auswahlregeln her, die die Energieerhaltung sowie die Erhaltung des Spin- und Bahndrehimpulses berücksichtigen. Zusätzlich zeigen wir, dass der Bahndrehimpuls der erzeugten Harmonischen genau durch den Bahndrehimpuls des erzeugenden Lasers kontrolliert werden kann. Zum Schluss betrachten wir die zeitliche Entwicklung der hohen Harmonischen und zeigen, dass hierbei helikale Lichtfedern geformt werden und erklären wie Parameter der Lichtfedern, wie beispielsweise die Anzahl der Windungen, kontrolliert werden können.

ABSTRACT

High-harmonic generation is a versatile process, for one thing useful to explore the structure of atoms or molecules during the generation itself and apart from that a source of bright, short, coherent extreme ultraviolet radiation. Thereby the harmonic radiation can be controlled by the shape of the driving laser with respect to its polarization or frequencies. Recent advances show that Laguerre-Gaussian beams, which carry in addition to their spin also orbital angular momentum, can be utilized for high-harmonic generation.

In this thesis, we analyze high-harmonic generation with Laguerre-Gaussian beams in the framework of the strong-field approximation and show that this requires both the interaction of a single atom with the driving laser and the macroscopic superposition of all single atom contributions.

We first investigate high-harmonic generation with linearly polarized Laguerre-Gaussian beams. There, we show how the orbital angular momentum of the driving laser is transferred to the generated harmonics. Here, we developed vivid photon diagrams to explain the conservation of orbital angular momentum. We then consider phase matching of the generated radiation in order to increase the conversion efficiency. In particular, we analyze the coherence length at different positions in the generating beam. We show, for example, that the coherence length is increased if the target is placed behind the focus plane compared to a target before the focus plane.

Furthermore, we investigate high-harmonic generation with a pair of counter-rotating circularly polarized Laguerre-Gaussian beams. Here, we derive selection rules that take account of the conservation of energy, spin and orbital angular momentum. In addition, we show that the orbital angular momentum of the generated harmonics can be precisely controlled by the orbital angular momentum of the driving beam. Finally, we investigate the temporal evolution of the high-harmonic signal, and show that it forms helical light springs. We also explain how to control parameters of the light spring, such as the number of coils.

CONTENTS

1 INTRODUCTION 1
  1.1 A brief history of attosecond physics 1
  1.2 The orbital angular momentum of light 3
  1.3 Short overview of the thesis 4
2 TWISTED LIGHT BEAMS 7
  2.1 Plane waves 7
  2.2 Paraxial approximation 8
    2.2.1 Gaussian beams 9
    2.2.2 Laguerre-Gaussian beams 10
    2.2.3 Divergence of Laguerre-Gaussian beams 11
3 THEORETICAL APPROACH TO HIGH-HARMONIC GENERATION 15
  3.1 Microscopic picture 15
    3.1.1 Multiphoton and tunnel ionization 15
    3.1.2 Simple-man's model 16
    3.1.3 Semi-classical aspects of HHG 17
    3.1.4 Lewenstein model 21
    3.1.5 Quantum orbit approach 27
  3.2 Macroscopic picture 29
    3.2.1 Fraunhofer diffraction 30
    3.2.2 Numerical propagation of the emitted radiation 30
4 HIGH-HARMONIC GENERATION WITH LINEARLY POLARIZED LAGUERRE-GAUSSIAN BEAMS 33
  4.1 Single atom response to a linearly polarized field 33
  4.2 Extended targets in linearly polarized LG beams 36
    4.2.1 Conservation of OAM 36
    4.2.2 Divergence of the harmonics 37
  4.3 Phase Matching 38
    4.3.1 Dipole phase 42
    4.3.2 Intrinsic beam phases 43
    4.3.3 Phase matching on maximum 45
    4.3.4 Transverse and longitudinal phase matching 52
  4.4 Controlling the OAM of harmonics by multi mode HHG 55
5 HIGH-HARMONIC GENERATION WITH BICIRCULAR LAGUERRE-GAUSSIAN BEAMS 59

5.1 High-harmonic generation in circularly polarized fields 59
5.2 Bicircular modes 60
5.2.1 Composition of bicircular modes 60
5.2.2 Symmetries in bicircular LG modes 60
5.3 Single atom response to a bicircular field 64
5.4 Extended targets in bicircular LG beams 67
5.4.1 Conservation of SAM and OAM 67
5.4.2 Tailored OAM 71
5.4.3 Generalization to $r\omega + s\omega$ 73
5.5 Generation of near-circularly polarized attosecond pulse trains 73
5.5.1 Spatial separation with OAM 75
5.5.2 Relative intensity ratio and polarization control 76
5.6 Attosecond light springs in HHG 78
6 SUMMARY AND CONCLUSIONS 85

BIBLIOGRAPHY i
LIST OF FIGURES xi
ACRONYMS xiii
PUBLICATIONS xv
DECLARATION xvii

1

INTRODUCTION

1.1 A BRIEF HISTORY OF ATTOSECOND PHYSICS

It has always been fascinating for people to keep memories in terms of pictures. In early times the only possibility was to paint or draw pictures. A big step was made in 1822 when Joseph Nicéphore Niépce successfully took photographs with his camera obscura. However, it was only possible to take photographs of static objects and not of moving animals or people. In order to take photographs of moving objects, it is required to have a small period of exposure. Generally, it must be shorter than the time it takes the object to move a characteristic length. Of course, this length determines the blur of the image.

In 1872, the American governor Leland Stanford requested the photographer Eadweard Muybridge to find out whether a galloping horse is ever completely aloft. Muybridge was able to reduce the period of exposure to less than a tenth of a second and was thus able to resolve this open question with the answer *yes* [1]. One of his photographs is shown in the left part of Fig. 1.1. His success can be seen as the beginning of chronophotography, which terms the photographic documentation of moving objects. Within the last century the exposure times dropped by several orders of magnitude. Nowadays exposure times of about 25 ns are achievable with stroboscope light sources [2] and it is possible to observe and capture motion at this timescales with for example applications in slow motion photography.

But is it possible to capture the motion of an electron? If we consider an electron moving classically on the first Bohr's orbit, it takes about 150 as[1] to travel once around the nucleus, as illustrated in the right part of Fig. 1.1. In order to observe electronic motion it is therefore required to have exposure times in the attosecond range, which means using light pulses that have duration of less than a femtosecond[2].

A typical Titan:sapphire laser has a wavelength of about 800 nm, which corresponds to a cycle length of 2.5 fs [3]. Physically it is not possible to have light pulses that are shorter than one cycle. New light sources were therefore required to observe such ultrafast processes.

---

[1] $1\,\text{as} = 10^{-18}\,\text{s}$

[2] $1\,\text{fs} = 10^{-15}\,\text{s}$

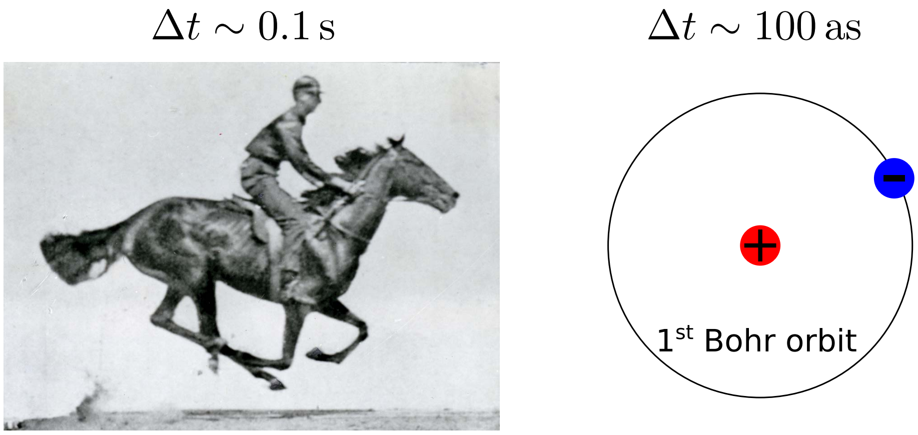
$\Delta t \sim 0.1\,\mathrm{s}$
$\Delta t \sim 100\,\mathrm{as}$
-
+
1st Bohr orbit

Figure 1.1: Left: Horse in motion from [4], which takes place in timescales of approximately a tenth of a second. Right: Illustration of an electron on first Bohr's orbit. Electronic motion usually happens on sub-femtosecond timescales.

In 1987, the first observations of high-harmonic generation (HHG) in rare gases were made [5, 6]. The research group around L'Huillier aimed to observe the fluorescence of excited atoms, whereas they measured that the atoms emitted highly energetic radiation. The frequencies of the radiation were (high) odd multiples of the frequency of the driving laser, which were therefore called odd harmonics. It has been fascinating that many of these harmonics have been emitted at similar intensities over a wide spectral range and form the so-called plateau in HHG [7].
Corkum explained these observations within his simple-man's model: During the short time, where the laser interacts with the atom there is not only single ionization but the electron may also come back to the parent ion, recombine and therefore a high energetic photon is emitted [8]. About one year later the first complete theoretical description of HHG has been provided by Lewenstein and Corkum [9].
At this time, it was not yet known that the emitted radiation forms attosecond pulses. It took another seven years until the group of Ferenc Krausz was able to measure the duration of such a pulse [10]. A single attosecond pulse is generated if the driving infrared pulse is very short, about or less than 5 fs. If the driving beam consists of multiple cycles, a so-called attosecond pulse train is generated [11, 12].
Until the present the HHG reveals a table top source for coherent radiation in the extreme ultraviolet ($10 - 100\,\mathrm{nm}$) and even up to the soft X-Ray regime ($1 - 10\,\mathrm{nm}$) [13]. These pulses can be used to probe matter at fundamental timescales [14–17]. Moreover, multiple studies have proven that the driving infrared beams can be used to control the HHG and therefore have a significant impact on the generated harmonic signal [18–20].

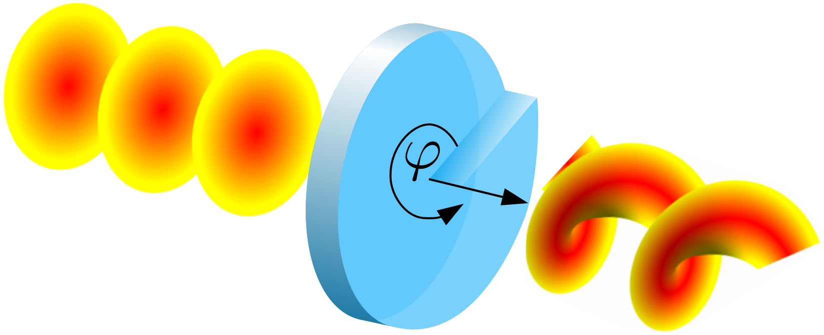

Figure 1.2: Illustration of the generation of twisted light with a spiral phase plate.

1.2 THE ORBITAL ANGULAR MOMENTUM OF LIGHT

It is well known that light, as an electromagnetic wave, carries energy. Often less attention is paid to the different forms of momentum of light. For example, light carries in addition to energy also linear momentum, which becomes apparent in terms of radiation pressure [21, 22].

In the beginning of the 20th century, it was Poynting who came up with the idea that light fields, whose electric field vector is spinning, should have some form of angular momentum [23]. This type of angular momentum was named spin angular momentum (SAM) and is associated with the polarization of the light. In 1936, the angular momentum of light was experimentally detected by Holburn [24] and Beth [25]. Moreover, it was shown that the SAM is quantized, such that the SAM of a single photon can only be $\pm\hbar$, where $\hbar = 1$ in atomic units [26]. Thereby, left circularly polarized light has SAM of $+\hbar$ and right circularly polarized light of $-\hbar$.

Less known is the third form of momentum of light, the orbital angular momentum (OAM). It was a pioneering work by Allen *et al.* that connected an azimuthally varying phase $e^{i\ell\varphi}$ in the electric field to its OAM [27]. This azimuthal phase induces a phase singularity together with a zero intensity region on the beam axis. Moreover, it causes helical phase fronts, which is a fundamental difference to plane wave phase fronts. Due to the helical phase fronts light beams with OAM are often referred to as twisted light or optical vortices.

Nowadays, these beams can be routinely generated in the lab with for example cylindrical mode converters [27], pitchfork holograms [28] or spiral phase plates [29]. The latter one is shown in Fig. 1.2. Here the thickness of the plate varies azimuthally but is radially constant. As the fundamental beam passes through the plate it undergoes a phase-change which introduces the helical phase front.

Twisted light beams paved new ways for light-matter interaction. Recent theoretical and experimental results show that atomic transitions can be induced beyond the plane wave selection rules [30–32].

In addition, the single photon ionization of atoms by twisted light modifies the electron wave packet and gives rise to a large variety of dichroism signals that are different from the the well-known circular dichroism [33, 34].

Furthermore, optical vortices have been used to trap particles [35] or as a tool to detect spinning objects [36] and show potential use in optical telecommunication, so-called OAM multiplexing [37].

The wide range of applications of twisted light beams, indeed stimulated extensive research on the generation of vortex beams up to the extreme ultraviolet region. Within the last years HHG has been found a versatile source of extreme ultraviolet vortex beams, which has also been the ignition key for the work presented in this thesis.

1.3 SHORT OVERVIEW OF THE THESIS

In Ch. 2, we will start with the theoretical description of plane wave light beams, continue with Gaussian beams and finally consider the description of twisted light beams. We here consider a special class of twisted beams, so-called Laguerre-Gaussian (LG) beams.

We devote Ch. 3 to the theory to compute high-harmonic signals. This chapter is subdivided into two parts. In the first part we present HHG on the single atom level. We start with the simple-man's model and some classical considerations. We then continue with the quantum mechanical model for HHG based on the well-know strong-field approximation (SFA). In the second part of this chapter we deal with the coherent nature of HHG. We show how to compute the experimentally measurable signal, which arises from a coherent summation of many single atom contributions.

Then, in Ch. 4, we introduce HHG with linearly polarized LG beams and show that the conservation of OAM is fulfilled. Moreover, we introduce photon diagrams to explain the conservation laws. In particular, we apply these diagrams to more sophisticated scenarios of HHG that arise from the superposition of two LG beams. Next, we analyze phase matching in HHG with LG beams and optimize the position of the atomic target with respect to the focus of the driving beam in order to achieve a high conversion efficiency.

In Ch. 5, we investigate HHG with driving beams with circular polarization. Thereby, we introduce bicircular beams. After a short discussion about their symmetry, we show that harmonics can be generated with these beams. In a next step, we analyze how the OAM of the driving beam is transferred to the generated harmonics and we derive selection rules that follow from the simultaneous conservation of energy, OAM and SAM. We furthermore show that we can precisely control the OAM of the generated harmonics. Afterwards, we examine the temporal evolution of the high-harmonic signal and analyze the shape of the so-called light springs.

Finally, we summarize our results in Ch. 6 and conclude with an outlook for possible future work.

Atomic units are used throughout the thesis unless stated otherwise:

$$e = \hbar = m_e = 4\pi\varepsilon_0 = 1.$$

2

TWISTED LIGHT BEAMS

2.1 PLANE WAVES

Generally, electromagnetic waves in vacuum can be described by a second-order linear partial differential equation, the homogeneous wave equation. In this thesis, we will focus on the electric field and ignore the magnetic field, since the electric field predominantly determines the driving field for HHG. We can write the wave equation for the electric field as [38]

$$\nabla^2\mathbf{E}(\mathbf{r},t) - \frac{1}{c^2}\frac{\partial^2}{\partial t^2}\mathbf{E}(\mathbf{r},t) = 0, \tag{2.1}$$

where c is the speed of light. For monochromatic fields, wen can separate the time dependent part from the spatial part as

$$\mathbf{E}(\mathbf{r},t) = \mathbf{u}(\mathbf{r})e^{-i\omega t}. \tag{2.2}$$

The spatial amplitude $\mathbf{u}(\mathbf{r})$ is then a solution to the Helmholtz equation

$$\left(\nabla^2 + k^2\right)\mathbf{u}(\mathbf{r}) = 0, \tag{2.3}$$

where $k = \frac{\omega}{c}$ denotes the wave number. If we consider waves that propagate in z-direction, we can write the wave vector as $\mathbf{k} = k\mathbf{e}_z$. A solution to the Helmholtz equation is given by

$$\mathbf{u}(\mathbf{r}) = \hat{\mathbf{e}}u_0e^{ikz}. \tag{2.4}$$

Here u_0 is the amplitude of the wave and $\hat{\mathbf{e}}$ is a polarization vector. For linear polarization along x-direction we have $\hat{\mathbf{e}} = \hat{\mathbf{e}}_x$, while for left ($\hat{\mathbf{e}}_+$) or right ($\hat{\mathbf{e}}_-$) circular polarization we have

$$\hat{\mathbf{e}}_\pm = \frac{1}{\sqrt{2}}\begin{pmatrix} 1 \\ \pm i \\ 0 \end{pmatrix}. \tag{2.5}$$

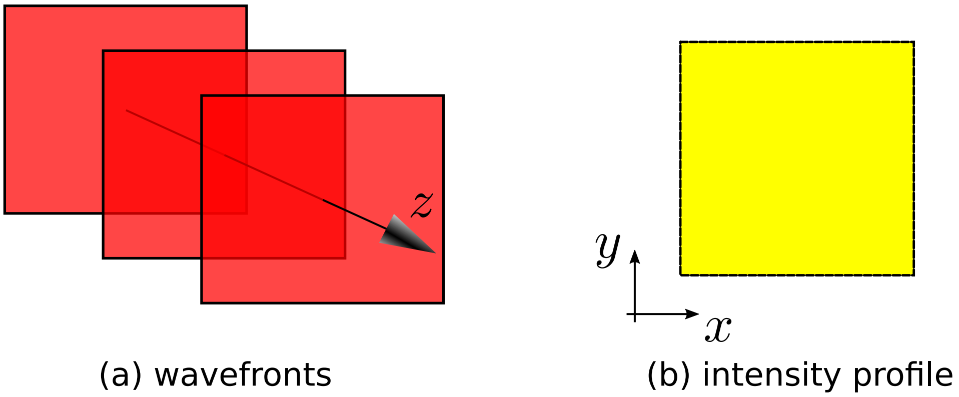

(a) wavefronts (b) intensity profile

Figure 2.1: (a) Phase fronts of a plane wave that propagates in z-direction. (b) Intensity profile of a plane wave perpendicular to the propagation direction shows a uniform distribution.

The wavefronts of these solutions are characterized by $e^{ikz} = \text{const}$, which describes planes perpendicular to the propagation direction, as shown in Fig. 2.2a. Therefore these solutions to the Helmholtz equation are also called *plane waves*. Another characteristic property of plane waves is a uniform intensity profile perpendicular to the propagation direction, also called transverse profile. This intensity profile is shown in Fig. 2.2b.

2.2 PARAXIAL APPROXIMATION

For plane waves the amplitude u_0 is independent of the spatial coordinate $\mathbf{r}$. However, this is only true for a very limited selection of beams. Generally the amplitude is position-dependent $u_0 = u_0(\mathbf{r})$, which makes is more difficult to find solutions to the Helmholtz equation. Nevertheless, if the z-derivative of the spatial amplitude $u(\mathbf{r})$ varies sufficiently slowly with z, such that

$$\left|\frac{\partial^2 u_0(\mathbf{r})}{\partial z^2}\right| << \left|k\frac{\partial u_0(\mathbf{r})}{\partial z}\right| \quad \text{and} \quad \left|\frac{\partial^2 u_0(\mathbf{r})}{\partial z^2}\right| << \left|\nabla_\perp^2 u_0(\mathbf{r})\right| \tag{2.6}$$

the Helmholtz equation (Eq. 2.3) can be rewritten in its paraxial approximation

$$\nabla_\perp^2 u_0(\mathbf{r}) + 2ik\frac{\partial u_0(\mathbf{r})}{\partial z} = 0. \tag{2.7}$$

We can rewrite this equation in cylindrical coordinates as

$$\left(\frac{1}{\rho}\frac{\partial}{\partial\rho}+\frac{\partial^2}{\partial\rho^2}+\frac{1}{\rho^2}\frac{\partial^2}{\partial\varphi^2}+2ik\frac{\partial}{\partial z}\right)u_0(\mathbf{r})=0. \tag{2.8}$$

2.2.1 *Gaussian beams*

Gaussian beams are a solutions to Eq. 2.8. Analytically, we can express the amplitude as

$$u_0(\rho,z)=u_0\frac{w_0}{w(z)}e^{\left(\frac{-\rho^2}{w(z)^2}\right)}e^{i\left(k\frac{\rho^2}{2R(z)}+\psi(z)\right)}. \tag{2.9}$$

The transverse profile of a Gaussian beam has a Gaussian shape, where the waist or more precisely the radius at which the amplitude of the beam reaches a fraction of $\frac{1}{e}$ of its on axis value at the focus $z=0$ is given by w_0. Along the beam axis the waist is given by

$$w(z)=w_0\sqrt{1+\left(\frac{z}{z_r}\right)^2}. \tag{2.10}$$

The Rayleigh range z_r is the distance from the focus, where the cross section of the beam has doubled

$$z_r=\frac{\pi\cdot w_0^2}{\lambda}. \tag{2.11}$$

The phase front radius $R(z)$ is given by

$$R(z)=z\left(1+\left(\frac{z_r}{z}\right)^2\right), \tag{2.12}$$

which is infinite at the focus, respectively the phase front is a plane at $z=0$. Generally, Gaussian beams do not have plane wave phase fronts, however the phase front radius is large compared to the waist. Thus for many applications it is reasonable to approximate Gaussian beams as plane waves. The beam has the smallest phase front radius at the Rayleigh range, where $R(z_r)=2z_r$. The Gouy phase

$$\psi(z)=-\arctan\left(\frac{z}{z_r}\right) \tag{2.13}$$

was discovered experimentally in 1890 by Louis Georges Gouy [39] and describes a phase shift of π across the focus of the beam.

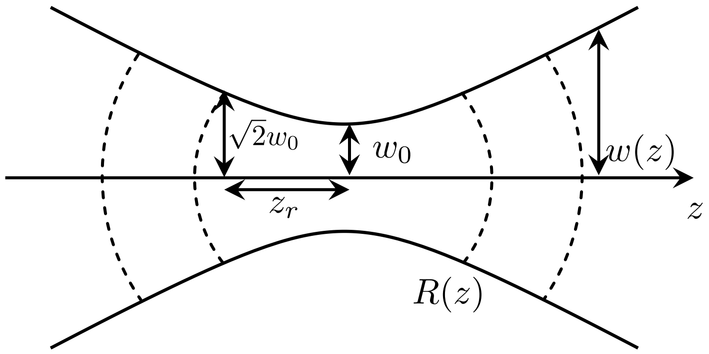

Figure 2.2: Visualization of geometrical parameters in a Gaussian beam that propagates in z-direction. Here, w_0 is the waist of the beam at the focus $z = 0$, $R(z)$ is the phase front radius and z_r is the Rayleigh range.

For many experiments in strong-field physics Ti:sapphire lasers with a wavelength of $\lambda = 800\,\text{nm}$ are used. Here, the waist is usually in the order of $30\,\mu\text{m}$ and the Rayleigh range is approximately $3.5\,\text{mm}$ [40].

2.2.2 *Laguerre-Gaussian beams*

A complete set of solutions to Eq. 2.8 are Laguerre-Gaussian (LG) beams, which can be expressed as

$$u_{\ell,p}(\rho,\varphi,z) = u_0 \frac{w_0}{w(z)} \left(\frac{\sqrt{2}\rho}{w(z)}\right)^{|\ell|} e^{\left(\frac{-\rho^2}{w(z)^2}\right)} L_p^{\ell}\left[\frac{2\rho^2}{w(z)^2}\right] \tag{2.14}$$

$$\times e^{i\left(\ell\varphi + \frac{k\rho^2}{2R(z)} + (2p+|\ell|+1)\psi(z)\right)}. \tag{2.15}$$

Here $L_p^{\ell}\left[\frac{2\rho^2}{w(z)^2}\right]$ are the generalized Laguerre polynomials [41]. The intensity profiles of LG beams show concentric rings, where the number of rings is determined by the radial quantum number p, more precisely by $p+1$. Several transverse intensity profiles of LG at $z = 0$ are shown in the upper row of Fig. 2.3. The azimuthal mode index ℓ is an eigenvalue of the amplitude with respect to the operator $\hat{L}_z = -i\frac{\partial}{\partial\varphi}$, and is related to the OAM of the beam. This parameter induced the azimuthal phase dependence, which can be seen in the lower row of Fig. 2.3. LG beams with OAM ℓ exhibit a phase shift of $\ell \cdot 2\pi$ along the azimuth. The radius of the first maximum in the transverse intensity profile increases with the OAM for a constant number of radial nodes, respectively a constant p.

Notably, a LG beam with $p = \ell = 0$ is a Gaussian beam, which also can be seen by

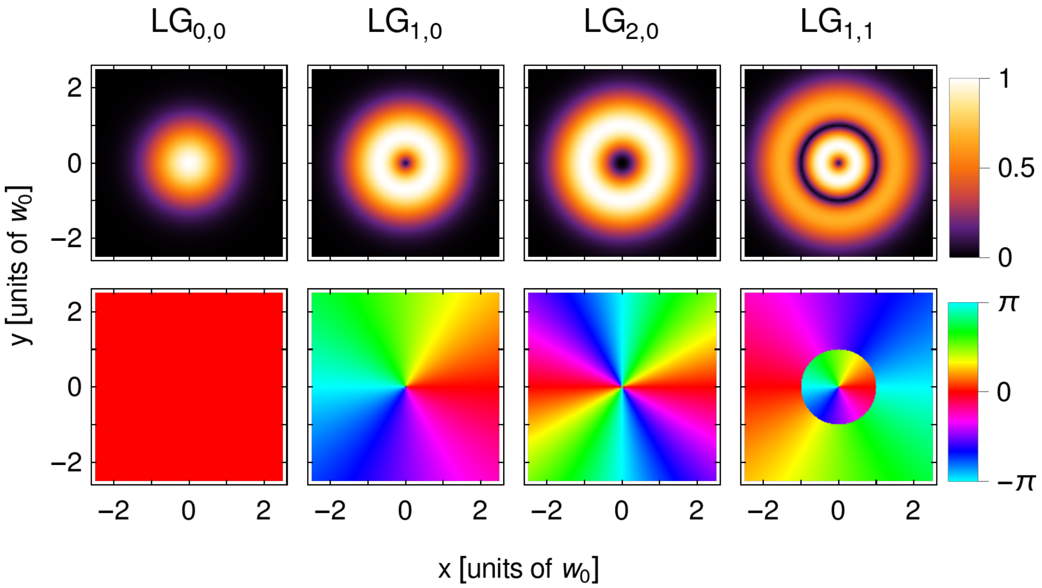

Figure 2.3: Transverse intensity profiles of various LG beams at $z = 0$ (upper row) and their corresponding phase profiles (lower row). The peak intensity was normalized to 1.

a comparison of Eq. 2.9 and Eq. 2.14. The phase profile of the $LG_{0,0}$ beam, respectively the Gaussian beam, shows the phase profile of a plane wave.

The azimuthal mode index also causes the corkscrew like structure for the planes of constant phase. Fig. 2.4 shows the planes of constant phase for a Gaussian beam ($LG_{0,0}$) and LG beams with nonzero OAM ℓ, which clearly show the helical phase fronts. Especially, for $\ell = 2$ there are two intertwined helicoids. Throughout the thesis we will use the notation $LG_{\ell,p}$ in order to describe a LG beam with OAM ℓ and radial node index p. The notation LG_ℓ implicitly assumes that $p = 0$.

2.2.3 *Divergence of Laguerre-Gaussian beams*

For Gaussian beams the waist of a beam is defined as the value, where the intensity decreases to $\frac{1}{e^2}$ of its on axis value. For large values of z the waist $w(z)$ is proportional to z. Therefore for Gaussian beams the divergence can be defined as the limit

$$\beta_{\text{div}} = \lim_{z\to\infty} \arctan\left(\frac{\partial w(z)}{\partial z}\right) = \arctan\left(\frac{\lambda}{\pi w_0}\right) \approx \frac{\lambda}{\pi w_0}, \tag{2.16}$$

where the last step is justified since $\lambda \ll w_0$. For some characteristic values of $\lambda = 800\,\text{nm}$ and $w_0 = 30\,\mu\text{m}$, we obtain a divergence of approximately 8 mrad.

However, this definition cannot be applied to LG beams, since their intensity on axis

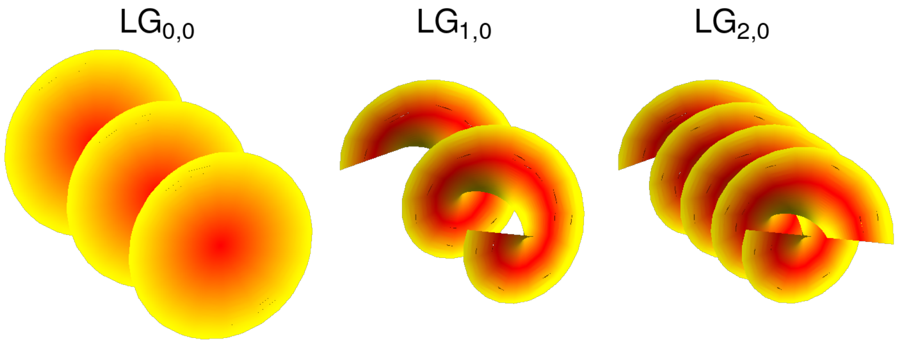

Figure 2.4: Planes of constant phase for a Gaussian beam (left) and LG beams with nonzero OAM.

is zero. Here, it is more appropriate to consider the radius of maximal intensity and its angular spread as the beam propagates. For monochromatic beams, we write

$$I(\rho, z) \sim \frac{1}{w(z)^2} \left(\frac{\sqrt{2}\rho}{w(z)} \right)^{2|\ell|} e^{-\frac{2\rho^2}{w(z)^2}}. \tag{2.17}$$

The radius of maximal intensity can be found by calculating $\frac{\partial I(\rho,z)}{\partial \rho} = 0$ and is given by

$$\rho_{\text{max}} = \sqrt{\frac{|\ell|}{2}} w(z). \tag{2.18}$$

With this definition, we get

$$\beta_{\text{div}} = \lim_{z \to \infty} \arctan \left(\frac{\partial \rho_{\text{max}}}{\partial z} \right) = \arctan \left(\sqrt{\frac{|\ell|}{2}} \frac{\lambda}{\pi w_0} \right) \approx \sqrt{\frac{|\ell|}{2}} \frac{\lambda}{\pi w_0}. \tag{2.19}$$

However, for Gaussian beams with $\ell = 0$ the radius of maximal intensity $\rho_{\text{max}} = 0$, which makes Eq. 2.18 not feasible for a general approach to describe the angular spread of LG beams.

Another approach to the divergence of LG beams is to consider the standard deviation of the spatial distribution, respectively the square root of the mean squared radius of the normalized transverse intensity profiles $\tilde{I}(\rho, z)$ [42]:

$$\begin{aligned} \rho_{\text{sd}} &= 2\pi \int_0^\infty \rho^2 \tilde{I}(\rho, z) \rho d\rho \qquad (2.20) \\ &= \sqrt{\frac{|\ell| + 1}{2}} w(z). \qquad (2.21) \end{aligned}$$

With this definition, we finally get

$$\beta_{\text{div}} = \lim_{z \to \infty} \arctan\left(\frac{\partial \rho_{\text{sd}}}{\partial z}\right) = \arctan\left(\sqrt{\frac{|\ell| + 1}{2}} \frac{\lambda}{\pi w_0}\right) \approx \sqrt{\frac{|\ell| + 1}{2}} \frac{\lambda}{\pi w_0} \tag{2.22}$$

for the divergence of LG beams. Notably, for large[1] values of ℓ that we usually face in HHG, the values for the divergence from Eq. 2.19 and Eq. 2.22 approach each other.

---

[1] $\ell \approx 10$

3

THEORETICAL APPROACH TO HIGH-HARMONIC GENERATION

In this chapter, we introduce theoretical models for HHG. In particular, we will consider the two opposing sides of HHG and their interplay. On the microscopic side, HHG arises from the interaction of a single atom with an intense laser field, whereas on the macroscopic side, the harmonic signal, which can be measured at the detector, is a coherent superposition of all single atom responses to the intense laser field. Therefore a theoretical investigation of HHG requires the analysis of both, the microscopic and the macroscopic side.

High-harmonics can be generated from atomic [5, 6], molecular [43], ionic [44] targets and even from solids [45] and crystals [46]. We focus on HHG with atomic gas targets. For brevity and simplicity, we will call our target *atom*.

3.1 MICROSCOPIC PICTURE

The microscopic picture of HHG describes the interaction of a single atom with the intense near-infrared laser field. Here, intense usually means in the order of $10^{14}\,\mathrm{W/cm^2}$. This picture helps to analyze for example which harmonics are generated and moreover provides information about the polarization of the harmonics.

In order to explore the microscopic picture we will first explain in Sec. 3.1.1 two different ionization mechanisms. Then, we introduce the vivid simple-man's or three step model in Sec. 3.1.2. In Sec. 3.1.3 we consider semi-classical aspects of HHG and continue in Sec. 3.1.4 with a quantum mechanical description in terms of the Lewenstein model in the framework of the SFA.

3.1.1 *Multiphoton and tunnel ionization*

Generally, if a laser, whose frequency is smaller than the binding energy of the valence electron, ionizes an atom, we face two different mechanisms of ionization. The distinction between these two mechanism finds its origin in the work of Keldysh

[47]. He introduced a dimensionless parameter to distinguish between the multiphoton and tunneling regime. The Keldysh parameter can be defined as

$$\gamma = \sqrt{\frac{I_p}{2U_p}}, \tag{3.1}$$

where I_p is the binding energy of the electron and U_p, the ponderomotive energy, is the cycle averaged kinetic energy of the electron in the laser field. For a linearly polarized laser with the electric field amplitude amplitude E_0 and frequency ω, we get

$$U_p = \frac{E_0^2}{4\omega^2}. \tag{3.2}$$

We generally distinguish between:

$\gamma \gg 1$: Multiphoton ionization, which assumes that the electron absorbs multiple photons to overcome the ionization threshold (Fig. 3.1a).

$\gamma \ll 1$: Tunnel ionization, which assumes that the strong electric field of the laser suppresses the atomic potential, such that a barrier is formed where the electron can tunnel through (Fig. 3.1b).

Of course, this sharp distinction is only true for limiting cases. This can be further illustrated by the dependencies of the Keldysh parameter to the frequency and the amplitude of the electric field:

$$\gamma \sim \frac{\omega}{E_0}. \tag{3.3}$$

Intuitively, tunneling is favored if the field becomes more static, which implies that the electron has more time to tunnel through the barrier. Similarly we can argue that the electron is more likely to tunnel if the barrier is stronger suppressed. Thus we can summarize that the probability for the electron to be released via tunnel ionization can be increased by decreasing the frequency and increasing the field amplitude.

3.1.2 *Simple-man's model*

An intuitive explanation and by far most vivid and powerful picture of various processes in strong fields, such as HHG, was provided by Corkum [8]. He divided these processes in three separate steps, as illustrated in Fig. 3.2. Generally we can consider these three steps as follows:

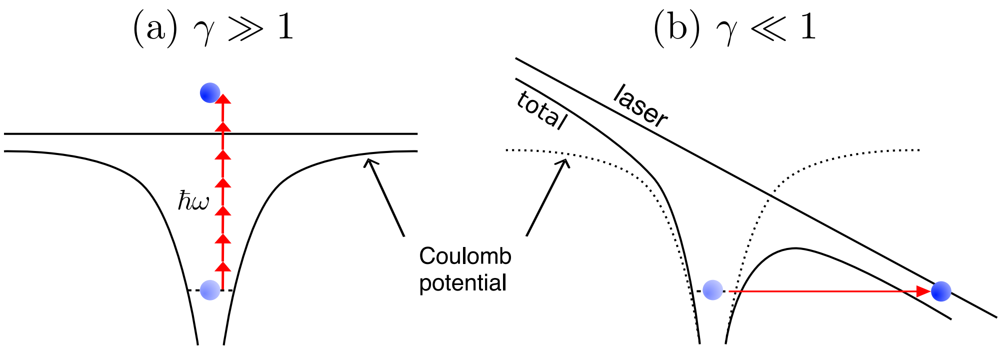

Figure 3.1: Illustration of (a) multiphoton and (b) tunnel ionization. In the multiphoton regime the electron (blue) is released due to the absorption of several photons. In the tunneling regime, the strong laser field suppresses the atomic potential, which enables the electron to tunnel.

1. The strong laser field suppresses the atomic potential, which forms a barrier. An electron can tunnel through this barrier and thus be released via tunnel ionization.
2. The released electron is driven and accelerated by the strong oscillating laser field. After half[1] a cycle, the electric field changes its sign and therefore causes an acceleration of the electron in the opposite direction.
3. The electron may come back to its parent ion. As the electron comes back, it may:
   - scatter elastically from the ion (rescattering), which gives rise to photo electrons with very high momentum, up to $10U_p$ [48, 49],
   - scatter inelastically and release a second electron (non-sequential double ionization) [50, 51]
   - recombine under the emission of a high energetic photon, which is known as HHG [52, 53].

In the context of this thesis we will focus in particular on the latter, respectively HHG.

3.1.3 *Semi-classical aspects of HHG*

The ionization of the atom, respectively the release of the electron is typically described as a tunnel ionization through the suppressed barrier of the atomic potential. There are several models that approximate the probability for an electron to

---

[1] This is in particular true for linearly polarized laser fields. For fields of different polarization, this timing might be different.

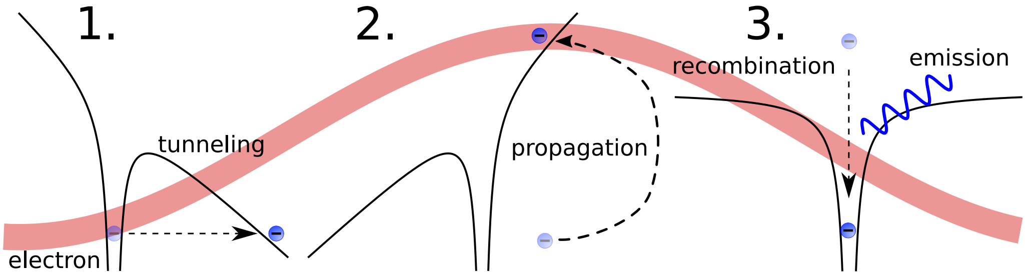

Figure 3.2: Sketch of the three step model for HHG: First, an electron is released from the atom by the strong laser field via tunnel ionization. Subsequently the released electron is accelerated and driven by the strong external laser field. Finally the electron may come back to the parent ion and recombine under the emission of a high energetic photon.

tunnel through the potential barrier at a given time t' [54, 55]. One of the most popular works was published by Ammosov, Delone and Krainov, where they introduced the so-called ADK-rate [56]. Generally the probability for tunneling increases with the instantaneous field strength of the electric field, which means that the stronger the barrier is suppressed the more likely is an electron to tunnel through the potential barrier.

After the the electron tunneled through the potential barrier it can be modeled as a classical particle that enters the continuum at the tunnel exit $r_0 \approx \frac{I_p}{E_0}$ with negligible small velocity. For these classical consideration we will set the velocity to zero. Here I_p is the ionization potential and E_0 the amplitude of the electric field. The tunnel exit is a few (≈ 10) atomic units away from the position of the ion and will be neglected for these classical considerations. By means of classical physics, it is possible precisely analyze the motion of electrons in terms of well-defined trajectories. We write the initial conditions of the electron's trajectory as

$$\mathbf{r}(t = t') = 0 \tag{3.4}$$

and

$$\dot{\mathbf{r}}(t = t') = 0. \tag{3.5}$$

Once the electron is released, its motion is governed by the electric field of the laser. During the acceleration we ignore further interaction with the ion and neglect the influence the Coulomb potential to the trajectory of the electron. In this chapter, we

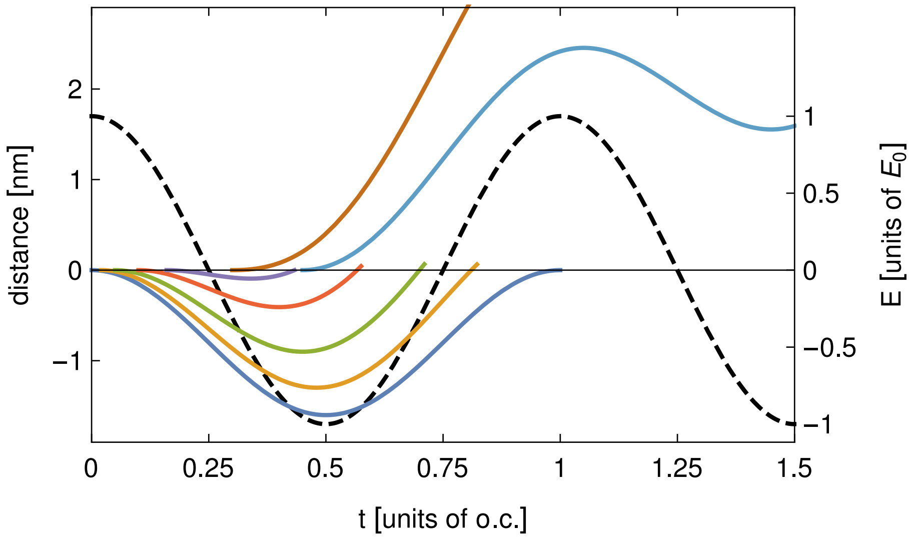

Figure 3.3: Sample of classical electron trajectories in a linearly polarized laser field with wavelength $\lambda = 800\,\mathrm{nm}$ (solid colored lines). The dashed black line indicates the electric field. The electrons start at the position of the parent ion (on the x-axis). The distance that an electron travels away from the parent ion clearly depends on the time when the electron starts. Notably, only electrons that start between 0 and 0.25 optical cycles (o.c.) come back to the parent ion. Electrons that start between 0.25 and 0.5 o.c. are driven away. The trajectories from electrons released between 0.5 and 0.75 (0.75 and 1.0) o.c. are similar to those between 0 and 0.25 (0.25 and 0.5) o.c., just with an opposed sign of the propagation direction, due to the symmetry of the laser field.

will address the example of a linearly polarized laser field $\mathbf{E}(t) = E_0 \cos(\omega t)\mathbf{e}_x$ and write the equations of motion for the free electron as

$$m_e \ddot{\mathbf{r}} = q\mathbf{E}(t), \tag{3.6}$$

where m_e is the mass and $q = -e$ is the charge of the electron. Since the electron is only accelerated in the direction of the electric field, we just consider the x-component of the electronic trajectory. Integration of the equations of motion with the initial conditions (Eq. 3.4) and (Eq. 3.5) yields:

$$\dot{x}(t) = \frac{eE_0}{m_e\omega}\left(\sin(\omega t') - \sin(\omega t)\right) \tag{3.7}$$

$$x(t) = \frac{eE_0}{m_e\omega}(t - t')\sin(\omega t') + \frac{eE_0}{m_e\omega^2}\left(\cos(\omega t) - \cos(\omega t')\right). \tag{3.8}$$

The condition for the electron to return to its parent ion at some later time t is $x(t) = 0$. Fig. 3.3 shows that only not all of the released electrons will come back to its parent ion to recombine. More specifically, only electrons released in the first quarter cycle of the electric field will return to the parent ion. The return condition

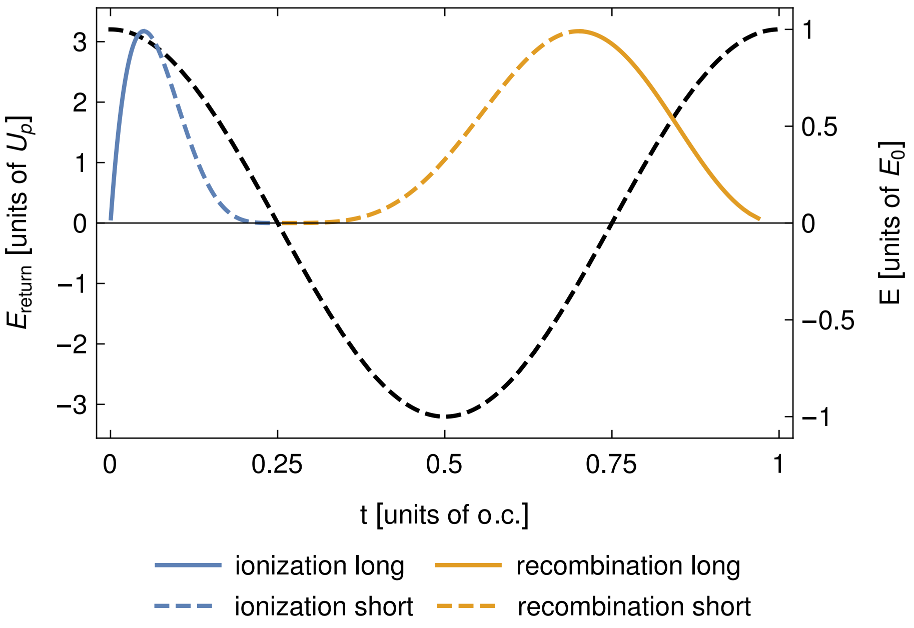

Figure 3.4: Kinetic energies of the classical electron as it returns to the parent ion depending on the ionization time (blue) and return time (yellow). Notably, there are two different ionization times with their corresponding recombination times that lead to the same kinetic energy when the electron returns. These two trajectories are distinguished by their travel times and called short (dashed) and long (solid) trajectories. The maximal return energy is 3.17 U_p.

immediately makes clear why the shape of the electric field has big impact on HHG. In circularly polarized fields, for example, none of the electronic trajectories will come back to the ion, which explains why HHG does not take place in these fields.

As the electron recombines a photon is emitted. The energy of the emitted photon can be calculated by the sum of the return energy of the electron and the ionization potential. The return energy E_{return} is given by:

$$E_{\text{return}} = \frac{1}{2} m_e \dot{x}(t)^2 \tag{3.9}$$

under the condition that $x(t) = 0$. Numerically, we find that the highest possible return energy for the electron is

$$E_{\text{return,max}} = 3.17 \frac{e^2 E_0^2}{2 m_e \omega^2} = 3.17 U_p. \tag{3.10}$$

In Fig. 3.4, we show that there are two possible ionization times (blue) in each half cycle for each return energy below $3.17 U_p$ with their corresponding return times (yellow). These two ionization times give rise to two different trajectories that can be characterized as short (dashed) and long (solid) trajectories with respect to their travel times. Within this model, the highest harmonic order q that can be generated in linearly polarized laser field is

$$q\omega = 3.17U_p + I_p, \tag{3.11}$$

which is also known as the cutoff in HHG. Within this classical model it is not possible to generate harmonics beyond this cutoff. The simple classical model enables good insight into the physics of HHG and is helps to understand some fundamentals, such as the high-harmonic cutoff. However, in order to study the process of HHG in more detail, it is essential to apply quantum mechanical models.

3.1.4 *Lewenstein model*

There are multiple ways to quantum mechanically compute HHG as a single atom response. The most direct approach is the exact numerical solution of the time dependent Schrödinger equation [57–59]. However, the this can be tedious, computationally demanding, especially if macroscopic effects are considered, c.f. Sec. 3.2. The analysis of macroscopic effects, such as phase matching, requires that the high-harmonic signal is computed for multiple[2] times. These calculations require shorter computation times and make the single active electron approximation and application of the SFA almost inevitable.
The *Lewenstein model* has been developed in 1994 [9]. It is an SFA based analytical and quantum mechanical approach for HHG, which still provides an intuitive physical picture in terms of the three step model [8]. This model is the underlying theoretical approach for this thesis.

3.1.4.1 *Single active electron approximation*

The time dependent Schrödinger equation for a single active electron can be written as

$$i\frac{\partial}{\partial t}\left|\Psi(\mathbf{r},t)\right\rangle = H_0\left|\Psi(\mathbf{r},t)\right\rangle, \tag{3.12}$$

where $H_0 = -\frac{1}{2}\nabla^2 + V(\mathbf{r})$ is the Hamiltonian that determines the electronic ground state

$$H_0\left|0\right\rangle = -I_p\left|0\right\rangle. \tag{3.13}$$

---

[2] $\approx 10^4$ and even more often

For the example of the hydrogen atom the potential is given by $V(\mathbf{r}) = -\frac{1}{r}$ and $I_p = \frac{1}{2}$ a.u. $\approx 13.6\,\text{eV}$. The spatial distribution of the ground state is given by

$$|0\rangle_{1s} = \frac{1}{\sqrt{\pi}} e^{-r}. \tag{3.14}$$

The wave function of the ground state can be expressed as

$$|\Psi(\mathbf{r}, t)\rangle = |0\rangle_{1s}\, e^{-iI_p t}. \tag{3.15}$$

More generally, we can write the spatial distribution of the ground state wave function for hydrogen like *s*-waves as

$$|0\rangle = \frac{\alpha^{\frac{3}{4}}}{\sqrt{\pi}} e^{-\sqrt{\alpha} r}, \tag{3.16}$$

where $\alpha = 2I_p$. If we now consider an atom under the influence of an electric field $\mathbf{E}(t)$ in length gauge, the time dependent Schrödinger equation can be expressed in dipole approximation as

$$i\frac{\partial}{\partial t}|\Psi(\mathbf{r}, t)\rangle = \left(-\frac{1}{2}\nabla^2 + V(\mathbf{r}) - \mathbf{r}\cdot\mathbf{E}(t)\right)|\Psi(\mathbf{r}, t)\rangle\,. \tag{3.17}$$

Here the application of the dipole approximation is justified since the extent of the electron wave packet, which is in the order of $a_0 = 5.2 \cdot 10^{-2}\,\text{nm}$, is small compared to 800 nm, a typical wavelength of the electric field used for HHG.

3.1.4.2 *Strong-field approximation*

One of the key assumptions in the SFA is that the electron undergoes a direct transition from the ground state to the continuum states without hitting any intermediate resonances, which is justified for small Keldysh parameters. Therefore, we only consider the atomic ground state and the continuum states in the derivation. As pointed out in Sec. 3.1.3, at intensities of $10^{14}\,\text{W/cm}^2$ a released electron may be driven $2\,\text{nm} \approx 40\,\text{a.u.}$ away from the parent ion before it comes back to recombine. Here, the laser field clearly dominates the dynamic of the electron, since the Coulomb force

$$F_c \approx \frac{1}{40^2}\,\text{a.u.} \approx 0.0006\,\text{a.u.} \tag{3.18}$$

is negligible compared to the electric force

$$F_{el} = E_0 \approx 0.05\,\text{a.u.} \tag{3.19}$$

felt by the electron due to the strong laser field laser. The continuum wave function for an electron with asymptotic kinetic momentum $\mathbf{v}$ are eigenstates to H_0 as

$$H_0 \left|\mathbf{v}\right\rangle = \frac{v^2}{2} \left|\mathbf{v}\right\rangle \tag{3.20}$$

with $\left|\mathbf{v}\right\rangle = e^{-i\mathbf{v}\cdot\mathbf{r}}$. If we only consider the atomic ground and the continuum states, we can write an ansatz for the solution of the time dependent Schrödinger equation (Eq. 3.17) as

$$\left|\Psi(\mathbf{r},t)\right\rangle = e^{-iI_p t}\left(a(t)\left|0\right\rangle + \int d^3\mathbf{v} b(\mathbf{v},t)\left|\mathbf{v}\right\rangle\right), \tag{3.21}$$

where $a(t)$ is the amplitude of the ground state and $b(\mathbf{v},t)$ are the amplitudes of the corresponding continuum states.

3.1.4.3 *Time dependent dipole moment*

Within the Lewenstein model it is assumed that the radiation is emitted in terms of electric dipole radiation. If we calculate the expectation value of the electric dipole from the wave function Eq. 3.21, we obtain:

$$\begin{aligned}\mathbf{D}(t) &= \left\langle\Psi(\mathbf{r},t)\right|\mathbf{r}\left|\Psi(\mathbf{r},t)\right\rangle \\ &= a^2(t)\left\langle 0\right|\mathbf{r}\left|0\right\rangle + \int d^3\mathbf{v} a^\dagger(t) b(\mathbf{v},t)\left\langle 0\right|\mathbf{r}\left|\mathbf{v}\right\rangle \\ &\quad + \int d^3\mathbf{v} a(t) b(\mathbf{v},t)^\dagger\left\langle \mathbf{v}\right|\mathbf{r}\left|0\right\rangle \\ &\quad + \int d^3\mathbf{v}\int d^3\mathbf{v}' b^\dagger(\mathbf{v}',t) b(\mathbf{v},t)\left\langle \mathbf{v}'\right|\mathbf{r}\left|\mathbf{v}\right\rangle .\end{aligned} \tag{3.22}$$

The first term vanishes, since $\left\langle 0\right|\mathbf{r}\left|0\right\rangle = 0$. Additionally, we neglect the continuum-continuum transitions in the SFA, which are represented by the last term. Now, we can rewrite the time dependent dipole moment as

$$\mathbf{D}(t) = \int d^3\mathbf{v} a^\dagger(t) b(\mathbf{v},t)\mathbf{d}^*(\mathbf{v}) + \text{c.c.}, \tag{3.23}$$

where c.c. denotes the complex conjugate and $\mathbf{d}^*(\mathbf{v})$ is the hermitian conjugate of $\mathbf{d}(\mathbf{v})$. Here,

$$\mathbf{d}(\mathbf{v}) = \langle \mathbf{v} | \mathbf{r} | 0 \rangle \tag{3.24}$$

are the dipole transition matrix elements, which can be calculated analytically for initial hydrogenic wave functions. For example, for a hydrogenic s-wave, we get

$$\mathbf{d}(\mathbf{v}) = \langle \mathbf{v} | \mathbf{r} | 0 \rangle = -i2^{\frac{7}{2}} \alpha^{\frac{5}{4}} \frac{\mathbf{v}}{\pi \left(v^2 + \alpha\right)^3}. \tag{3.25}$$

In order to compute the time dependent dipole moment, we are now only left to find an expression for $b(\mathbf{v}, t)$.

3.1.4.4 *Analytical solution of the time dependent Schrödinger equation*

In order to compute the continuum state amplitudes $b(\mathbf{v}, t)$, we insert the wave function (Eq. 3.21) into the time dependent Schrödinger equation (Eq. 3.17) and solve it for $b(\mathbf{v}, t)$. We thereby obtain [9, 40]

$$\begin{aligned} b(\mathbf{v}, t) = -i \int_{-\infty}^{t} & dt' a(t') \mathbf{E}(t') \cdot \mathbf{d}[\mathbf{v} - \mathbf{A}(t) + \mathbf{A}(t')] \\ & \times e^{\int_{t'}^{t} dt'' \left(\frac{1}{2}(\mathbf{v} - \mathbf{A}(t) + \mathbf{A}(t''))^2 + I_p\right)}. \end{aligned} \tag{3.26}$$

Here, $\mathbf{A}(t)$ is the vector potential, which is connected to the electric field by

$$\mathbf{E}(t) = -\frac{\partial}{\partial t} \mathbf{A}(t). \tag{3.27}$$

For few cycle pulses or laser intensities below the saturation intensity, we may neglect the depletion of the ground state and thus to approximate $a(t) \simeq 1$.

3.1.4.5 *Conservation of canonical momentum*

The canonical momentum of an electron in the laser field is a conserved quantity and in atomic units defined as

$$\mathbf{p} = \mathbf{v}(t) - \mathbf{A}(t). \tag{3.28}$$

The canonical momentum can be used to further simplify the continuum state amplitude $b(\boldsymbol{\nu}, t)$ to

$$b(\boldsymbol{\nu}, t) = i \int_{-\infty}^{t} dt' \mathbf{E}(t') \cdot \mathbf{d}[\mathbf{p} + \mathbf{A}(t')] \, e^{-\int_{t'}^{t} dt'' \left(\frac{1}{2}(\mathbf{p}+\mathbf{A}(t''))^2 + I_p\right)} \tag{3.29}$$

Finally, we insert the continuum state amplitude from Eq. 3.29 into the time dependent dipole moment Eq. 3.23

$$\begin{aligned} \mathbf{D}(t) = & i \int_{-\infty}^{t} dt' \int d^3\mathbf{p} \, \mathbf{d}^*(\mathbf{p} + \mathbf{A}(t))\mathbf{E}(t') \\ & \cdot \mathbf{d}(\mathbf{p} + \mathbf{A}(t')) \times e^{-iS(\mathbf{p},t,t')} + \text{c.c.}, \end{aligned} \tag{3.30}$$

where

$$S(\mathbf{p}, t, t') = \int_{t'}^{t} dt'' \left(\frac{1}{2}(\mathbf{p} + \mathbf{A}(t'')) + I_p \right). \tag{3.31}$$

This expression of the time dependent dipole moment has a vivid physical interpretation in terms of the three step model, which we presented in Fig. 3.2. The term $\mathbf{E}(t') \cdot \mathbf{d}(\mathbf{p} + \mathbf{A}(t'))e^{iI_p t'}$ describes the transition of the electron from a ground state to the continuum at time t' due to its interaction with the external electric field $\mathbf{E}(t')$ (Step 1). The exponential term $e^{-i\int_{t'}^{t} dt'' \left(\frac{1}{2}\mathbf{p}+\mathbf{A}(t'')\right)^2}$, is phase that the electron waves accumulates from the ionization time t' to the recombination time t and equal to the classical action of a free electron that propagates during that time in the laser field (Step 2). This phase is also often called dipole phase. Eventually, the term $\mathbf{d}^*(\mathbf{p} + \mathbf{A}(t))e^{-iI_p t}$ describes the recombination of the electron from the continuum to its ground state (Step 3).

3.1.4.6 *Saddle-point approximation*

The numerical integration over the momenta $d^3\mathbf{p}$ in the time dependent dipole moment (Eq. 3.30) is computationally expensive, especially if more realistic, extended atomic gas targets are considered, where the dipole moment has to be computed 10^4 times or even more often. In order to overcome this computational issue, the so called saddle-point or stationary phase approximation can be applied. Generally the stationary phase methods approximates integrals in the form [60]

$$\int d^3\mathbf{x} g(\mathbf{x}) e^{if(\mathbf{x})} \approx \sum_{\mathbf{x}_s} \sqrt{\frac{(2\pi i)^3}{\det(f''(\mathbf{x}_s))}} g(\mathbf{x}_s) e^{if(\mathbf{x}_s)}, \tag{3.32}$$

provided that $g(\mathbf{x})$ changes much slower with $\mathbf{x}$ than $e^{if(\mathbf{x})}$. The $\mathbf{x}_s$ are the stationary points of f with respect to $\mathbf{x}$ such that

$$\nabla_{\mathbf{x}} f(\mathbf{x}) \overset{!}{=} 0 \tag{3.33}$$

and

$$f''(\mathbf{x}_s) = \left(\frac{\partial^2 f}{\partial x_i \partial x_j}(\mathbf{x}) \bigg|_{\mathbf{x}=\mathbf{x}_s} \right)_{i,j=1,2,3} . \tag{3.34}$$

is the Hessian matrix of the function f evaluated at the saddle points $\mathbf{x}_s$.
Let us now apply this saddle-point approximation to the time dependent dipole moment (Eq. 3.30). Here, the saddle-point over the intermediate momenta $\mathbf{p}$ can be calculated by

$$\nabla_{\mathbf{p}} S(\mathbf{p}, t, t') \overset{!}{=} 0. \tag{3.35}$$

Luckily, there is always a unique solution for the momentum saddle-point, since the classical action of the electron in Eq. 3.31 is quadratic in $\mathbf{p}$. The momentum saddle-point is given by

$$\mathbf{p}_{st} = -\frac{1}{t-t'} \int_{t'}^{t} d\tau \, \mathbf{A}(\tau). \tag{3.36}$$

Physically, the saddle-point approximation selects exactly the canonical momentum $\mathbf{p}$ for an electron, such that it recombines at time t if it was released earlier at time t'. With this approximation, we can reduce the four dimensional integral in the time dependent dipole moment (Eq. 3.30) to a one dimensional integral:

$$\begin{aligned} \mathbf{D}(t) =& i \int_{-\infty}^{t} dt' \left(\frac{2\pi i}{(t-t'-i\epsilon)} \right) \mathbf{d}^*(\mathbf{p}_s + \mathbf{A}(t)) \, \mathbf{E}(t') \\ & \cdot \mathbf{d}(\mathbf{p}_s + \mathbf{A}(t')) \times e^{-iS(\mathbf{p}_s, t, t')} + \text{c.c.}. \end{aligned} \tag{3.37}$$

Finally the frequency spectrum of the emitted harmonics can be obtained by the Fourier transform of the time dependent dipole moment (Eq. 3.37)

$$\begin{aligned} D(q\omega) =& i \int_{-\infty}^{\infty} dt \int_{-\infty}^{t} dt' \left(\frac{2\pi i}{(t-t'-i\epsilon)} \right) \mathbf{d}^*(\mathbf{p}_s + \mathbf{A}(t)) \, \mathbf{E}(t') \\ & \cdot \mathbf{d}(\mathbf{p}_s + \mathbf{A}(t')) e^{iq\omega t - iS(\mathbf{p}_s, t, t')} + \text{c.c.}, \end{aligned} \tag{3.38}$$

where q is the harmonic order. The intensity of the generated harmonics are given by

$$I(q\omega) \propto (q\omega)^4 |D(q\omega)|^2. \tag{3.39}$$

3.1.5 *Quantum orbit approach*

The basic idea behind the quantum orbit approach is to further apply the saddle-point approximation to both time integrals in Eq. 3.38. The saddle-point with respect to t' is given by

$$\begin{aligned} &\frac{\partial}{\partial t'}(q\omega t - S(\mathbf{p}_s, t, t')) = 0 \\ &\qquad \Rightarrow \frac{1}{2}\left(\mathbf{p}_s + \mathbf{A}(t')\right)^2 = -I_p, \end{aligned} \tag{3.40}$$

which physically expresses conservation of energy when the electron is released from the atom, while the saddle-point with respect to t,

$$\begin{aligned} &\frac{\partial}{\partial t}(q\omega t - S(\mathbf{p}_s, t, t')) = 0 \\ &\qquad \Rightarrow \frac{1}{2}\left(\mathbf{p}_s + \mathbf{A}(t)\right)^2 = q\omega - I_p, \end{aligned} \tag{3.41}$$

describes conservation of energy, when the electron recombines with its parent ion. We now can approximate the harmonic dipole as a summation over the saddle-points $s = (\mathbf{p}_s, t'_s, t_s)$:

$$\begin{aligned} \mathbf{D}(q\omega) = i \sum_s & \frac{2\pi}{\sqrt{\det(S'')}} \left(\frac{2\pi}{t_s - t'_s}\right)^{\frac{3}{2}} \mathbf{d}^*(\mathbf{p}_s + \mathbf{A}(t_s))\, \mathbf{E}(t'_s) \\ & \cdot \mathbf{d}(\mathbf{p}_s + \mathbf{A}(t'_s)) e^{[-iS(\mathbf{p}_s, t_s, t'_s) + iq\omega t_s]}, \end{aligned}$$

where S'' is the Hessian matrix of the action $S(\mathbf{p}, t, t')$, which is given by

$$S''(\mathbf{p}_s, t_s, t'_s) = \left.\begin{pmatrix} \frac{\partial^2 S(\mathbf{p}_s,t,t')}{\partial t^2} & \frac{\partial^2 S(\mathbf{p}_s,t,t')}{\partial t \partial t'} \\ \frac{\partial^2 S(\mathbf{p}_s,t,t')}{\partial t' \partial t} & \frac{\partial^2 S(\mathbf{p}_s,t,t')}{\partial t'^2} \end{pmatrix}\right|_{t=t_s t'=t'_s}. \tag{3.42}$$

To get a more vivid picture, we can interpret t' as *time of ionization* and t as *time of recombination*. Notably, these times have to be complex since $I_p > 0$. Otherwise Eq. 3.40 would not have any solution.

Each solution $s = (\mathbf{p}_s, t'_s, t_s)$ to the saddle-point equations (Eq. 3.36, 3.40 and 3.41)

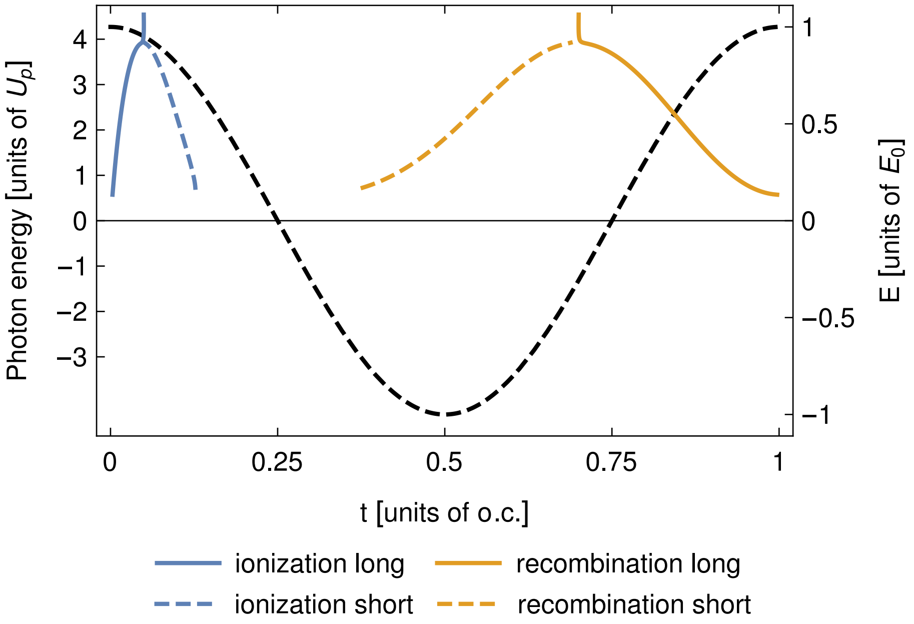

Figure 3.5: The energy of the emitted photons calculated with the quantum orbit formalism. Similarly to the classical approach in Fig. 3.4, there are short and long trajectories.

defines a unique complex trajectory, a so called *quantum orbit* [61–63]. Thus it can be said that the quantum orbit approach approximates and simplifies the integrals to compute the HHG spectra as a summation over several complex electron trajectories.

3.1.5.1 *Quantum orbits in a linearly polarized field*

Let us discuss the quantum orbits in the context of a linearly polarized laser field. Here, we express the electric field as:

$$\mathbf{E}(t) = E_0 \cos(\omega t)\mathbf{e}_x \tag{3.43}$$

and therefore the vector potential is given by

$$\mathbf{A}(t) = -\frac{E_0}{\omega}\sin(\omega t)\mathbf{e}_x. \tag{3.44}$$

If we insert the vector potential into the saddle point equations (Eq. 3.36, 3.40 and 3.41), we can calculate the complex ionization and recombination times of the quantum orbits that will contribute to a given harmonic order q. We present the results in Fig. 3.5. Obviously these results are similar to those presented in Fig. 3.4, where we considered classical trajectories. As pointed out before, the solution to the saddle-point equations for the ionization and recombination times are actually complex. Therefore, it is important to mention that we just show the real part of the ionization and recombination times, respectively. Similarly to the classical analysis, we find for each harmonic order and in each half cycle two different ionization times with their corresponding recombination times. Here, we also restrict ourselves to quantum orbits with travel times shorter or equal to one cycle. Thereby the travel time τ is defined as $\tau = \mathrm{Re}(t - t')$.

For the classical trajectories, we found a maximal return energy of the electron of $3.17U_p$ and thus a maximal photon energy of the generated harmonics of $3.17U_p + I_p$. However the quantum orbits theory predicts a slightly higher cutoff for the photon energy of approximately $3.17U_p + 1.32I_p$, which was shown by Lewenstein [9]. In addition, we can also predict harmonic orders beyond this cutoff with the quantum orbits theory. However, there is only one quantum orbit that contributes to these harmonics. These harmonics cannot be explained with the classical model.

3.2 MACROSCOPIC PICTURE

So far we considered HHG with only a single atom. However, in an experiment a gas jet or a gas cell with many ($\approx 10^{12}$) atoms are placed in the interaction region of the beam to contribute to HHG. Here, we define interaction region as the volume in the beam with sufficiently high intensity, such that harmonics can be generated. Since HHG is a coherent process the measured radiation at the detector is a superposition of all single atom contributions from the interaction region.

Especially for beams with spatially structured intensity profiles, such as LG beams, it is important to include this macroscopic picture of HHG. Harmonics generated at different positions in the beam are usually exposed to different local intensities and therefore are emitted with different phase. This affects, for instance, the conversion efficiency, which impacts the intensity at which a given harmonic can be measured at the detector. Furthermore, the OAM induced azimuthal phase shift, which was introduced in Ch. 2 also causes that harmonics generated at different azimuthal angles are emitted at different phases. In order to analyze the OAM of the generated harmonics the coherent superposition of all the single atom contributions is required as well.

Thereby, we consider two approaches to take macroscopic atomic targets in HHG into account [64]:

1. Within the Fraunhofer diffraction model, we approximate the atomic gas target as a layer of atoms perpendicular to the propagation axis.

2. The numerical propagation of individual radiators to a virtual detector can be used to simulate more realistic three dimensional gas targets, such as gas jets from a nozzle or atomic clouds in a cell.

Generally the phase and intensity profiles calculated with the Fraunhofer diffraction model agree very well with those of the exact numerical propagation [65, 66]. A major advantage of the numerical propagation is that it provides access to the generated electric field at the detector and automatically takes longitudinal phase matching into account.

3.2.1 *Fraunhofer diffraction*

The Fraunhofer diffraction formula [67] can be applied to calculate the phase and intensity profiles of different harmonic orders in the far-field, respectively at the virtual detector. In order to make use of this formula, we model the atomic gas target as a thin layer of atoms that can be displaced with respect to the focus plane of the beam. A sketch of the geometry is shown in Fig. 3.6, where we indicate the atoms by the small black dots in the near-field.
In order to make use of this formula, we calculate the harmonic response from each atom to its local field by means of Eq. 3.38, which gives us the complex amplitude of each harmonic order in the near-field $A_q^{(\text{near})}$ at position (ρ', φ', z'), respectively in the interaction region. The complex amplitude of the q^{th} harmonic in the far-field can then be written as

$$A_q^{(\text{far})}(\beta, \varphi) = \int_0^\infty \int_0^{2\pi} \rho' d\rho' d\varphi' A_q^{(\text{near})}(\rho', \varphi', z') \times e^{\left(-i\frac{2\pi}{\lambda_q}\rho' \tan(\beta)\cos(\varphi-\varphi')\right)} \tag{3.45}$$

where $\lambda_q = \lambda/q$ is the wavelength of the q^{th} harmonic. The angle φ is the polar angle in the far-field and β is the angle of divergence, cf. Fig. 3.6.

3.2.2 *Numerical propagation of the emitted radiation*

Another approach has been developed by Hernández-García [68, 69]. This approach propagates the radiation emitted from every radiator in the target to a virtual detector an thus allows for a simulation of three dimensional gas target. Within this approach, we decompose the target into a discrete set of single atom contributions

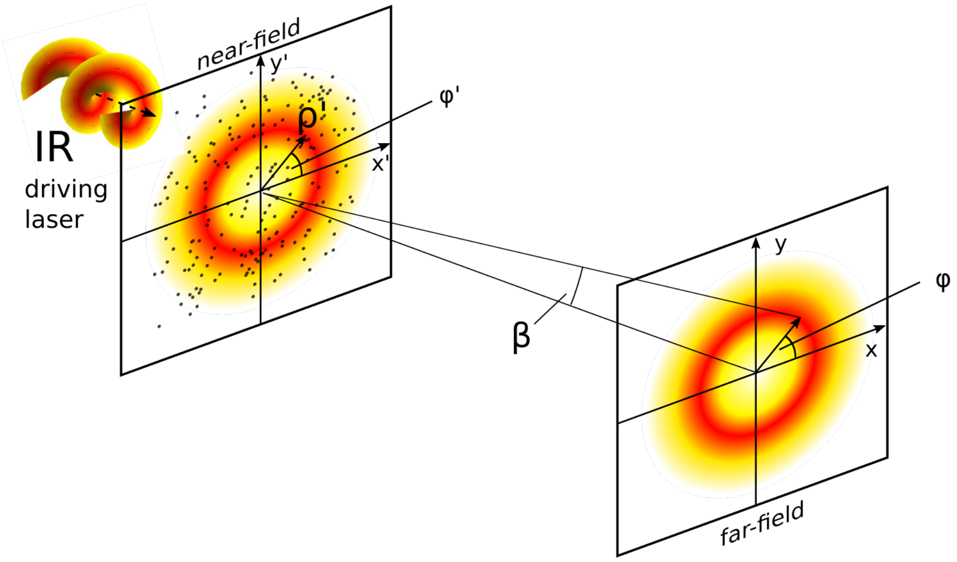

Figure 3.6: Geometry of the Fraunhofer diffraction formula: The incident near-infrared driving laser interacts with the gas target in the near-field. The gas target is approximated by a thin layer at the focus of the beam extended over the whole beam, which is indicated by the black dots. At each point in the gas target harmonics are emitted. The emitted harmonics contribute to the far-field. The divergence of the harmonics can be described by the angle β.

(radiators). The electric field at the detector that has been generated by a single atom at position $\mathbf{r}_j$ can be calculated by

$$\mathbf{E}_j\left(\mathbf{r}_d, t\right) = \frac{1}{c^2}\frac{q_j}{\left|\mathbf{r}_d - \mathbf{r}_j(0)\right|}\,\mathbf{s}_d \times \left[\mathbf{s}_d \times \mathbf{a}_j\left(t - \frac{\left|\mathbf{r}_d - \mathbf{r}_j(0)\right|}{c}\right)\right], \tag{3.46}$$

where $\mathbf{a}_j$ is the dipole acceleration of the radiator placed at $\mathbf{r}_j$, respectively the second derivative of Eq. 3.30 with respect to time. The vector $\mathbf{r}_d$ is the vector that points to the detector and $\mathbf{s}_d = \frac{\mathbf{r}_d}{|\mathbf{r}_d|}$. This scheme is illustrated in Fig. 3.7. Note that we use the dipole approximation and assume $\mathbf{r}_j(t) = \mathbf{r}_j(0)$. The physical meaning is that a released electron stays in the vicinity of the atom and does not experience the entire structure of the twisted light field. This assumption is reasonable, since the electron classically only moves about 2 nm, which is small compared to the wave length of the driving beam, as shown in Sec. 3.1.3. Therefore, we consider each single atom to be just locally exposed to a plane wave field.

In order to compute the harmonic signal at the detector we first discretize the detector. For a given detector position $\mathbf{r}_d$, we have to compute the harmonic signal from each radiator and propagate it to the detector. Thus, we have to calculate the time, it takes for the radiation to go from the atom to the detector $\tau = \frac{|\mathbf{r}_d - \mathbf{r}_j|}{c}$, where we assume that the radiation travels at the speed of light. Then we calculate the dipole acceleration starting from $t = -\tau$ for a specific number of discrete time

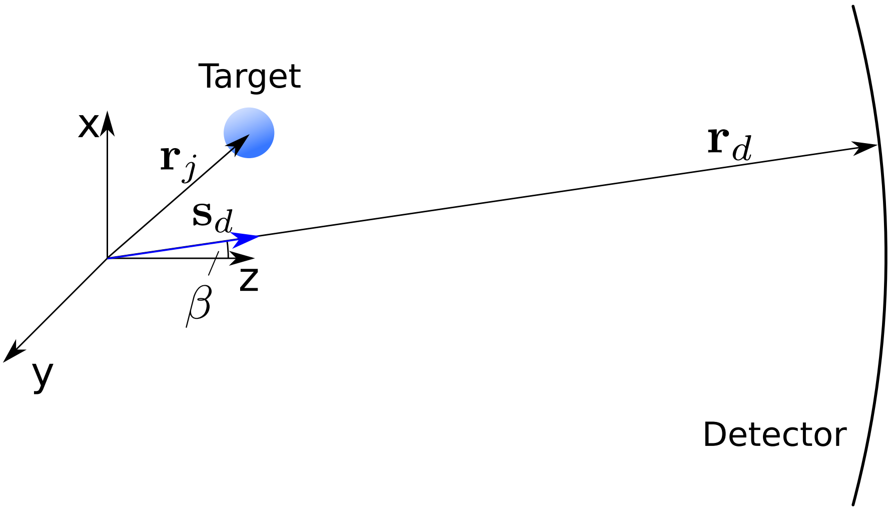

Figure 3.7: Scheme to compute the numerical propagation of high harmonic radiation. The driving beam propagates in z-direction. The origin of our coordinate system is in the focus of the beam. The simulated cloud of atomic targets consists of multiple atoms placed at different positions $\mathbf{r}_\mathrm{j}$, as indicated by the blue "atom". At each detector position $\mathbf{r}_\mathrm{d}$ we compute the electric field as a superposition of all single atom contributions in the atomic cloud.

steps. Finally, we use these calculated values of the dipole acceleration in Eq. 3.46 to calculate the electric field at the detector position $\mathbf{r}_\mathrm{d}$ and store these values for the electric field in an array. We proceed the same way for each radiator in the atomic gas target and add up the values for the electric field coherently at the detector position $\mathbf{r}_\mathrm{d}$. After we calculated the harmonic signal at detector position $\mathbf{r}_\mathrm{d}$, we step to the next detector position until we finished the calculation for the whole detector.

4

HIGH-HARMONIC GENERATION WITH LINEARLY POLARIZED LAGUERRE-GAUSSIAN BEAMS

In this chapter we discuss the HHG of atomic targets in linearly polarized fields. We will first analyze the calculated harmonic spectrum generated by a single atom. Then, we extend this analysis and take extended target into account. In particular, we focus on the OAM of the generated harmonics and methods how to control this OAM. Moreover, we will also analyze phase matching in LG beams and identify the best positions for the atomic target in order to get the "brightest" signal at the detector.
Some of the material in this chapter has appeared previously in references

> *High harmonic generation with Laguerre–Gaussian beams*
> Paufler, W., Böning, B., Fritzsche, S.
> *Journal of Optics*, **21**(9), 094001 (2019)
>
> *Coherence control in high-order harmonic generation with Laguerre-Gaussian beams*
> Paufler, W., Böning, B., Fritzsche, S.
> *PHYSICAL REVIEW A*, **100**, 013422 (2019)

4.1 SINGLE ATOM RESPONSE TO A LINEARLY POLARIZED FIELD

Within this section we discuss the HHG of a single atom irradiated by an intense linearly polarized laser field. Even though, HHG by one single atom has never been experimentally observed and the emitted radiation would be far too low for any physical applications, its discussion still provides a qualitatively good insight to the spectrum of the emitted harmonics.
In Fig. 4.1, we show a typical spectrum of emitted harmonics in a linearly polarized laser field. Here, we chose a hydrogen $1s$ wave function, a wavelength of $800\,\mathrm{nm}$ and an intensity of $10^{14}\,\mathrm{W/cm^2}$. The spectrum shows a broad comb of harmonics of the driving laser, where notably every second harmonic is suppressed. The odd harmonics build up an extended plateau, where all harmonics are emitted at similar intensities. The plateau extends up to the harmonic cutoff, where the harmonic

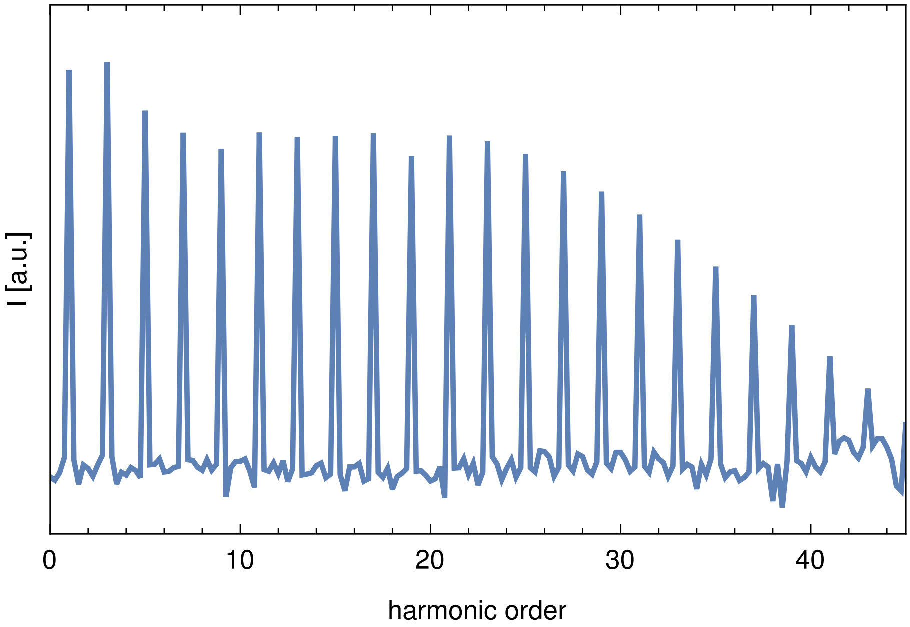

Figure 4.1: Characteristic spectrum of high-harmonics generated by a linearly polarized 800 nm laser with intensity 10^{14} W/cm² in an arbitrary logarithmic scale. The spectrum exhibits the characteristic plateau of several harmonics that are emitted at similar intensities and the subsequent exponential harmonic cutoff around the 21^{st} harmonic. The calculation has been performed with the RB-SFA code [70].

intensity drops down exponentially. In this example, the classical harmonic cutoff (Eq. 3.11) is given by

$$n_{\max}\omega \approx I_p + 3.17U_p \approx 22\omega. \tag{4.1}$$

The occurrence of only odd harmonics and the suppression of all even ones, respectively can be explained in multiple ways.

First, we may investigate the symmetry of the time dependent dipole moment (Eq. 3.37), which satisfies

$$\mathbf{D}(t) = -\mathbf{D}(t + T/2), \tag{4.2}$$

where $T = \frac{2\pi}{\omega}$ is the cycle length of the driving laser. The left column of Fig. 4.2 shows one cycle of the x-component of the time dependent dipole moment (blue) combined with the oscillation of a first[1] and second harmonic. Thereby the choice of the first and second harmonic is arbitrary, however, low-harmonic orders make this example much more vivid than high-harmonic orders. The Fourier transform of the time dependent dipole moment reveals the spectrum of the contributing

---

[1] Of course, a first harmonics makes no sense, since it would be just the driving beam. However, to explain the suppression of all even harmonics, it is quite vivid and reasonable.

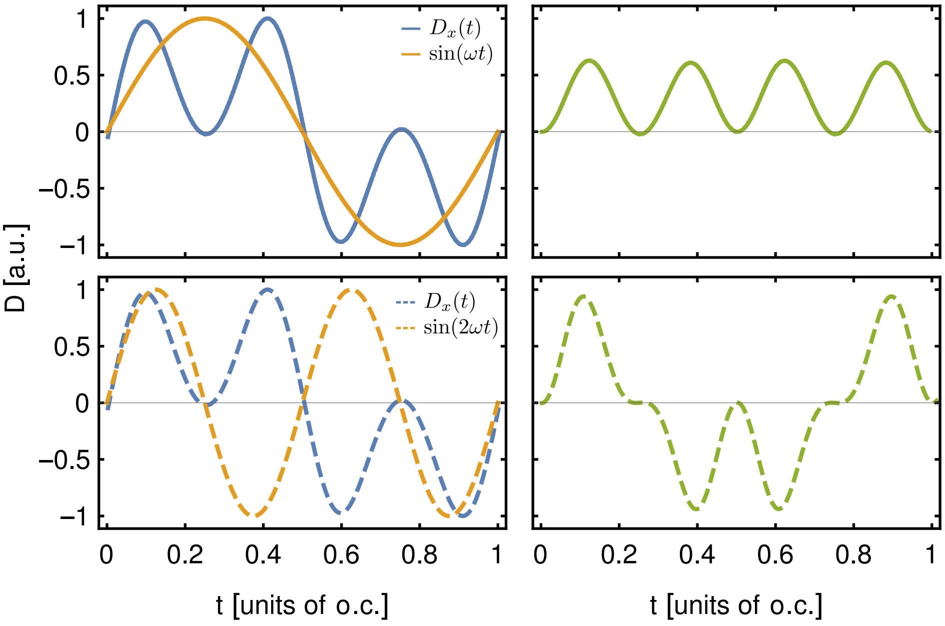

Figure 4.2: Illustration of the Fourier transform of the time dependent dipole moment for an odd (upper row) and an even (bottom row). The time dependent dipole moment is shown in blue, while the odd (even) function is shown in yellow. The Fourier coefficients can be computed from the integral over the product of the dipole moment and the odd (even) function, which is shown as in the right part as the green curve.

harmonics. Especially, the first Fourier coefficient is the integral over the product of the time dependent dipole moment and the oscillation of the first harmonic. This product is shown in the right column (solid green line). It is clearly visible that the integral over this product will be nonzero. We can apply a similar argument to the second harmonic, in terms of the second Fourier coefficient. However, the integral over the product of the dipole moment and the oscillation of the second harmonic (green dashed line) will be zero. More generally, the Fourier transform of any function with the symmetry from Eq. 4.2 reveals only odd Fourier coefficients, which implies that only odd harmonics are generated.

Another explanation can be provided in terms of an intuitive photon picture. Each photon has a SAM either plus or minus one[2], which can be associated with the polarization. Linearly polarized light can be considered as an evenly distributed composition of photons with SAM of plus and minus one. If an electron absorbs several photons, the SAM of the photons add up. Therefore, after the absorption of an even number of photons, it is not possible to emit the absorbed energy in terms of a single photon, because this single photon's SAM could not be plus and minus one. This only can be achieved after the absorption of an odd number of photons. Therefore, only odd harmonics contribute to the spectrum, while all even harmonic orders are strictly suppressed. This can be summarized by our notation for HHG that will be used throughout the thesis as:

---

[2] in atomic units $\hbar = 1$

$$\mathrm{LG}_{0,0}^{\omega\leftrightarrow} \quad \xrightarrow{\mathrm{HHG}} \quad \begin{aligned} \omega_{\mathrm{H}_q} &= q,\, \omega \\ q &= \text{odd}. \end{aligned} \tag{4.3}$$

Here the arrow ↔ indicates the linear polarization of the driving beam and ω_{H_q} denotes the energy of the q^{th} harmonic.

4.2 EXTENDED TARGETS IN LINEARLY POLARIZED LG BEAMS

4.2.1 *Conservation of OAM*

The first experiment on HHG with linearly polarized LG beams was done in 2012 by Zürch *et al.* [71]. Here they used a driving beam with topological charge (or OAM) of $\ell = 1$. Surprisingly, they found that the measured topological charge of all harmonics was equal to one. This was a contradiction to their expectations from second harmonic generation [72] and the Lewenstein model [9], which both predict that the OAM of a q^{th} harmonic order is q times the OAM of the driving field. Zürch *et al.* explained this puzzling fact by a decay of the initially generated highly charged vortices into singly charged vortices as they propagate to the detector.
Thereafter, Hernández-García *et al.* developed an algorithm to simulate HHG in atomic gas jets and to propagated the generated radiation at each position in the gas jet to the detector [68, 69]. Here, they theoretically showed that the highly charged vortices survive propagation and that a q^{th} harmonic generated by a LG beam with topological charge $\ell = 1$ has OAM of q. In 2014, Gariepy *et al.* finally experimentally confirmed these theoretical predictions [73]. We can express the conservation of energy and OAM in HHG with linearly polarized LG beams as:

$$\mathrm{LG}_{\ell,0}^{\omega\leftrightarrow} \quad \xrightarrow{\mathrm{HHG}} \quad \begin{aligned} \omega_{\mathrm{H}_q} &= q\,\omega, \\ q &= \text{odd}, \\ \ell_{\mathrm{H}_q} &= q\,\ell. \end{aligned} \tag{4.4}$$

In Fig. 4.3, we show the calculated far-field phase profiles of a 11^{th} and 13^{th} harmonic. Here we used the Fraunhofer diffraction formula (Eq. 3.45) to calculate the phase profiles in the far-field. We can obtain the OAM of the generated harmonics

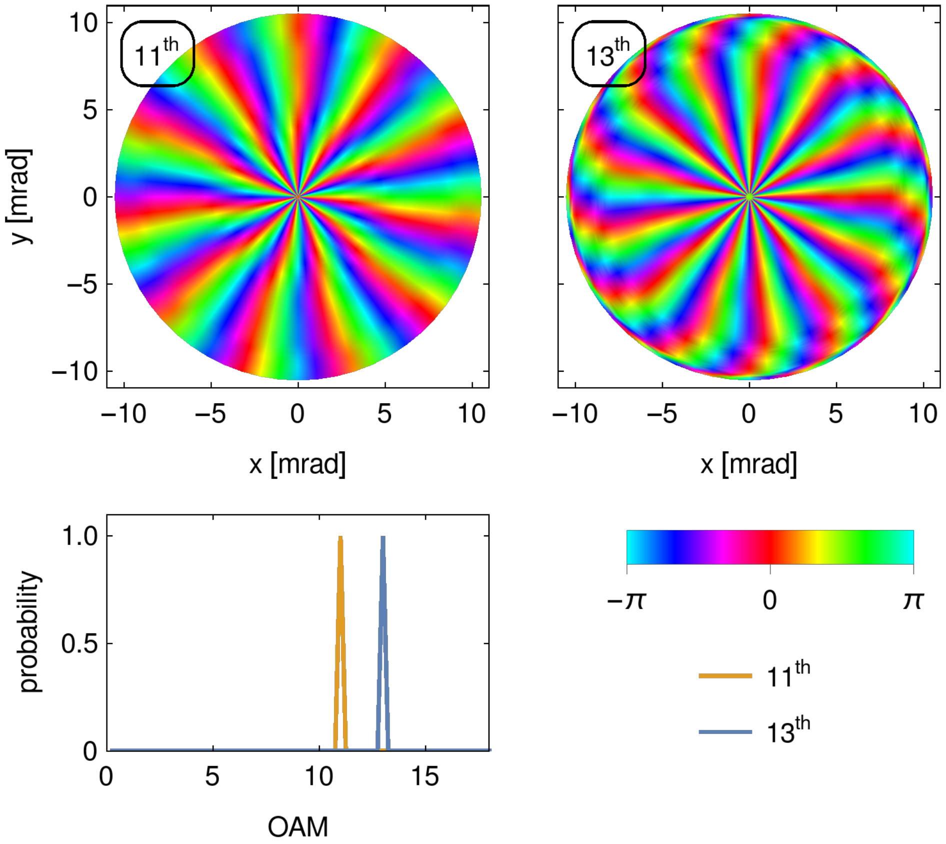

Figure 4.3: Top: The phase profiles for the 11^{th} and 13^{th} harmonic at the detector generated by a linearly polarized LG beam with $\ell = 1$. The OAM (number of phase shifts of 2π) is equal the harmonic order. Bottom left: OAM of the 11^{th} (blue) and 13^{th} (red) harmonic calculated by a Fourier transform along the azimuthal coordinate.

if we count the number phase shifts of 2π along the azimuth, which is 11 of the 11^{th} and 13 for the 13^{th} harmonic. A more precise way to calculate the OAM of the harmonics is an azimuthal Fourier transform of the the far-field phase profiles for a fixed angle of divergence β and afterwards to integrate over all values of β. As shown in the bottom row of Fig. 4.3, the results obtained by an azimuthal Fourier transform agree with those from counting the phase shifts of 2π.

4.2.2 *Divergence of the harmonics*

In addition to the phase profiles, the intensity profiles play an important role for the analysis of HHG with LG beams. These intensity profiles allow to estimate the divergence of the generated harmonics.

In Sec. 2.2.3, we reported on different ways to define the divergence of the LG beams.

However, we showed that the values for the divergence defined by the radius of maximal intensity and the standard deviation of the intensity distribution approach each other as the OAM increases. Thus it is reasonable to estimate the divergence of the harmonics by analyzing the radius of the first maximum in the far-field intensity profile. Fig. 4.4 shows that the maxima of the 11^{th} and 13^{th} harmonics occur at similar values of β, which means that their divergence is similar to each other.

Generally, we can use the Fraunhofer diffraction formula to analyze the radius of the first maximum in far-field. Within the Lewenstein model for HHG, we can express the near-field amplitude of a q^{th} harmonic as

$$A_q^{(\mathrm{near})}(\rho', \varphi') = f(\rho') e^{iq\ell\varphi'}, \tag{4.5}$$

where all radial dependencies are included in $f(\rho')$. If we insert Eq. 4.5 into the Fraunhofer diffraction formula (Eq. 3.45), we can evaluate the integral over the azimuthal angle φ' analytically [74] and we obtain the following expression for the far-field amplitude:

$$A_q^{(\mathrm{far})}(\beta, \varphi) = 2\pi i^{q\ell} e^{iq\ell\varphi} \int_0^\infty d\rho' \rho' f(\rho') J_{q\ell}\left(\frac{2\pi}{\lambda_q}\beta\rho'\right). \tag{4.6}$$

Here λ_q is the wavelength of the q^{th} harmonic and $J_k(x)$ is a Bessel function of the first kind. The value β_{max} for which the far-field amplitude reaches its maximum can be seen as a measure of the divergence of each harmonic order. From the Bessel function in Eq. 4.6 we can extract the change of the divergence with the harmonic order. The order of the Bessel function increases with the harmonic order, which shifts the value of β_{max} to larger values. However, the argument of the Bessel function increases similarly with the harmonic order, which shifts the value of β_{max} to smaller values. Roughly speaking, different harmonics are emitted are emitted with similar divergence [65, 69], which can be seen in the lower left part of Fig. 4.4.

4.3 PHASE MATCHING

Of course, the harmonic radiation emitted by a single atom is far too low for any experiment and thus dense atomic targets $\sim 10^{16}\,\mathrm{atoms}\cdot\mathrm{cm}^{-3}$ are typically used to generate high-order harmonics. In order to make HHG efficient, it is required to analyze the macroscopic interplay of all the individual atomic responses to the driving laser field. The investigation of the macroscopic superposition of all the

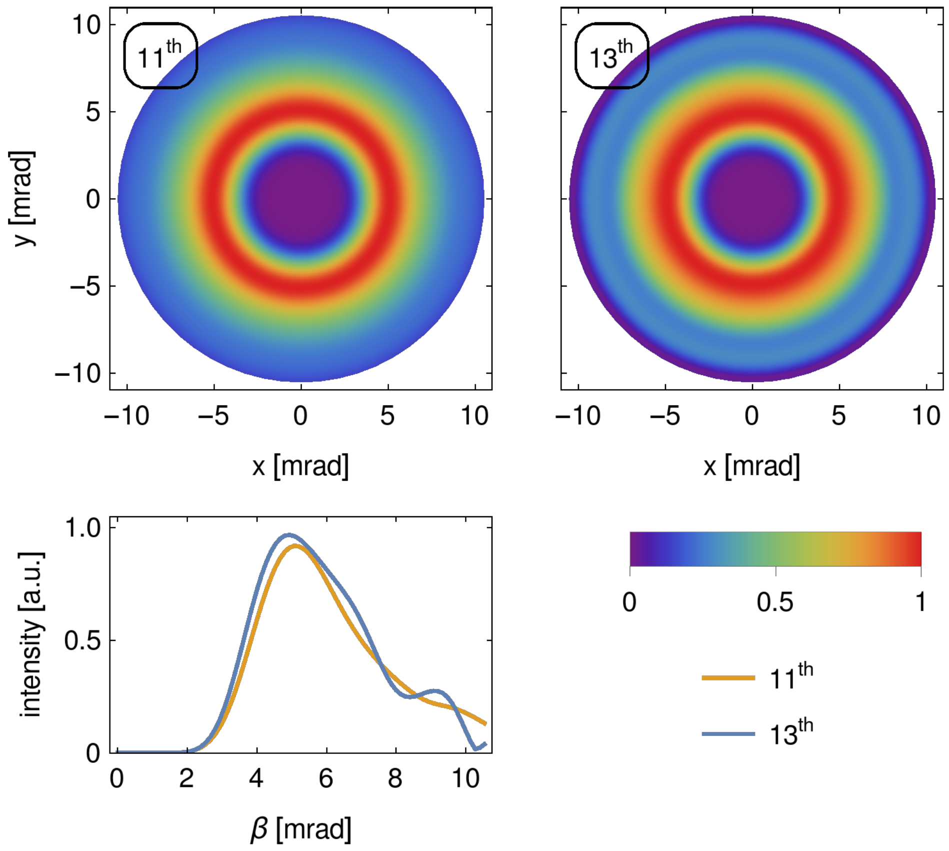

Figure 4.4: Top: The intensity profiles for the 11th and 13th harmonic at the detector generated by a linearly polarized LG beam with $\ell = 1$. Bottom left: Cut through the intensity profiles of the 11th and 13th harmonic. The maximum of the intensity profiles is set to one.

single atom responses helps to determine the phase and intensity profiles at the detector and also to increase the conversion efficiency. For the latter one, we have to ascertain especially that the single atom responses to the driving laser fields add up *constructively* at the detector and consequently increase the conversion efficiency of selected harmonics.

A typical size of a driving volume, respectively the area with sufficient intensity, for HHG in a Gaussian beam is a cylinder with a length of 7 mm and a radius of 30 µm and, thus, about 10^{12} atoms could be placed in the interaction region. Notably, for LG beams this cylinder would rather be a hollow cylinder.

Generally, the radiation emitted by different atoms in the interaction region is not in phase. Thus, we have to identify areas in the interaction region, where the harmonics are emitted in phase. Only then, the radiation adds up constructively at the detector, which we call good conditions for phase matching. In order to know whether the harmonics are emitted in phase in a given area in the interaction re-

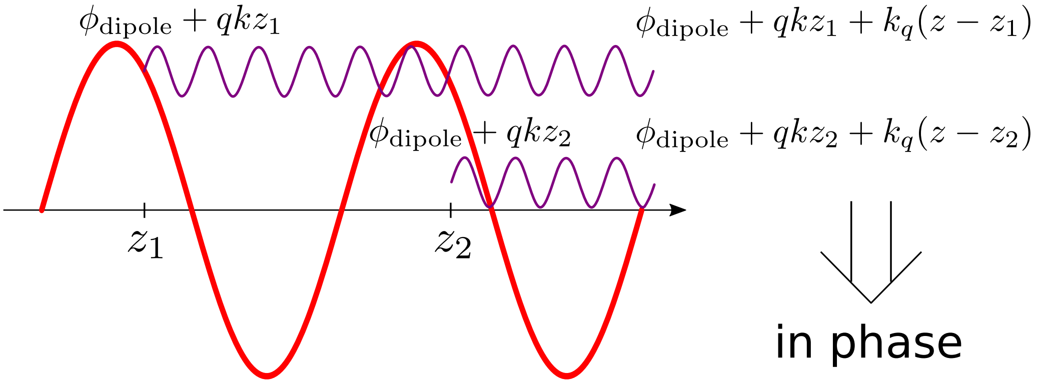
$\phi_{\text{dipole}} + qkz_1$
$\phi_{\text{dipole}} + qkz_1 + k_q(z - z_1)$
$\phi_{\text{dipole}} + qkz_2$
$\phi_{\text{dipole}} + qkz_2 + k_q(z - z_2)$
z_1
z_2
in phase

Figure 4.5: Phase matching for HHG in a plane wave field. The plane wave driving field propagates in z-direction. Harmonics emitted from different positions z_1 and z_2 are in phase if we assume that the radiation propagates at the speed of light and the wave number of the q^{th} harmonic $k_q = q \cdot k$, where k is the wave number of the driving beam.

gion, we first have to know the phase of each harmonic as emitted by the target atoms.

So far, phase matching has been mainly investigated in several studies for Gaussian beams [75–77]. In this section, we will now discuss phase matching for linearly polarized LG beams. Here, we will focus on two main contributions that determine the phase of the emitted harmonic field at the various positions of the target:

- the dipole phase due to the response of a single atom to local intensity of the laser,
- the intrinsic beam phase due to the focusing of the laser beam, such as the Gouy and focal phase.

In Fig. 4.5, we show a simplified picture for phase matching in plane wave fields. There are no intrinsic beam phases. In addition, the intensities of plane waves are constant as they propagate, which results in a constant dipole phase. Harmonics generated at z_1 inherit the dipole phase and q times the local phase of the electric field due to the absorption of q photons. The dipole phase is the same for harmonics generated at different positions in a plane wave. Here, we assume that the harmonic radiation and the driving beam propagate at the speed of light. The phase of a q^{th} harmonic generated at z_1 can be written as

$$\phi_{z_1} = \phi_{\text{dipole}} + qkz_1. \tag{4.7}$$

Similarly we express the phase of a q^{th} harmonic generated at z_2 as

$$\phi_{z_2} = \phi_{\text{dipole}} + qkz_2. \tag{4.8}$$

If these harmonics then propagate towards the detector, the phases change as

$$\phi_{z_1}(z) = \phi_{\text{dipole}} + qkz_1 + k_q(z - z_1), \tag{4.9}$$
$$\phi_{z_2}(z) = \phi_{\text{dipole}} + qkz_2 + k_q(z - z_2). \tag{4.10}$$

If we use the relation $k_q = qk$, the generated radiation will add up constructively at a detector placed at z_d, since $\phi_{z_1}(z_d) = \phi_{z_2}(z_d)$. This results in ideal conditions for phase matching for plane waves. The intensity of the harmonics measured at the detector will increase linearly with the size of the atomic target.

However, generally the assumption of a uniform intensity profile is not justified, therefore the dipole phase will be position dependent. Furthermore, the intrinsic beam phases, the Gouy and focal phase, also have to be included. Here it becomes clear, that phase matching is generally a much more complex issue than for the simple plane wave example.

The total phase for the q^{th} harmonic can be expressed as [40, 77, 78]

$$\phi_q(\rho, z) = \phi_{q,\text{dipole}}(\rho, z) - q\phi_{\text{intrinsic}}(\rho, z). \tag{4.11}$$

Here, we consider phase matching in the absence of dispersive effects, such as the change of the refraction index due to the occurrence of free electrons in the interaction region. We can calculate the change of the phase for each harmonic order in dependence on the coordinates of the emitting atom, in particular, we define this phase change in terms of a mismatch of the wave vectors by [76]:

$$\nabla\phi_q(\rho, z) = \partial_\rho\phi_q(\rho, z)\mathbf{e}_\rho + \partial_z\phi_q(\rho, z)\mathbf{e}_z. \tag{4.12}$$

Here, we just consider mismatch in transverse and longitudinal direction and omit the azimuthal mismatch. The change of the azimuthal phase has to be considered if we want to calculate the far-field phase profiles, as we did in Sec. 4.2.1. However, here we focus on the conversion efficiency of the harmonics.

Moreover, the length of the spatial interval in the interaction region, where the generated harmonic radiation adds up constructively, is called *coherence length*. The coherence length is generally defined as [76, 77]

$$L_{\text{coh}} = \frac{\pi}{|\nabla\phi_q(\rho, z)|}. \tag{4.13}$$

4.3.1 *Dipole phase*

In experiments, the intensity distribution of the driving laser is generally not uniform, as assumed for the idealized case of a plane wave beam. As an example, we show transverse and longitudinal cross sections of the intensity profiles for a Gaussian and a LG beam with $\ell = 1$ in Fig. 4.6. Atoms from an extended gas target that interact with the laser are therefore exposed to different local intensities at different positions. Since the intensity affects the dipole phase of a given harmonic order, atoms at different positions may emit this harmonic with different dipole phases. Of course, this then also affects phase matching. Therefore it is important to investigate how the intensity profile of the driving laser affects phase matching and the coherence length.

If we follow the three step model, a released electron is driven by the electric field of the laser and may come back to the parent ion to recombine. During its propagation and subsequent recombination the electron accumulates a phase that can be calculated with Eq. 3.31. This phase is called the dipole phase.

For those harmonics that contribute to the plateau, there are two different quantum orbits, which are labeled as short and long trajectories with respect to their travel time. The dipole phase of the short trajectories is different from the dipole phase of the long trajectories because of their different travel times, respectively time that they are driven by the laser field. If we decrease the intensity of the driving laser, a harmonic that contributes to the plateau tends towards the harmonic cutoff. The more a harmonic approaches the cutoff, the more the dipole phases of the long and short trajectories approach each other. If the intensity reaches the cutoff intensity I_c for the q^{th} harmonic, $3.17\frac{I_c}{4\omega^2} + I_p = q\omega$, both the short and long trajectory have the same dipole phase.

In Fig. 4.7, we show the dipole phase for the long and short trajectories for the example of a 21^{st} harmonic order as a function of intensity of the driving laser[3]. Here, we show both, the phase of the quantum orbits as well as the phase for the classical trajectories. As seen from this figure, the dipole phase for the short as well as for the long trajectory increases with the intensity. However, the dipole phase for the long trajectory is more sensitive to the intensity than the dipole phase for the short trajectory. For both trajectories, we can find a linear dependence of the dipole phase on the intensity [65, 79, 80]. We write

$$\phi_{q,\text{dipole}} = \alpha_i^q \cdot I, \tag{4.14}$$

---

[3] More precisely, the local intensity at the position of the atom

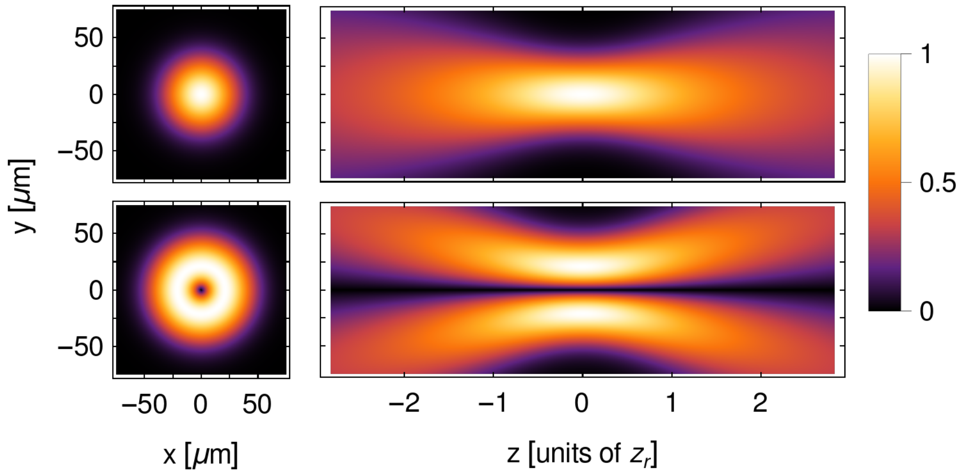

Figure 4.6: Transverse (left) and longitudinal (right) cross sections of the intensity profiles of a Gaussian beam (upper row) and a LG beam with OAM $\ell = 1$ (lower row). Both beams propagate in z-direction. The Gaussian beam has its transverse intensity maximum exactly on the axis of propagation. However the transverse intensity maximum for the LG beam is off-axis and has zero intensity on the beam axis.

where the subscript $i = s, l$ denotes the short and long trajectory, respectively. We use the slopes from our quantum orbit calculations $\alpha_s^{21} = 1.5 \cdot 10^{-14}\,\text{cm}^2/\text{W}$ and $\alpha_l^{21} = 22 \cdot 10^{-14}\,\text{cm}^2/\text{W}$.

4.3.2 *Intrinsic beam phases*

In addition to the inhomogeneous intensity profile of the driving laser, the intrinsic phases[4] of the beam also influence the phase of the generated harmonics. Here we consider two important contributions to the intrinsic phase $\phi_{\text{intrinsic}}$. The first one is the Gouy phase. It has been theoretically predicted and experimentally confirmed by Louis Georges Gouy in 1890 [39, 81]. For a Gaussian beam this phase contributes a phase shift from $\frac{\pi}{2}$ to $-\frac{\pi}{2}$ as the beam propagates from negative to positive infinity. Mathematically it can be approximated by

$$\phi_{\text{Gouy}} = -\arctan\left(\frac{z}{z_r}\right). \tag{4.15}$$

---

[4] also called geometric phases

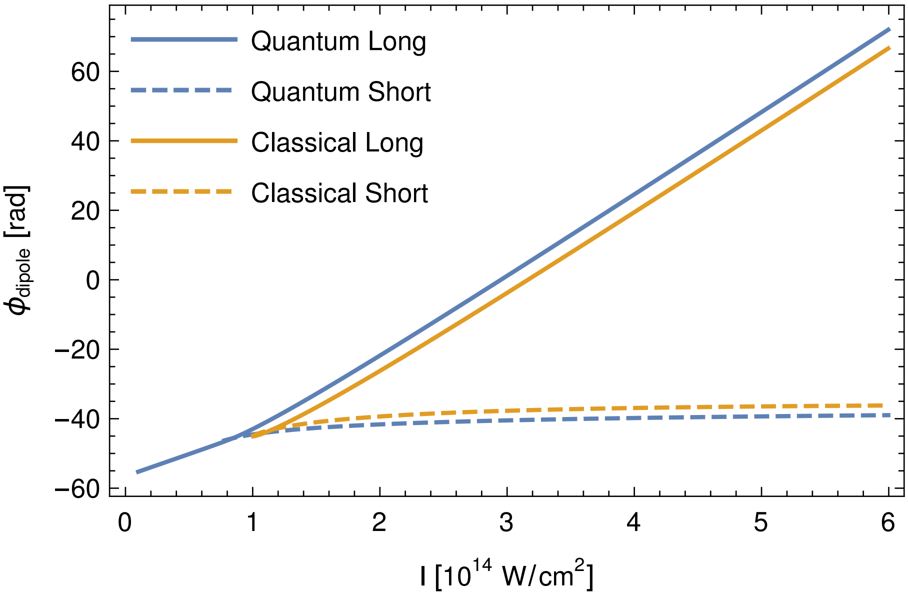

Figure 4.7: Dipole phase for an electron depending on intensity for short (dashed) and long solid trajectories that contribute to the 21^{st} harmonic. We calculated the dipole phase by means of classical trajectories (yellow) and quantum orbits (blue). The cutoff intensity I_c for the 21^{st} harmonic is near 10^{14} W/cm². For intensities higher than I_c, the dipole phase for short and long trajectories increases linearly with intensity.

For LG beams, however, this phase shift increases to

$$\phi_{\text{Gouy}} = -(2p + |\ell| + 1) \arctan\left(\frac{z}{z_r}\right) \tag{4.16}$$

and thus contributes a phase shift of $(|\ell| + 1)\pi$ if $p = 0$.

The second contribution arises from the curved wavefronts of Gaussian and LG beams [82]. The focal phase, can be expressed as $\phi_{\text{focal}} = k\frac{\rho^2}{2R(z)}$ and is independent of the OAM of the beam. The azimuthal phase $\ell\varphi$ only depends on the azimuthal coordinate and therefore does not affect longitudinal (z-direction) and transverse (ρ-direction) phase matching.

In Fig. 4.8, we show the transverse and longitudinal cross sections of the phase profiles for a Gaussian and LG beam with $\ell = 1$. The transverse phase profile for the Gaussian beam shows the plane wave behavior near the focus while for the LG beam it shows the characteristic phase shift of $2\pi \cdot \ell$. The longitudinal phase profile of the Gaussian beam exhibits the phase shift from $\frac{\pi}{2}$ to $-\frac{\pi}{2}$ on the beam axis due to the Gouy phase. The focal phase modifies the phase off axis. The phase profile of the LG beam has a phase singularity on the propagation axis due to the azimuthal phase. In addition, the phase shift caused by the Gouy phase is increased to a phase shift from π to $-\pi$.

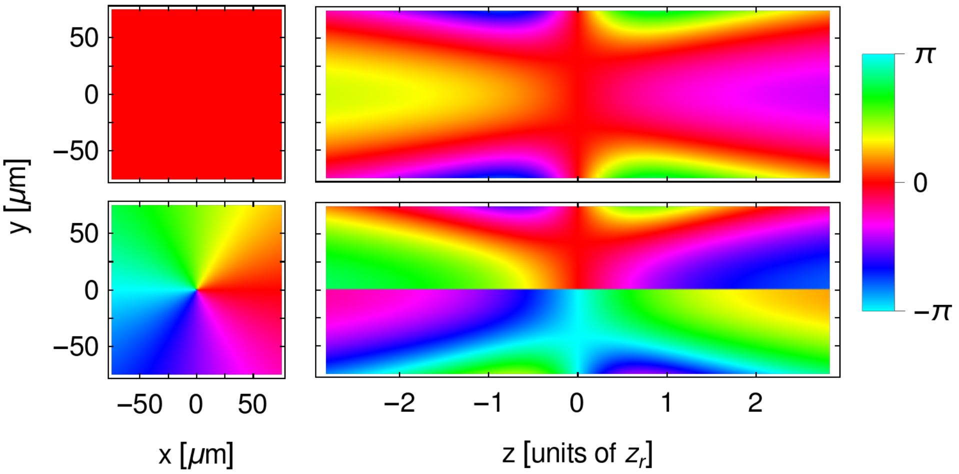

Figure 4.8: Transverse (left) and longitudinal (right) cross sections of the intensity profiles of the Gaussian beam (upper row) and a LG beam with OAM $\ell = 1$ (lower row). Both beams propagate in z-direction. For reasons of clarity, we omitted the phase term kz.

4.3.3 *Phase matching on maximum*

4.3.3.1 *A one dimensional model*

A simple model to investigate phase matching for Gaussian beams, is known as *phase matching on axis* [83]. Within this model it is assumed that harmonics are only emitted from the beam axis, since there is the intensity maximum in a transverse cross section of the beam and therefore the largest contribution to HHG. However, the intensity of LG beams with nonzero OAM is zero on the beam axis and of course no harmonics are generated in this region of the beam. This makes *phase matching on axis* inapplicable for LG beams. We therefore extend this model and generalize *phase matching on axis* from Gaussian beams to phase matching on the (first) transverse intensity maximum for LG beams. We will refer to this model shortly as *phase matching on maximum* [84].

The radial coordinate of the first intensity maximum of a $\mathrm{LG}_{\ell,0}$ beam can be calculated by $\frac{\partial u_{\ell,0}}{\partial \rho} = 0$ and is equal to

$$\rho_{\ell,\max}(z) = \sqrt{\frac{|\ell|}{2}}\, w(z) = \sqrt{\frac{|\ell|}{2}} w_0 \sqrt{1 + \frac{z^2}{z_r^2}}. \qquad (4.17)$$

Of course, for beams with zero OAM, we get $\rho_{0,\max}(z) = 0$, which coincides with the beam axis. Notably, the intensity on the maximum is independent of the OAM and is given by

$$I(z) = \frac{I_0}{1 + \frac{z^2}{z_r^2}}, \tag{4.18}$$

where I_0 is the peak intensity in the focus plane. For a Gaussian beam the total phase $\phi_q(z)$ on maximum for the q^{th} harmonic on axis is given by [40]

$$\begin{aligned}\phi_q(z) &= \phi_{q,\text{dipole}}(z) - q\phi_{\text{Gouy}}(z) \\ &= \alpha_{s,l} I(z) + q \arctan\left(\frac{z}{z_r}\right).\end{aligned} \tag{4.19}$$

Similarly, we analyze the phase for LG beams with nonzero OAM on the first maximum. Since the radial coordinate of the first maximum is nonzero, the focal phase, which arises from the curved wavefronts, contributes to the total phase. The total phase on the maximum for the q^{th} harmonic for a LG beam can be expressed as

$$\begin{aligned}\phi_q(z) &= \phi_{q,\text{dipole}}(\rho_{\ell,\max}(z), z) - q\phi_{\text{Gouy}}(z) - qk\frac{\rho_{\ell,\max}^2(z)}{2R(z)} \\ &= \alpha_{s,l} I(z) + q(|\ell| + 1) \arctan\left(\frac{z}{z_r}\right) - q\frac{|\ell| z}{2z_r}.\end{aligned} \tag{4.20}$$

Notably, Eq. 4.20 simplifies to Eq. 4.19 if the OAM ℓ is equal to zero. In order to have perfect phase matching conditions for the q^{th} harmonic, the total phase $\phi_q(z)$ should be constant in spatial regions of the driving volume of the beam. Within our *phase matching on maximum* model we write this condition as

$$\frac{\partial \phi_q(z)}{\partial z} = 0. \tag{4.21}$$

Analogously to Eq. 4.12, the left hand side of Eq. 4.21 is also called the mismatch of the wave vector in longitudinal direction.

However, this condition will be only fulfilled at discrete spatial points in the interaction region. Generally speaking, we have good phase matching conditions if the longitudinal wave vector mismatch approaches zero or, in other words if the phase of the emitted harmonics is nearly constant within a large interval in the interaction region. Still, the solution of Eq. 4.21 is a good approach to find regions in the beam, where phase matching can be achieved and thus harmonics can be generated efficiently.

Within this one dimensional model we will extract the coherence length from the

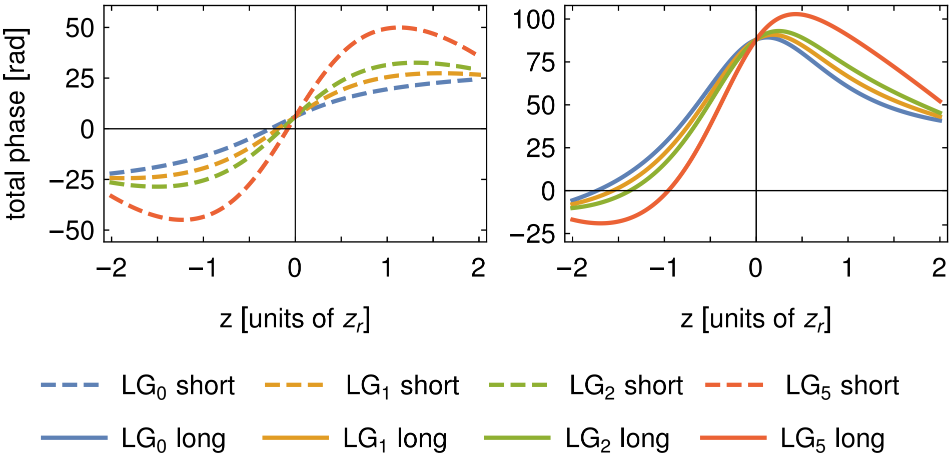

Figure 4.9: The total phase for the short (left) and long (right) trajectories depending on the z-coordinate. Different LG beams are denoted by different colors. The peak intensity at the focus $z = 0$ is $4 \cdot 10^{14}\,\mathrm{W/cm^2}$ and the Rayleigh range is $z_r = 3.5\,\mathrm{mm}$. The results are calculated by means of Eq. 4.19 and Eq. 4.20.

longitudinal wave vector mismatch and define the coherence length at a position z_0 as maximal extent of a target at z_0, such that the total phase within this target changes by less than π. We always choose the target to be symmetric around the position z_0. This definition is different from the commonly used definition (c.f. Eq. 4.13), but it is a more physical one.

4.3.3.2 *Total phase*

Let us now discuss the behavior of the total phase of the emitted harmonics within our one dimensional model. In Fig. 4.9, we show the total phase of the short (left) and the long (right) trajectories of 21$^{\mathrm{st}}$ harmonic for various LG beams with different OAM ℓ depending on the z-coordinate. Negative values of z refer to the region before the focus, $z = 0$ is exactly at the focus and $z > 0$ means behind the focus with respect to the propagation of the beam. Each beam has a peak intensity of $4 \cdot 10^{14}\,\mathrm{W/cm^2}$, a wavelength of 800 nm and a Rayleigh range of $z_r = 3.5\,\mathrm{mm}$. Within two Rayleigh ranges before and behind the focus the intensity is high enough, so that the 21$^{\mathrm{st}}$ harmonic still belongs the the harmonic plateau. Outside of this interval, the intensity is too low to efficiently create the 21$^{\mathrm{st}}$ harmonic.

At the focus there is the highest intensity and therefore also the highest dipole phase. If we move away from the focus plane, the intensity on the radial maximum decreases. Since the dipole phase is proportional to the intensity, the dipole phase decreases with the distance from the focus plane as well. This implies that the contribution of the dipole phase to the longitudinal wave vector mismatch is positive before and negative if the target is placed behind the focus. In contrast to the dipole phase, the contribution of the Gouy phase to the mismatch is always positive.

SHORT TRAJECTORIES For the short trajectories, the contribution of the dipole phase to the total phase is small compared to the contribution of the Gouy phase. The focal phase vanishes on the beam axis, therefore it does not contribute to the total phase on maximum for a Gaussian beam. Here the total phase has the shape of an arc-tangent function with a small offset, where the offset is due to the dipole phase.
For a LG beam with nonzero OAM, the intensity maximum is off axis, which leads to a contribution of the focal phase to the total phase. Furthermore, the Gouy phase shift across the focus increases if the beam has nonzero OAM. However, the sign of the focal phase is opposed to the sign of the Gouy phase and therefore counteracts the increasing contribution of the Gouy phase to the total phase. The comparison of the total phase for the short trajectories of different beams shows that the slope of the total phase, respectively the longitudinal wave vector mismatch increases across the focus as the OAM of the beam increases. However, the interplay of Gouy and focal phase gives rise to regions at $z \approx \pm z_r$, where the total phase is stationary. In these regions the condition for perfect phase matching (Eq. 4.21) is fulfilled.

LONG TRAJECTORIES The total phase of the long trajectories is more affected by the dipole phase than the total phase of the short trajectories, because $\alpha_l > \alpha_s$, while the Gouy and the focal phase contribute equally to both trajectories. For the long trajectories, the total phase is dominated by the dipole phase, which is, on maximum, the same for all $\mathrm{LG}_{\ell,0}$ beams. Therefore the plots of the total phase have a similar characteristic shape for all four beams, as shown in the right part of Fig. 4.9. For every beam, the total phase for the long trajectories has a stationary point behind the focus. At this point the condition for perfect phase matching is fulfilled. Notably, it moves away from the focus plane as the OAM increases.

4.3.3.3 *Coherence length*

In Fig. 4.10, we display the coherence length for the example of the 21^{st} harmonic generated by the short (left) and long (right) trajectories at the first maximum depending on a displacement of the atomic target with respect to the focus plane at $z = 0$.

SHORT TRAJECTORIES The coherence length of the 21^{st} harmonic created by the short trajectories near the focus plane decreases with the OAM of the driving

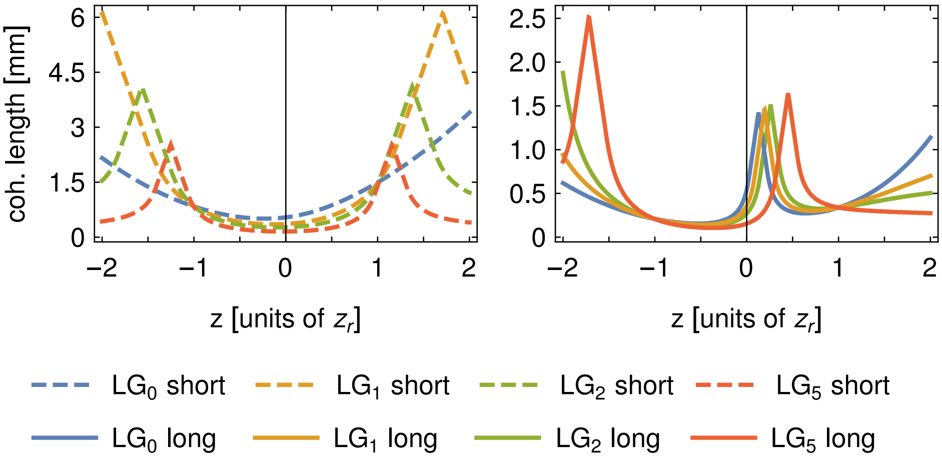

Figure 4.10: Coherence length for the short (left) and long (right) trajectories depending on the z-coordinate. Different LG beams are denoted by different colors. The peak intensity at the focus $z = 0$ is $4 \cdot 10^{14}\,\mathrm{W/cm^2}$ and the Rayleigh range is $z_r = 3.5\,\mathrm{mm}$.

beam, due to the increased Gouy phase shift across the focus. However, about one Rayleigh range off the focus plane, the contributions of the Gouy phase and the focal phase cancel each other, which results in a large coherence length.

LONG TRAJECTORIES For the contribution of the long trajectories to the 21^{st} harmonic, we find a large coherence length shortly behind the focus for all beams. Furthermore, the coherence length slightly increases behind the focus with the OAM, as expected from the discussion of the total phase.

4.3.3.4 *Perfect phase matching*

Let us now discuss the positions of perfect phase matching according to Eq. 4.21. For Gaussian beams these positions can be found analytically as solutions to

$$\tilde{z}^2 - 2\frac{\alpha_{s,l} I_0}{q}\tilde{z} + 1 = 0 \tag{4.22}$$

whose are given by

$$\tilde{z} = \frac{\alpha_{s,l} I_0}{q} \pm \sqrt{\left(\frac{\alpha_{s,l} I_0}{q}\right)^2 - 1}, \tag{4.23}$$

where $\tilde{z} = \frac{z}{z_r}$ is the position of the gas target for perfect phase matching in units of the Rayleigh range. Notably, Eq. 4.23 may have two solutions. However, we just consider the solution with the smaller modulus of $\tilde{z}$, since the intensity for large

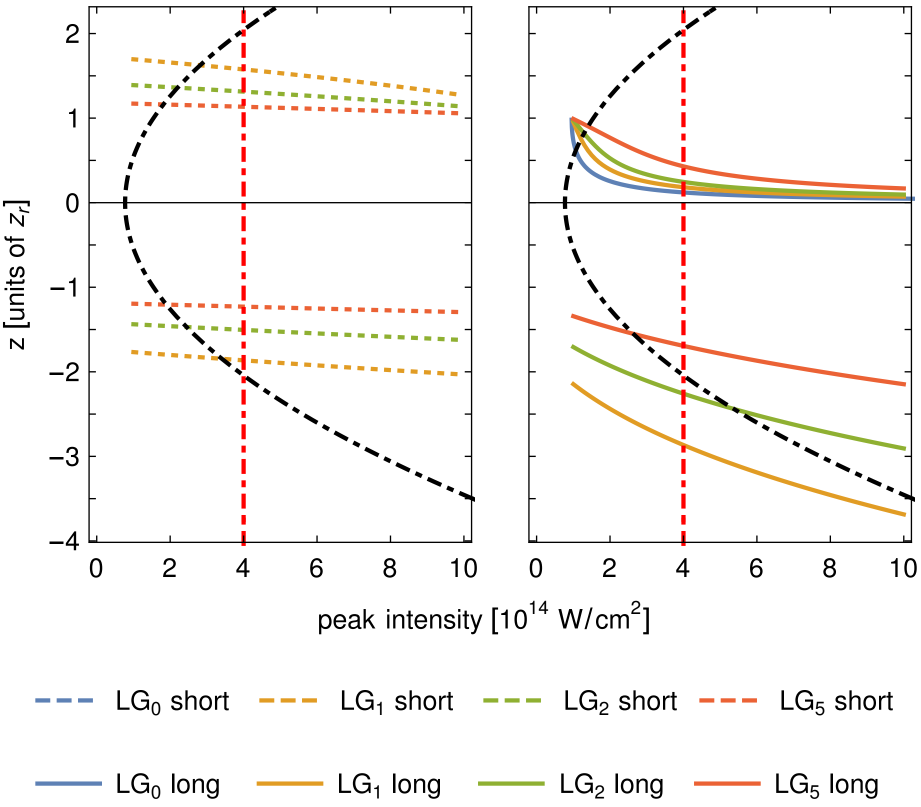

Figure 4.11: Positions for perfect phase matching along the propagation axis for a gas target depending on the peak intensity at the focus. The black, dot-dashed line denotes the transition between the cutoff and plateau region for the 21st harmonic. The vertical red, dot-dashed line helps to guide the eyes to compare the results with the Fig. 4.10. The results are calculated by means of Eq. 4.21.

values of $\tilde{z}$ is generally to low to efficiently generate harmonics.

Moreover, Eq. 4.23 requires a minimal peak intensity of $I_0 > \frac{q}{\alpha_{s,l}}$ to have real solutions, which means that below this minimal peak intensity a position for perfect phase matching does not exist. Since the α-coefficient for the short trajectories is much smaller than for the long trajectories, a much high peak intensity is required to have perfect phase matching for the short trajectories. For the example of a 21st harmonic a peak intensity of approximately $15 \cdot 10^{14}$ W/cm² is required for perfect phase matching of the short trajectories. These intensities are inapplicable for most of the rare gas atoms[5], since they will be completely ionized after a few cycles at these intensities. For the long trajectories, however, this minimal intensity is in the order of 10^{14} W/cm² which is applicable also to rare gas atoms.

---

[5] Helium with $I_p = 24.6\,\text{eV}$ is an exception.

Similarly, the positions for perfect phase matching on maximum for LG beams are solutions to

$$-\frac{|\ell|}{2}\tilde{z}^4+\tilde{z}^2-2\frac{\alpha_{s,l}I_0}{q}\tilde{z}+1+\frac{|\ell|}{2}=0, \tag{4.24}$$

which have to be calculated numerically. However, we can still see the behavior of the solutions for several limiting cases:

- For higher OAM of the incident beam, the optimal position for the gas target approaches the Rayleigh range.
- For the long trajectories, with large α coefficients, the solution to Eq. 4.24 near the focus plane can be approximated by $2\frac{\alpha_{s,l}I_0}{q}\tilde{z}-1-\frac{|\ell|}{2}=0$, which indicates that the position for perfect phase matching approaches the focus for higher intensities.

In Fig. 4.11, we show how the position for perfect phase matching changes with the peak intensity of the beam, again for the example of the 21^{st} harmonic. The black, dot-dashed line marks the transition between the plateau and the cutoff region for the 21^{st} harmonic. In particular, "left" from the black dot-dashed line, the intensity is not high enough so that the 21^{st} harmonic belongs to the plateau. The vertical red, dot-dashed line helps to guide the eye for the position for perfect phase matching at a peak intensity of $4\cdot 10^{14}\,\mathrm{W/cm^2}$. The intersection points for the curves for the position of perfect phase matching with the red line are the stationary points of Fig. 4.9 and the positions with the highest coherence length in Fig. 4.10, respectively.

In order to understand Fig. 4.11, let us discuss how different phase contributions to the total phase depend on the peak intensity. The contribution of the dipole phase to the total phase increases if the peak intensity increases. It contributes positively before and negatively behind the focus. In contrast, the Gouy phase and the focal phase are independent of the peak intensity. Furthermore, the contribution of the Gouy phase to the longitudinal wave vector mismatch is always positive, the focal phase contributes negatively.

For Gaussian beams, perfect phase matching is achieved if the sum of the derivatives of Gouy and dipole phase cancel each other. Both derivatives are positive before the focus and thus condition for perfect phase matching cannot be fulfilled before the focus. Since the sign of the slope of the dipole phase changes behind the focus it is here possible to satisfy the condition for perfect phase matching. If we increase the intensity, this position approaches the focus. Notably, there is no position for perfect phase matching for the short trajectories from the Gaussian (LG_0)

beam. As discussed before, a high peak intensity is required in order to fulfill the condition for perfect phase matching. As seen from the left part of Fig. 4.11, an intensity of $10^{15}\,\mathrm{W/cm^2}$ is not sufficient, since there is no dashed blue curve.
For LG beams, there are always two positions for perfect phase matching. If we just consider the Gouy and the focal phase, we find that these positions are given by

$$z = \pm\sqrt{1+\frac{2}{|\ell|}}\,z_{\mathrm{r}}, \tag{4.25}$$

which agrees with the position for perfect phase matching of the short trajectories for small intensities, where the contribution of the dipole phase is negligible. Generally, we observe two distinct behaviors. First, for higher OAM the position for perfect phase matching approaches the Rayleigh range. Second, for high intensities, the position for perfect phase matching behind the focus approaches the focus plane, while its moves away from the focus plane before the focus.

4.3.4 *Transverse and longitudinal phase matching*

In the previous section, where we investigated *phase matching on maximum*, we basically just considered harmonics that are emitted at the transverse intensity maximum and analyzed only longitudinal phase matching. In order to analyze phase matching off the intensity maximum, we need to take the change of the dipole and the focal phase in radial direction into account.
In Fig. 4.12, we show the coherence length of the 21st harmonic for the short (left column) and long (right column) trajectories for various LG beams with different values of OAM, similarly as it was presented in [85] for Gaussian beams. The black dashed line marks the transition from the plateau to the cutoff for a given harmonic order and the red dashed line follows the radial intensity maximum. We calculated the wave vector mismatch from Eq. 4.12 and used the coherence length as defined in Eq. 4.13.
For the short trajectories, we see that the coherence length across the focus decreases as the OAM increases. This is due to the large Gouy phase shift across the focus. However, as already discussed for the one dimensional model, we can see that especially for the long trajectories that the large phase shift due to the Gouy phase can be compensated by the dipole phase. In particular, this gives rise to areas with a coherence length larger than 1 mm shortly behind the focus. If we follow the line of the intensity maximum, we see that these figures for Gaussian beams are in good agreement with the results from phase matching on the maximum from

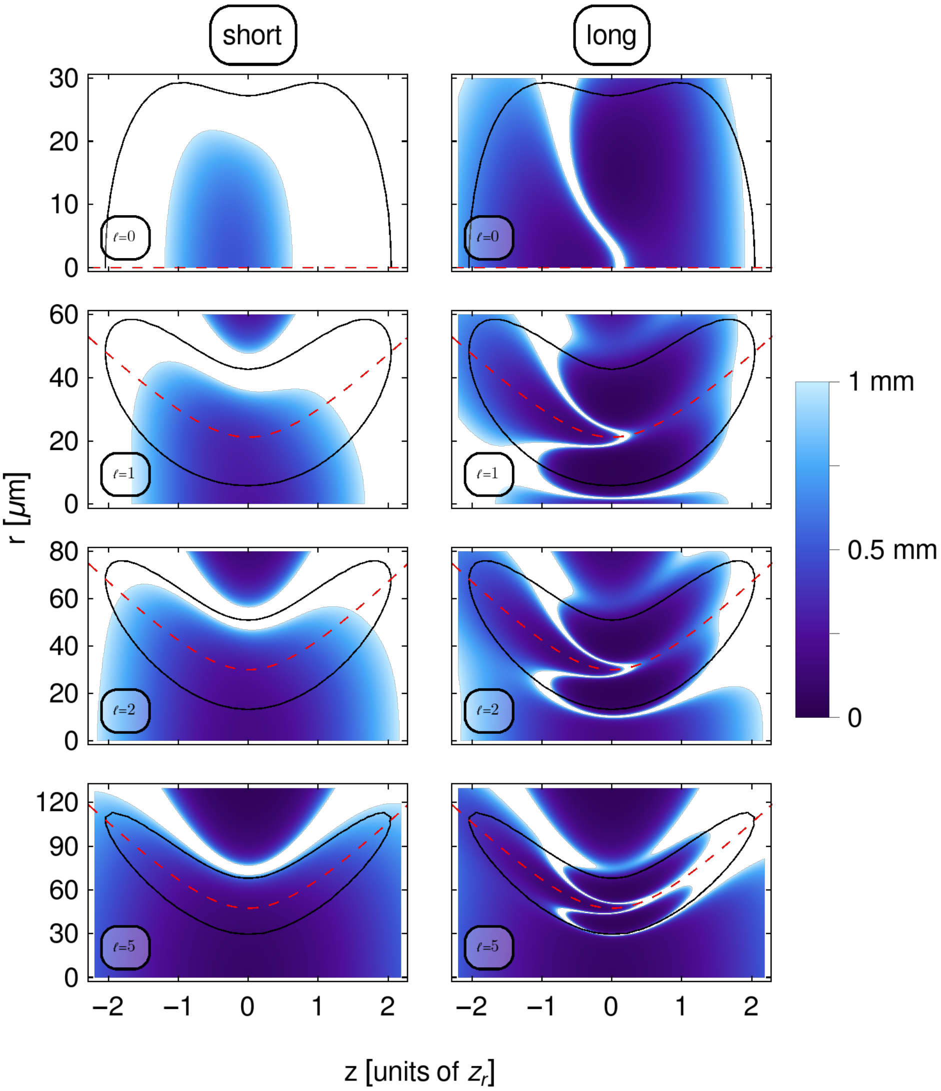

Figure 4.12: Maps of the coherence length for the 21st harmonic in and perpendicular to the propagation direction of the beam. The results are shown for a Gaussian ($LG_{0,0}$), for a $LG_{1,0}$, for a $LG_{2,0}$ and for a $LG_{5,0}$ beam (from top to bottom). The left panel presents results for the short while the right panel presents results for the long trajectories. The coherence length has been calculated from Eq. 4.13. The peak intensity at the focus $z = 0$ is $4 \cdot 10^{14}\,\mathrm{W/cm^2}$, the Rayleigh range is $z_r = 3.5\,\mathrm{mm}$ and the beam waist is $30\,\mu\mathrm{m}$. The black line marks the cutoff intensity for each beam. Inside the black line, the harmonic contributes to the harmonic plateau. The red line marks the transverse intensity maximum.

the previous subsection. For LG beams the agreement is worse than for Gaussian beams, since the change of the intrinsic phase in radial direction is cannot be considered in the one dimensional model.

In Fig. 4.13, we display the same phase matching maps as Fig. 4.12 but for the 35th harmonic. This harmonic can be created in a much smaller active volume compared to the 21st harmonic owing to the increase of the cutoff intensity with the

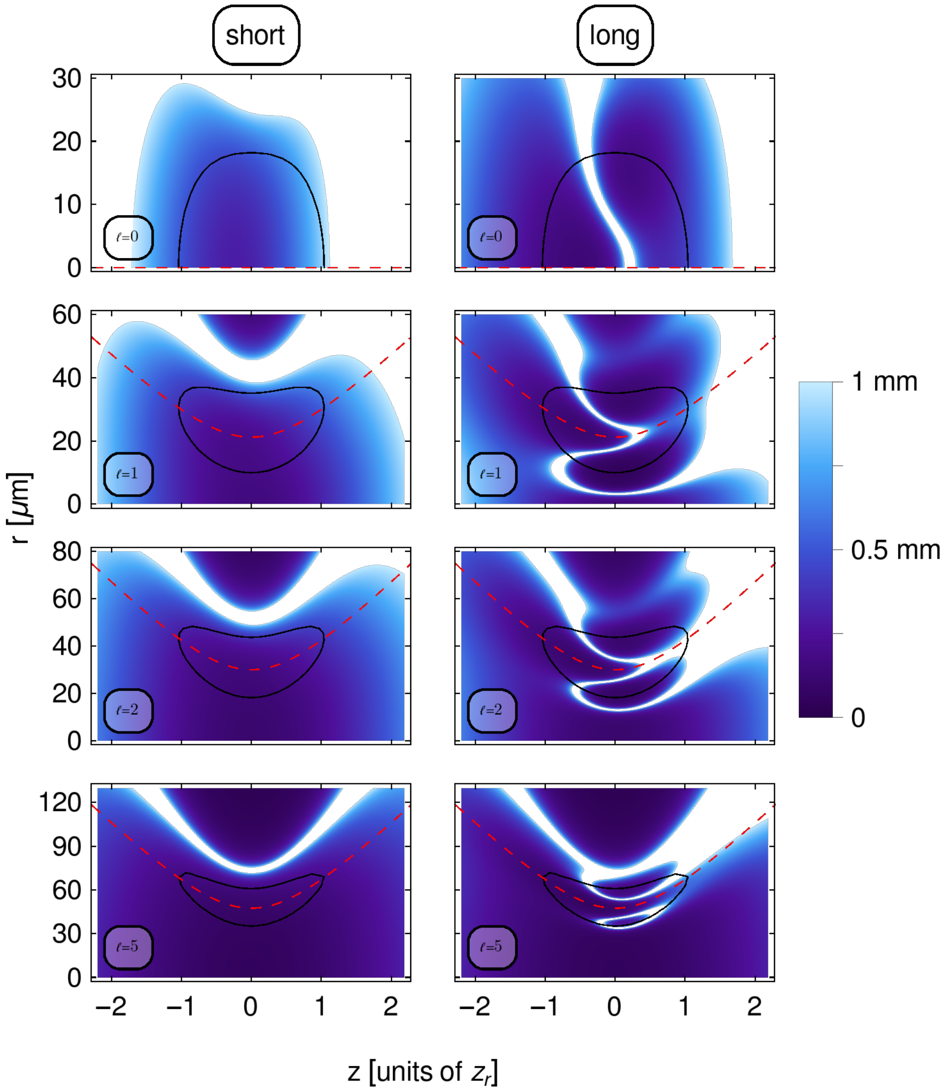

Figure 4.13: Same as Fig. 4.12, but for the 35th harmonic.

harmonic order. For our calculations of the dipole phase of the 35th harmonic we used $\alpha_s = 2.5 \cdot 10^{-14}\,\mathrm{cm}^2/\mathrm{W}$ and $\alpha_l = 21.5 \cdot 10^{-14}\,\mathrm{cm}^2/\mathrm{W}$, which have been obtained from quantum orbit calculations.

Similar to Fig. 4.12, the coherence length for the short trajectory decreases in the driving volume with the OAM. However, again we find areas in the interaction region with high coherence length behind the focus for the long trajectories.

Let us compare the coherence length for the long trajectory contributions to the 35th harmonic from Fig. 4.13 with those to the 21st harmonic of Fig. 4.12. We see that for both harmonic orders, there are regions with coherence length larger than 1 mm behind the focus. However, for the 21st harmonic the most favorable conditions occur for $\ell = 5$, while for the 35th they arise for $\ell = 2$. This indicates that there is an optimal OAM for the long trajectory contributions for each harmonic order,

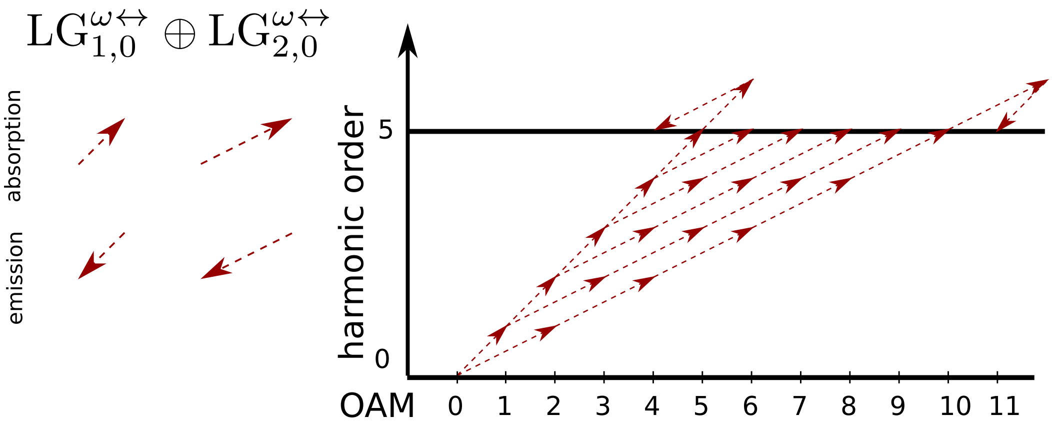
$\mathrm{LG}_{1,0}^{\omega\leftrightarrow} \oplus \mathrm{LG}_{2,0}^{\omega\leftrightarrow}$
absorption
emission
harmonic order
5
0
OAM
0 1 2 3 4 5 6 7 8 9 10 11

Figure 4.14: HHG with a superposition of two linearly polarized LG beams with the same photon energy but different OAM as proposed in [86]. The photon diagrams for the fifth harmonic show that there are multiple pathways to generate this harmonic.

which may help in particular to study and identify long trajectory contributions to HHG and may be even extended to beams with higher wavelengths in the infrared regime.

4.4 CONTROLLING THE OAM OF HARMONICS BY MULTI-MODE HHG

So far, we investigated HHG with only a single linearly polarized LG beam and for example showed that the OAM of the generated harmonics increases with the harmonic order. However, the OAM of the generated harmonics, in these cases, is only controllable in a very limited manner. In this section we will present three possible scenarios of HHG with linearly polarized LG beams that show how the OAM of the harmonics can be further manipulated and controlled [86–88]. The basic idea of these three scenarios is the superposition of two linearly polarized LG modes, so called *mode mixing*.

In the first scenario, we consider a superposition of two linearly polarized LG beams with the same frequency but different OAM. In the original work by Rego *et al.* [86] they used a

$$\mathrm{LG}_{1,0}^{\omega\leftrightarrow} \oplus \mathrm{LG}_{2,0}^{\omega\leftrightarrow}.$$

superposition, where both beams have a wavelength of 800 nm. Generally, an electron has to absorb q photons to contribute to the generation of a q harmonic. Since both beams have the same frequency, respectively photon energy, there are multiple photon pathways that contribute to a q^{th} harmonic. More precisely, if the electron

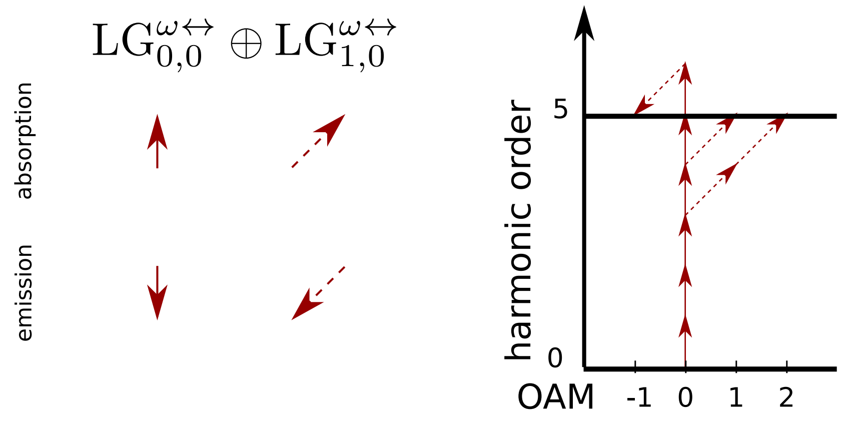
$\mathrm{LG}^{\omega\leftrightarrow}_{0,0} \oplus \mathrm{LG}^{\omega\leftrightarrow}_{1,0}$
absorption
emission
harmonic order
5
0
OAM
-1
0
1
2

Figure 4.15: HHG with a non-collinear superposition of a strong Gaussian beam with a weaker LG beam. The photon diagrams for the fifth harmonic show that there are multiple pathways to generate this harmonic. The harmonics are spatially separated at the detector according to their OAM due to the non-collinear setup.

absorbs n photons from the $\mathrm{LG}^{\omega\leftrightarrow}_{1,0}$ beam it has to absorb $q - n$ photons from the $\mathrm{LG}^{\omega\leftrightarrow}_{2,0}$ beam, to generate a q^{th} harmonic. This gives rise to $q + 1$ different photon pathways for a q^{th} harmonic. We illustrate some of the possible pathways for the simple example of a fifth harmonic in Fig. 4.14.

However, HHG is a non-perturbative process, which means that the q^{th} harmonic can be also generated, for example, by the absorption of more than q photons from the $\mathrm{LG}^{\omega\leftrightarrow}_{1,0}$ beam and subsequent emission of photons from the $\mathrm{LG}^{\omega\leftrightarrow}_{2,0}$ beam. Such an example is also shown in Fig. 4.14, where the fifth harmonic can also carry an OAM of four. By means of the photon picture, this can be achieved if the electron absorbs six photons from the $\mathrm{LG}^{\omega\leftrightarrow}_{1,0}$ beam and emits one $\mathrm{LG}^{\omega\leftrightarrow}_{2,0}$ photon. In particular, it shows that the generation of a fifth harmonic can also be a seventh order process and shows the non-perturbative picture of HHG. Similarly, if the electron absorbs six photons with $\ell = 2$ and emits one photon with $\ell = 1$, the fifth harmonic carries an OAM of $\ell_{H_5} = 11$.

This argumentation can be easily extended to higher photon orders (9^{th}, 11^{th}). However, the probability for the HHG along pathways of higher photon orders decreases with the number of photons that are involved in the generation. A cutoff law has been derived in [86].

In the first scenario, all generated harmonics carry multiple values of OAM. This becomes apparent at the detector, where each harmonic is a superposition of several LG modes with different OAM. Kong *et al.* developed a scenario to spatially separate the generated harmonics with respect to their OAM at the detector [87]. They used a non-collinear geometry of the two driving beams, which means that the beams are superimposed under a small angle of $\sim 1° - 2°$. In the original work,

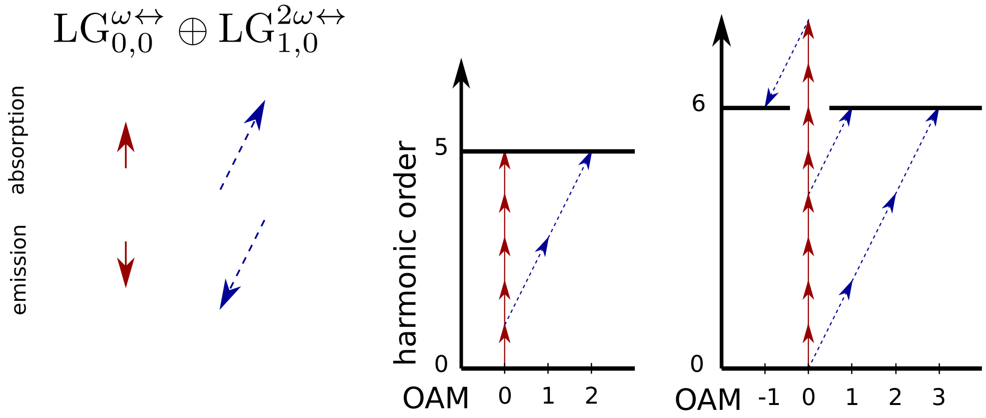
$\mathrm{LG}_{0,0}^{\omega\leftrightarrow} \oplus \mathrm{LG}_{1,0}^{2\omega\leftrightarrow}$
absorption
emission
harmonic order
5
0
OAM
0
1
2
6
0
OAM
-1
0
1
2
3

Figure 4.16: HHG with a non-collinear superposition of a strong Gaussian with its second harmonic that carries a well defined OAM. Similar to Fig. 4.15 we get spatially separated XUV-vortices that carry a well defined OAM as well. In addition, within this superposition it is also possible to generate even harmonic orders

they considered the non-collinear superposition of a strong Gaussian beam with a weaker LG beam, where both beams have the same frequency:

$$\mathrm{LG}_{0,0}^{\omega\leftrightarrow} \oplus \mathrm{LG}_{1,0}^{\omega\leftrightarrow}.$$

The intensity ratio of the two beams was approximately $100 : 1$. In Fig. 4.15, we show some possible pathways for the example of a fifth harmonic. Since the $\mathrm{LG}_{0,0}^{\omega\leftrightarrow}$ beam is more intense than the $\mathrm{LG}_{1,0}^{\omega\leftrightarrow}$, it is more likely for the electron to absorb photons from the Gaussian beam. Nevertheless, the electron can absorb photons from the weaker LG beam, then the generated harmonics carry OAM. The harmonics are spatially separated at the detector with respect to their OAM due to conservation of linear momentum. It gives rise to XUV radiation into direction of $\mathbf{k_q} = n_1\mathbf{k}_1 + n_2\mathbf{k}_2$, where $\mathbf{k}_1$ $(\mathbf{k}_2)$ and n_1 (n_2) are the wave vectors and the number of absorbed photons from the $\mathrm{LG}_{0,0}^{\omega\leftrightarrow}$ ($\mathrm{LG}_{1,0}^{\omega\leftrightarrow}$) driving beam. Since their wave vectors are not parallel to each other, harmonics generated by different combinations of photons from the two driving beams will be spatially separated.

In a last scenario, we discuss the non-collinear superposition of a strong Gaussian with a weaker LG mode that has two times the frequency of the Gaussian beam

$$\mathrm{LG}_{0,0}^{\omega\leftrightarrow} \oplus \mathrm{LG}_{1,0}^{2\omega\leftrightarrow},$$

which was proposed by Gauthier *et al.* [88]. In their experiment they used an intensity ratio of approximately $5 : 1$. The left photon diagram of Fig. 4.16 shows two possible photon pathways for the fifth harmonic. Since the frequency of the second beam is twice the frequency of the first beam a fifth harmonic does not necessarily require that five photons are absorbed. The left path shows the absorption of five photons with frequency ω and the right one the absorption of one photon with frequency ω and two photons with frequency 2ω. Both of these pathways lead to different OAM in the fifth harmonic. Similarly to the previously discussed scenario, the harmonics are spatially separated at the detector. Notably, the absorption of three photons from the $\mathrm{LG}_{0,0}^{\omega \leftrightarrow}$ beam and one photon from the $\mathrm{LG}_{1,0}^{2\omega\leftrightarrow}$ photons does not contribute to the fifth harmonic, since the total number of involved photons has to be an odd number. In contrast to the first two scenarios, this superposition of beams gives rise to a sixth harmonic as well, which is shown in the right photon diagram of Fig. 4.16.

5

HIGH-HARMONIC GENERATION WITH BICIRCULAR LAGUERRE-GAUSSIAN BEAMS

In this chapter, we discuss the HHG of atomic targets in bicircular LG beams. We will first introduce these bicircular fields and analyze them with respect to their symmetry. Then, similarly to the previous chapter we discuss the single atom response to these bicircular fields. Afterwards we analyze the HHG by macroscopic targets and explain the conservation of OAM. Finally, we will consider the temporal evolution of the high-harmonic signal and how it is affected by the OAM of the driving beam.

Some of the material in this chapter has appeared previously in references

> *Tailored orbital angular momentum in high-order harmonic generation with bicircular Laguerre-Gaussian beams*
> Paufler, W., Böning, B., Fritzsche, S.
> *PHYSICAL REVIEW A*, **98**, 011401(R) (2018)
>
> *High harmonic generation with Laguerre–Gaussian beams*
> Paufler, W., Böning, B., Fritzsche, S.
> *Journal of Optics*, **21**(9), 094001 (2019)

5.1 HIGH-HARMONIC GENERATION IN CIRCULARLY POLARIZED FIELDS

HHG is a versatile tool to explore atomic structure on the ultra fast time scale. If high harmonics are generated by linearly polarized driving beams, the generated harmonics also exhibit linear polarization, c.f. Ch. 4. Similarly, one may expect to generate circularly polarized harmonics with circularly polarized driving beams. However, HHG in circularly polarized beams is strongly suppressed.

We can explain this suppression by means of semi-classical physics. From a semi-classical viewpoint, the HHG arises from the recombination of the released electron with the parent ion after the electron was accelerated by the driving laser field. In circularly polarized laser fields, however, the electron, which moves on its classical trajectory, will not come back to the parent ion. Therefore HHG is strongly suppressed in circularly polarized fields.

Moreover, we can understand this suppression in terms of the conservation of SAM.

Each photon has SAM of either plus or minus one that corresponds to its polarization. In a circularly polarized beam all photons have the same SAM. If an electron absorbs more than one photon from a circularly polarized beam, their SAM add up. However, the SAM of the emitted photons can only be plus or minus one as well. Therefore it is not possible to emit high harmonic radiation after the absorption of several photons, where all photons have the same SAM.

However, the availability of circularly polarized harmonics becomes important to probe for example chiral matter [89]. Luckily it is possible to manipulate the driving field in such a way that circularly polarized harmonics can be generated. For example, it is possible to use a non-collinear setup of two counter-rotating circularly polarized beams with the same frequency to generate circularly polarized harmonics [18]. Another way is the use of so-called bicircular driving beams.

5.2 BICIRCULAR MODES

5.2.1 *Composition of bicircular modes*

As a bicircular beam we will denote a superposition of a circularly polarized beam with its counter-rotating second harmonic. In the literature there are different denotations for these fields. Some papers use *two color counter-rotating circularly polarized* fields [90, 91], while others use *bichromatic circularly polarized fields* [92]. However, we will refer to *bicircular fields*, similarly to [93, 94]. Although it is possible to consider a general superposition of two counter-rotating circularly polarized beams with frequencies $r\omega$ and $s\omega$, where r and s are arbitrary integers, we will always refer to the $\omega - 2\omega$ superposition unless stated otherwise.

In Fig. 5.1, we show how the electric field of a bicircular beam arises from two counter-rotating circularly polarized beams. Here both beams have the same intensity, respectively magnitude of the electric field. The effect of the intensity ratio between the two counter-rotating beams to the electric field is illustrated in Fig. 5.2.

5.2.2 *Symmetries in bicircular LG modes*

These bicircular fields have rotational symmetry that is of special interest, especially when we consider HHG with twisted bicircular fields. But let us start with a plane wave bicircular field. We can express the electric field of the bicircular beam as

$$\mathbf{E}(\varphi_1, \varphi_2, t) = \mathbf{E}^{\omega\ \circlearrowleft}(\varphi_1, t) + \mathbf{E}^{2\omega\ \circlearrowright}(\varphi_2, t), \tag{5.1}$$

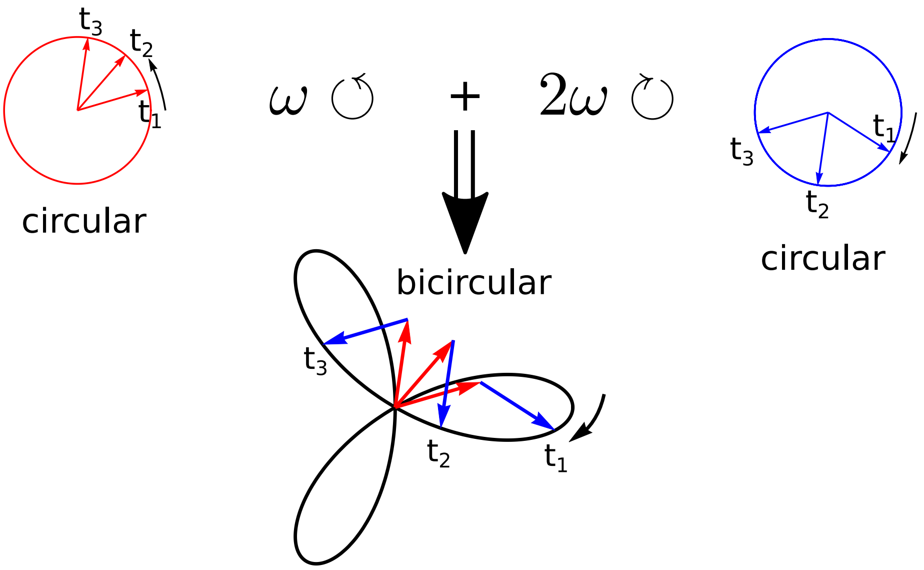

Figure 5.1: The composition of a bicircular field out of a superposition of a circularly polarized field with its counter-rotating second harmonic. For circularly polarized fields the electric field vector rotates in the $E_x - E_y$-plane, as shown top left and top right. For bicircular fields we add the electric field vectors, as shown for t_1, t_2 and t_3, which results in this Lissajous figure or *bicircular trefoil* for the electric field.

where the left and right circularly polarized components are given by

$$\mathbf{E}^{\omega\circlearrowleft}(\varphi_1, t) = \frac{E_\omega}{\sqrt{2}} \left(\cos\left(\varphi_1 - \omega t\right) \mathbf{e}_x - \sin\left(\varphi_1 - \omega t\right) \mathbf{e}_y\right) \tag{5.2}$$

and

$$\mathbf{E}^{2\omega\circlearrowright}(\varphi_2, t) = \frac{E_{2\omega}}{\sqrt{2}} \left(\cos\left(\varphi_2 - 2\omega t\right) \mathbf{e}_x + \sin\left(\varphi_2 - 2\omega t\right) \mathbf{e}_y\right), \tag{5.3}$$

respectively. Here E_ω and $E_{2\omega}$ are the field amplitudes. So far, the variables φ_1 and φ_2 are two phase terms without explicit physical meaning, but we will attach some to them in terms of twisted beams later in this section. If we set both phase terms to zero, the electric field has the shape of the Lissajous figure as shown in Fig. 5.3a. The black dot shows where the electric field vector will point to at $t = 0$. The color scale indicates the evolution of the electric field with time. If we set $\varphi_1 = \frac{\pi}{2}$, the Lissajous figure is rotated through an angle of $\theta_1 = -\frac{2}{3}\varphi_1$ around the z-axis [95, 96], as shown in Fig. 5.3b. Notably, it rotates clockwise. In contrast, if we set $\varphi_2 = \frac{\pi}{2}$, the Lissajous figure is rotated counter-clockwise through an angle of $\theta_2 = \frac{1}{3}\varphi_2$, which we show in Fig. 5.3c.

Interestingly, for both changes of φ_i the vector of the electric field will be shifted

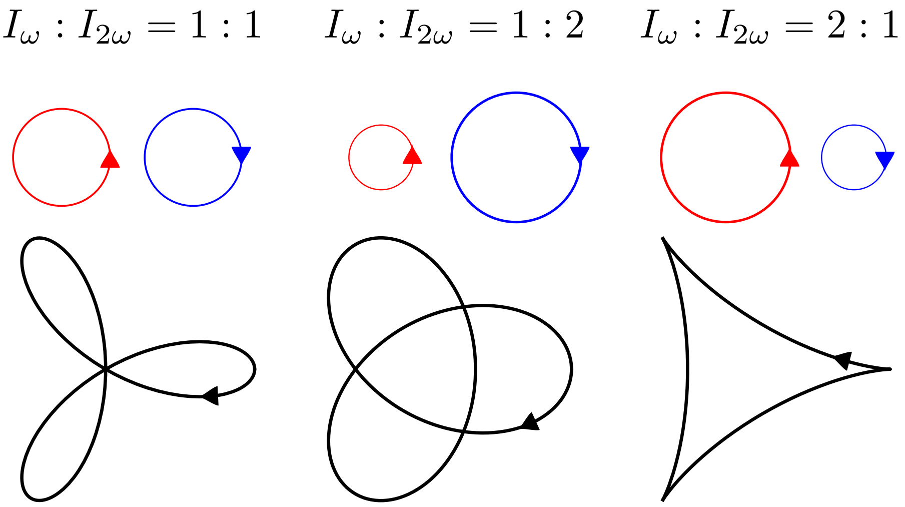
$I_\omega : I_{2\omega} = 1 : 1$
$I_\omega : I_{2\omega} = 1 : 2$
$I_\omega : I_{2\omega} = 2 : 1$

Figure 5.2: Visualization of the electric field of bicircular fields for various intensity ratios of the circularly polarized incident beams in the $E_x - E_y$-plane.

in time such as $t' = t - \frac{\varphi_i}{3\omega}$, which can be seen by the shift of the black dot. We can express the electric field in Eq. 5.1 for arbitrary phases φ_1 and φ_2 as

$$\mathbf{E}(\varphi_1, \varphi_2, t) = \mathbf{R}\left(\frac{\varphi_2 - 2\varphi_1}{3}\right) \mathbf{E}\left(0, 0, t - \frac{\varphi_1 + \varphi_2}{3\omega}\right), \tag{5.4}$$

where the rotation matrix is given by

$$\mathbf{R}(\varphi) = \begin{pmatrix} \cos(\varphi) & -\sin(\varphi) \\ \sin(\varphi) & \cos(\varphi) \end{pmatrix}. \tag{5.5}$$

Let us now apply these findings to LG beams. We can express bicircular LG beams as a superposition of two LG beams with frequencies ω and 2ω and opposing polarization:

$$\mathbf{LG}(\varphi, t) = \mathbf{LG}^{\omega\ \circlearrowleft}_{\ell_1, p_1}(\varphi, t) + \mathbf{LG}^{2\omega\ \circlearrowright}_{\ell_2, p_2}(\varphi, t). \tag{5.6}$$

The circularly polarized LG beams can be expressed as

$$\mathbf{LG}^{\omega\ \circlearrowleft}_{\ell_1, p_1}(\varphi, t) = \frac{E_\omega(\rho, z)}{\sqrt{2}} \left(\cos\left(\ell_1 \varphi - \omega t\right) \mathbf{e}_x - \sin\left(\ell_1 \varphi - \omega t\right) \mathbf{e}_y\right) \tag{5.7}$$

and

$$\mathbf{LG}^{2\omega\ \circlearrowright}_{\ell_2, p_2}(\varphi, t) = \frac{E_{2\omega}(\rho, z)}{\sqrt{2}} \left(\cos\left(\ell_2 \varphi - \omega t\right) \mathbf{e}_x + \sin\left(\ell_2 \varphi - \omega t\right) \mathbf{e}_y\right). \tag{5.8}$$

Here we hide the exact shape of the spatial dependent amplitudes, which have

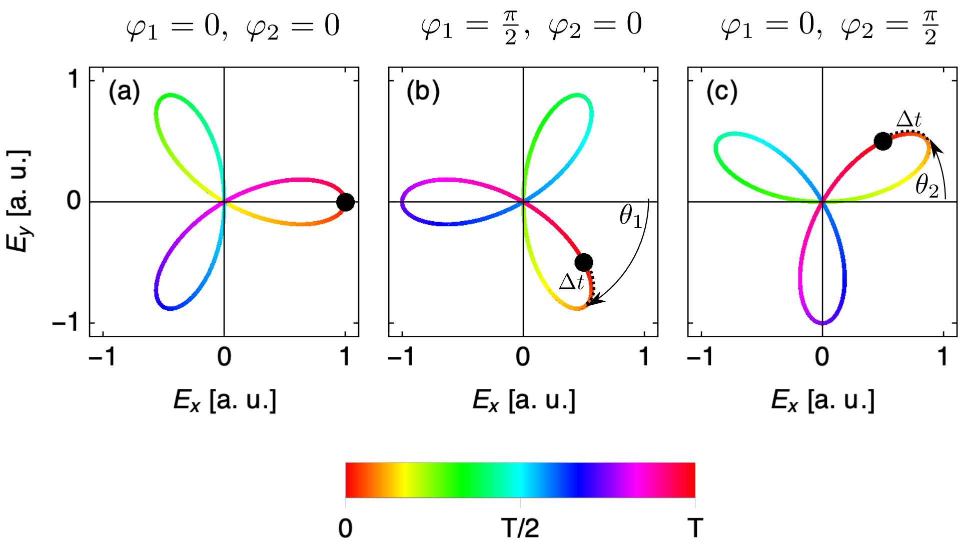

Figure 5.3: Visualization of the electric field of bicircular fields for depending on the phase terms in Eq. 5.4 in the $E_x - E_y$-plane. Left: $\varphi_1 = \varphi_2 = 0$, the Lissajous figure shows up as presented before. Middle: $\varphi_1 = \pi/2$ and $\varphi_2 = 0$, the Lissajous figure rotates through $\pi/3$ and the electric field is shifted in time as $t' = t - \frac{\varphi_i}{3\omega}$. Right: $\varphi_1 = 0$ and $\varphi_2 = \pi/2$, the Lissajous figure rotates through $\pi/6$ opposed to the case in the middle figure and the electric field is shifted again in time as $t' = t - \frac{\varphi_i}{3\omega}$.

been presented in Eq. 2.14, in $E_\omega(\rho, z)$ and $E_{2\omega}(\rho, z)$.

Interestingly, Eq. 5.7 and Eq. 5.8 have a similar structure to Eq. 5.2 and Eq. 5.3, respectively. However, there are important differences. First, for LG beams, the amplitude is spatially dependent. Second, the initially introduced phase terms φ_1 and φ_2 have a physical meaning as they are rewritten as $\ell_1\varphi$ and $\ell_2\varphi$, where ℓ_1 and ℓ_2 denote the OAM of the LG beams and φ is the azimuthal coordinate.

Now, Eq. 5.4 helps to understand how the Lissajous figure at different azimuthal angles has to be transformed compared to $\varphi = 0$. If we change the azimuthal coordinate from $\varphi = 0$ to $\varphi = \varphi_0$, the Lissajous figure will rotate through an angle of $\frac{\ell_2 - 2\ell_1}{3}\varphi_0$. In addition, the electric field will be shifted in time such as $t' = t - \frac{\ell_1 + \ell_2}{3\omega}\varphi_0$, as shown in Fig. 5.4. We can rewrite the local electric field of a bicircular LG beam as

$$\mathbf{LG}(\varphi, t) = \mathbf{R}\,(\gamma\varphi)\,\mathbf{LG}(0, t - \tau\varphi), \tag{5.9}$$

where

$$\gamma = \frac{\ell_2 - 2\ell_1}{3} \tag{5.10}$$

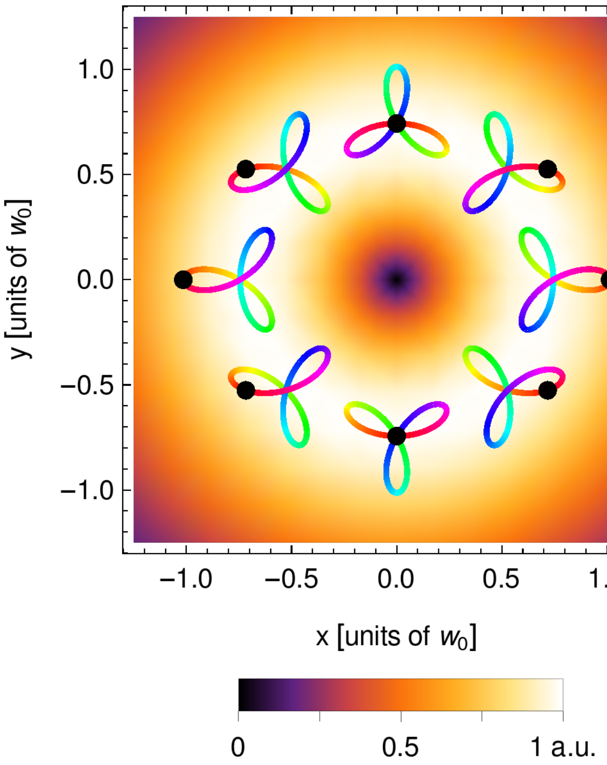

Figure 5.4: Orientation of the Lissajous figures for various azimuthal angles φ in a bicircular LG beam ($\mathrm{LG}^{\omega\,\circlearrowleft}_{1,0} + \mathrm{LG}^{2\omega\,\circlearrowright}_{1,0}$). The background shows the the cycle averaged intensity distribution of the two superimposed LG beams with the characteristic singularity in on the beam axis. For $\varphi = 0$ the Lissajous figure has the same orientation as in Fig. 5.3a. The black dot helps to guide eyes and shows the position of the electric field vector at $t = 0$.

is the OAM dependent rotational and

$$\tau = \frac{\ell 1 + \ell_2}{3\omega} \tag{5.11}$$

is the OAM dependent time delay parameter [97]. We will need these symmetries to understand the temporal evolution of the harmonic radiation, which is considered in Sec. 5.6.

5.3 SINGLE ATOM RESPONSE TO A BICIRCULAR FIELD

Let us now discuss the harmonic response of a single atom to a bicircular laser field. HHG with these bicircular fields has been proposed already a few years ago by Milošević [98] and experimentally confirmed by Fleischer *et al.* [99].
The characteristic spectrum of emitted harmonics in bicircular fields, as shown in Fig. 5.5, has fundamental differences to the spectrum of HHG in linearly polarized

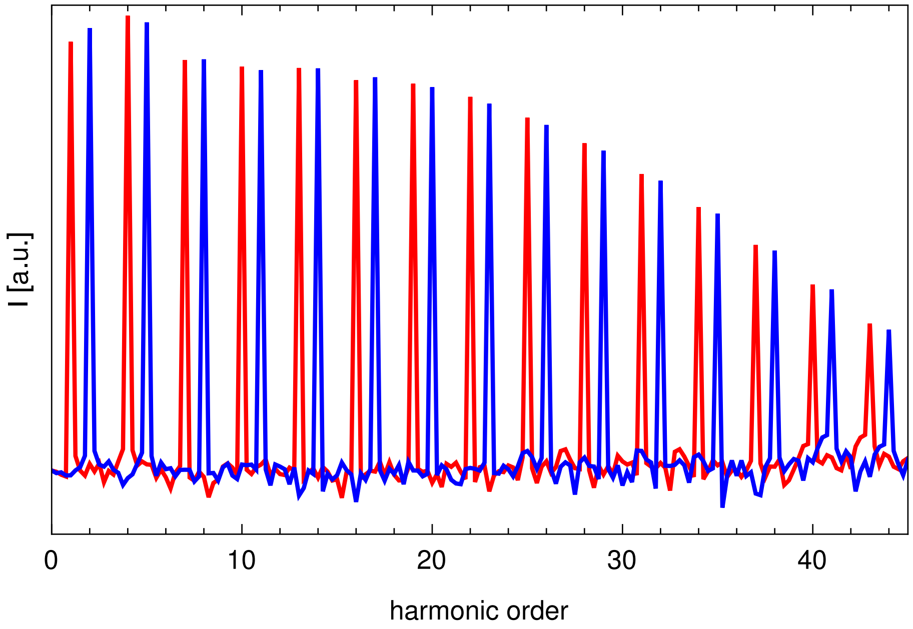

Figure 5.5: Characteristic spectrum of high harmonics generated by a bicircular ($\omega - 2\omega$) field with equal intensities of 10^{14} W/cm² in an arbitrary logarithmic scale. The spectrum exhibits the characteristic plateau of several harmonics that are emitted at similar intensities and the subsequent exponential harmonic cutoff around the 21^{st} harmonic. Different colors indicate different polarization of the generated harmonics. The calculation has been performed with the RB-SFA code [70].

fields. Here, every third harmonic is suppressed and the contributing harmonics exhibit alternatingly left and right circular polarization. The $3n+1$ harmonics (red) have the same polarization as the fundamental ω driver, while the $3n+2$ harmonics (blue) exhibit the same polarization as the 2ω beam.

Similarly to HHG with linearly polarized beams, the plateau, which is followed by an exponential cutoff in the harmonic intensity, is characteristic for the harmonic spectrum. However, the cutoff for HHG in bicircular fields, with equal intensities of the two circularly polarized components, is given by [98]

$$n_{\max}\omega = \frac{1}{\sqrt{2}} 3.17 U_p + 1.2 I_p, \tag{5.12}$$

where the ponderomotive potential is defined by $U_p = \frac{E_\omega^2}{4\omega^2} + \frac{E_{2\omega}^2}{16\omega^2}$. We can explain HHG with bicircular beams in terms of intuitive photon diagrams [100] as shown in Fig. 5.6. Within this picture of photon diagrams

- photons from the fundamental, red, left circularly polarized, ω beam have a SAM of plus one,

- photons from the second harmonic, blue, right circularly polarized, 2ω beam have a SAM of minus one.

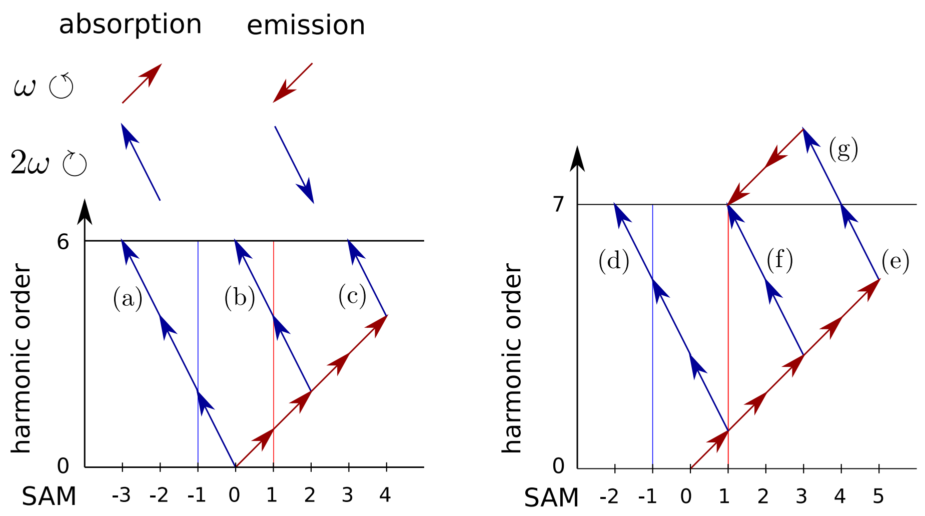

Figure 5.6: Candidates for photon pathways to generate a sixth (left) or seventh (right) harmonic. Photons from the ω-beam with SAM of one are indicated by red arrows, while those of the 2ω-beam with SAM minus one are denoted by blue arrows. The SAM of the harmonic is shown on the x-axis. (a), (b), (c), (d) and (e) are forbidden since the SAM of the generated harmonics has to be plus of minus one. (f) and (g) as an extension of (e) contribute to the generation of a seventh harmonic. Furthermore (g) shows the non-perturbative nature of HHG.

In the left part of Fig. 5.6, we show possible candidates (a-c) for photon pathways that could contribute to a sixth harmonic. However, none of these shown pathways for the sixth harmonic ends up at a projection of the SAM of plus (vertical red line) or minus one (vertical blue line). For example, the absorption of three 2ω-photons (blue) leads to a SAM of minus three, thus HHG is forbidden from this pathway. Moreover, since there is no combination of blue and red photons, which corresponds to the sixth harmonic and ends up at SAM plus or minus one, this harmonic is strongly suppressed in the spectrum. This also agrees with Fig. 5.5.
In the right part of Fig. 5.6, we show pathways for the seventh harmonic. Here, the photon paths (d) and (e) do not contribute to HHG. However, pathway (f) ends up at SAM plus one after the absorption of three red and two blue photons, which results into the emission of a left circularly polarized seventh harmonic. In addition, pathway (g), which is an extension to pathway (e) also contributes to the generation of the seventh harmonic. Notably, pathway (g) is similar to (f) and just differs by the additional absorption and emission of two red photons. Briefly speaking, the net absorption of photons for pathway (f), three red and two blue photons, and pathway (g), $5-2=3$ red and two blue photons, is the same. However, pathway

(g) is a pathway of higher photon order. These higher order pathways are allowed and have significant contributions to HHG, since it is a non-perturbative process. For simplicity, we will treat both paths as the same. Generally, we will refer to net absorption of photons if we speak about absorption.
It can be easily seen from the photon diagrams that only paths where the number of net absorbed red and blue photons differs by one can contribute to HHG. This simple rule gives rise to the selection rules for HHG in bicircular fields:

$$\mathrm{LG}_{0,0}^{\omega\,\circlearrowleft} \oplus \mathrm{LG}_{0,0}^{2\omega\,\circlearrowright} \quad \xrightarrow{\text{HHG}} \quad \begin{aligned} \omega_{H_q} &= q\,\omega = m\omega + n2\omega, \\ m - n &= \pm 1, \end{aligned} \tag{5.13}$$

where m is the number of absorbed red and n the number of absorbed blue photons.

5.4 EXTENDED TARGETS IN BICIRCULAR LG BEAMS

In the previous section, we discussed HHG with bicircular plane waves, respectively the single atom response to a bicircular field. However, in order to investigate HHG with bicircular LG beams, we have to take the coherent nature of HHG into account. The measured harmonic radiation at the detector is a result of the superposition of all single atom responses in the interaction region of the driving laser. The results in this section were calculated by means of the Fraunhofer diffraction model, which we presented in Eq. 3.45.

5.4.1 *Conservation of SAM and OAM*

In Fig. 5.7 we show the calculated far field phase profiles for the 11th and 13th harmonic. We used a bicircular LG driving field that can be expressed as

$$\mathrm{LG}_{1,0}^{\omega\,\circlearrowleft} \oplus \mathrm{LG}_{1,0}^{2\omega\,\circlearrowright}, \tag{5.14}$$

or to put it in other word, both LG beams have the same OAM $\ell = 1$. For our simulations, we choose that both beams have a waist of 30 μm and a peak intensity of 10^{14} W/cm² at the focus. The far-field phase profiles for the 11th harmonic reveals seven phase shifts of 2π along the azimuth, which implies that the 11th harmonic carries an OAM of $\ell_{H_{11}} = 7$. This is also confirmed by the computation of the azimuthal Fourier transform (bottom left). Similarly, the 13th harmonic carries an OAM of $\ell_{H_{11}} = 9$.

At first glance, this result seems to be unexpected, since it does not reveal the linear scaling of the OAM with the harmonic order as it does for linearly polarized LG beams. In Sec. 5.3, we showed there is only one photon path for each harmonic in these bicircular fields. Locally each atom is irradiated by a bicircular field. Therefore the photon pathway that contributes to a given harmonic order is well defined. For example, in order to generate an 11th harmonic, the electron has to absorb three red and four blue photons, since $3\omega + 4 \cdot 2\omega = 11\omega$. Within the paraxial approximation SAM and OAM are well separated quantities, thus both of them have to be conserved simultaneously [101]. The polarization of the 11th harmonic has to be the same as the polarization of the $\mathrm{LG}_{1,0}^{2\omega\circlearrowright}$, due to the conservation of SAM. For the conservation of OAM we need to consider the OAM of all absorbed photons. Since both beams carry an OAM of $\ell = 1$, the OAM of the 11th harmonic can be computed as $\ell_{H_{11}} = 3 \cdot 1 + 4 \cdot 1 = 7$. Analogously, we get for the 13th harmonic that $\ell_{H_{13}} = 9$. We can summarize the simultaneous conservation of SAM and OAM with the following selection rules [102]:

$$\mathrm{LG}_{\ell_1,0}^{\omega\circlearrowleft} \oplus \mathrm{LG}_{\ell_2,0}^{2\omega\circlearrowright} \quad \xrightarrow{\mathrm{HHG}} \quad \begin{array}{rcl} \omega_{H_q} & = & q\,\omega = m\omega + n2\omega, \\ m - n & = & \pm 1, \\ \ell_{H_q} & = & m\ell_1 + n\ell_2, \end{array} \tag{5.15}$$

where again m is the number of absorbed red and n the number of absorbed blue photons. Note that the upper two equations are the same as for bicircular plane wave fields, while the last equation accounts for the conservation of OAM. The latter one also implies that the OAM of the harmonics can be manipulated by the OAM of the incident beams.

Similarly to HHG linearly polarized LG beams, we can write the amplitude of the q^{th} harmonic in the near-field as

$$A_q^{(\mathrm{near})}(\rho', \varphi') = f(\rho') e^{i\ell_{H_q}\varphi'}. \tag{5.16}$$

This is a more general expression than that in Eq. 4.5, since the OAM of the q^{th} harmonic is not necessarily $q\ell$. However, we can evaluate the azimuthal integral in Eq. 3.45 analogously, which gives

$$A_q^{(\mathrm{far})}(\beta, \varphi) = 2\pi i^{\ell_{H_q}} e^{i\ell_{H_q}\varphi} \int_0^\infty d\rho' \rho' f(\rho') J_{\ell_{H_q}}\left(\frac{2\pi}{\lambda_q}\beta\rho'\right), \tag{5.17}$$

where again λ_q is the wavelength of the q^{th} harmonic and $J_k(x)$ is a Bessel function of the first kind. From Eq. 5.17, we can see that the divergence of the harmonics

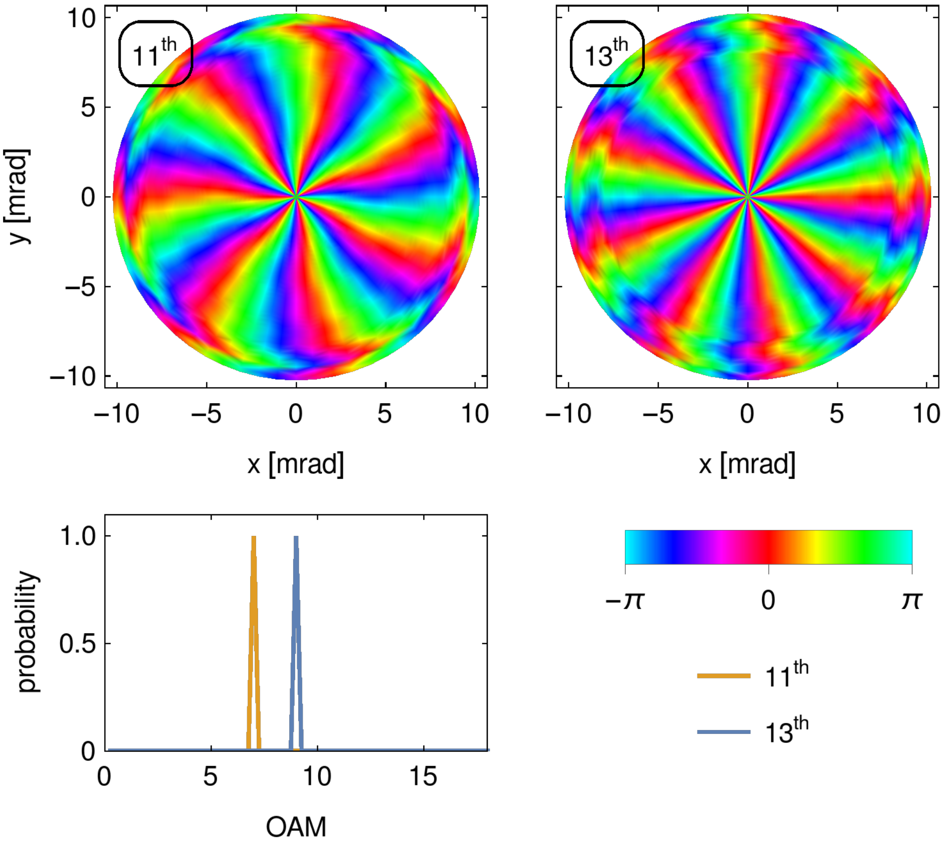

Figure 5.7: Top: The phase profiles for the 11th and 13th harmonic at the detector generated by a bicircular LG beam, $\mathrm{LG}_{1,0}^{\omega\circlearrowleft} \oplus \mathrm{LG}_{1,0}^{2\omega\circlearrowright}$. The OAM (number of phase shifts of 2π) for the 11th harmonic is equal to seven, while for the 13th harmonic it is equal to nine. Bottom left: OAM of the 11th (blue) and 13th (red) harmonic calculated by a Fourier transform along the azimuthal coordinate.

increases with the OAM but decreases with the harmonic order. Since we can manipulate the OAM of the harmonics by the OAM of the incident beam, it is possible to to manipulate the divergence as well [66, 100].

In particular, the divergence for the 11th and 13th harmonic are quite similar to each other, as shown in Fig. 5.8. In Fig. 5.9 we present photon diagrams for HHG with bicircular LG beams. Notably, we only selected these pathways that contribute to HHG, respectively these pathways where the number of red and blue photons differs by one. In contrast to these diagrams in Fig. 5.6, where we focused on the SAM, we now focus on the OAM of the emitted harmonics (x-axis). We show the photon pathways by way of example for the fifth and seventh harmonic for two different superposition of LG beams. In the left part, we use the superposition

$$\mathrm{LG}_{1,0}^{\omega\circlearrowleft} \oplus \mathrm{LG}_{1,0}^{2\omega\circlearrowright}, \tag{5.18}$$

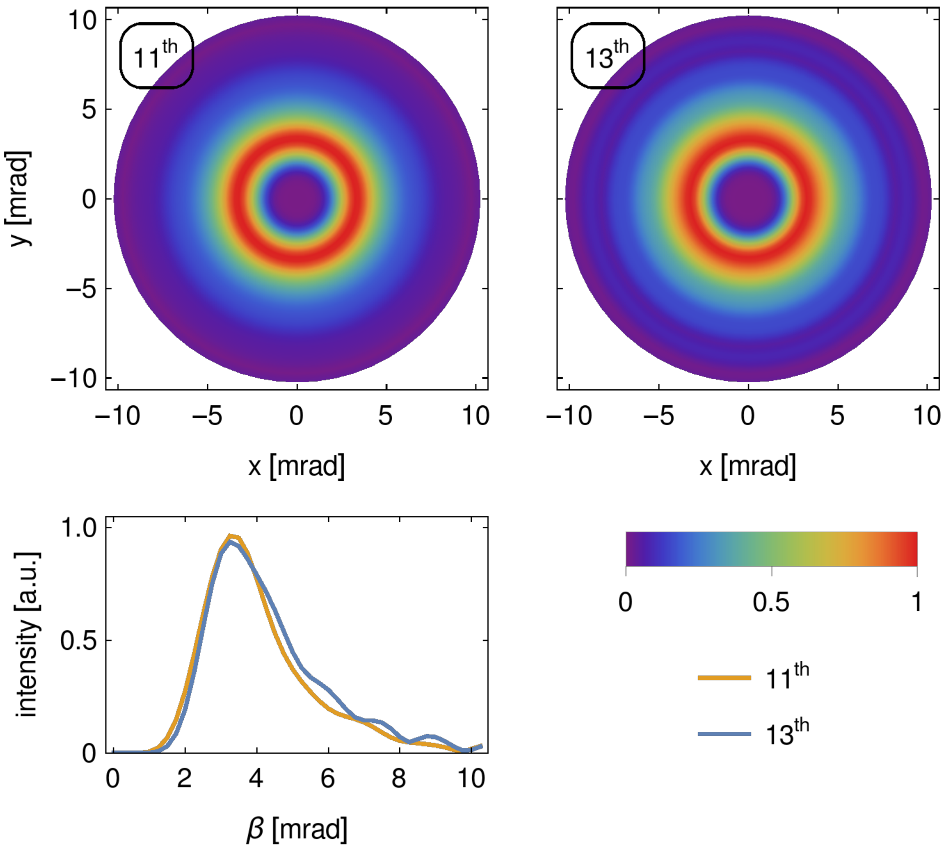

Figure 5.8: Top: The intensity profiles for the 11^{th} and 13^{th} harmonic at the detector generated by a bicircular LG beam, $\mathrm{LG}_{1,0}^{\omega\circlearrowleft} \oplus \mathrm{LG}_{1,0}^{2\omega\circlearrowright}$. Bottom left: Cut through the intensity profiles of the 11^{th} and 13^{th} harmonic. The maximum of the intensity profiles is set to one.

which we also considered for the calculations of Fig. 5.7 and Fig. 5.8. In the right part, we consider the superposition

$$\mathrm{LG}_{1,0}^{\omega\circlearrowleft} \oplus \mathrm{LG}_{-1,0}^{2\omega\circlearrowright}. \tag{5.19}$$

In particular, the latter superposition is interesting, since all generated harmonics will carry the same modulus of OAM. More precisely all left circularly polarized harmonics carry an OAM of $\ell = 1$, while all right circularly polarized harmonics carry an OAM of $\ell = -1$. From the Fraunhofer diffraction formula, we can deduce that the divergence will decrease with the harmonic order if harmonics are generated by this superposition of LG beams.

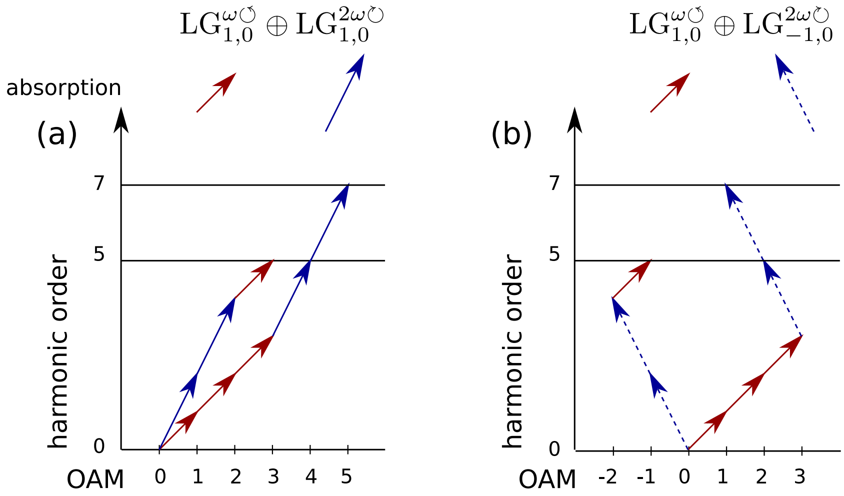
$\mathrm{LG}^{\omega\circlearrowright}_{1,0} \oplus \mathrm{LG}^{2\omega\circlearrowright}_{1,0}$
$\mathrm{LG}^{\omega\circlearrowright}_{1,0} \oplus \mathrm{LG}^{2\omega\circlearrowright}_{-1,0}$
absorption
(a)
(b)
harmonic order
7
5
0
OAM
0 1 2 3 4 5
-2 -1 0 1 2 3

Figure 5.9: Photon diagrams for the generation of a 5th and 7th harmonic by (a) $\mathrm{LG}^{\omega\circlearrowright}_{1,0} \oplus \mathrm{LG}^{2\omega\circlearrowright}_{1,0}$ and (b) $\mathrm{LG}^{\omega\circlearrowright}_{1,0} \oplus \mathrm{LG}^{2\omega\circlearrowright}_{-1,0}$ superpositions. Different arrows denote absorption of photons from different beams. Here we just show photon pathways that contribute to the generation of harmonics. On the x-axis we can read of the OAM of the generated harmonics.

5.4.2 *Tailored OAM*

In Sec. 5.4.1, we found selection rules for HHG in bicircular LG beams, c.f. Eq. 5.15. These selection rules show that the OAM of the harmonics depends on the OAM of the incident LG beams. It is possible to control the OAM the the harmonics precisely by the incident beams. Moreover, for a given harmonic order q, it is always possible to find values for the OAM ℓ_1 and ℓ_2, such that the OAM takes the value ℓ_{H_q}. In order to prove this, we will analyze the selection rules in more detail. For a q^{th} harmonic, we can find the number of absorbed red photons by

$$m = \frac{q \pm 2}{3} \tag{5.20}$$

and the number of absorbed blue photons by

$$n = \frac{q \mp 1}{3}. \tag{5.21}$$

Notably, for each harmonic order, these equations have two solutions. However, only one of them is integer valued. The other solution can be discarded, since fractional photons do not exist. For example, for an 11^{th} harmonic order, we get

$$m = \frac{11 \pm 2}{3} \quad \text{and} \quad n = \frac{11 \mp 1}{3}.$$

Here $m = 3$ and $n = 4$ are the significant solutions. Moreover, for harmonic orders that are divisible by three, we cannot find integer solutions. This is in agreement with the suppression of every third harmonic in bicircular driving fields..

Once we have determined the number number of red (m) and blue (n) photons that have to be absorbed to generate a q^{th} harmonic, we are still left to verify that we can always find integer values for ℓ_1 and ℓ_2, such that

$$\ell_{H_q} = m\ell_1 + n\ell_2. \tag{5.22}$$

Noteworthy, Eq. 5.22 is a linear Diophantine equation [103]. These equations are solvable if and only if ℓ_{H_q} is divisible by the greatest common divisor of m and n. However, m and n differ exactly by one, due to the conservation of SAM. This implies that their greatest common divisor must be equal to one. Therefore the condition to find solutions is always fulfilled.

Let us now construct the set of solutions for ℓ_1 and ℓ_2. First, we solve the homogeneous part of Eq. 5.22. As a second step, we find one particular solution. Finally, we can express the set of solutions as a superposition of the homogeneous and particular solution. The homogeneous equation is given by

$$0 = m\ell_1 + n\ell_2. \tag{5.23}$$

This equation is fulfilled for

$$\ell_1 = a \cdot n \tag{5.24}$$

$$\ell_2 = -a \cdot m, \tag{5.25}$$

where a is an arbitrary integer. We are now left to find a particular solution. Here we have to distinguish between two cases.

1. $\mathbf{m - n = 1}$

   Here the q^{th} harmonic has the same polarization as the incident $\mathrm{LG}^{\omega\,\circlearrowleft}_{\ell_1,0}$ beam. The particular solution is given by

   $$\ell_1 = \ell_{H_q} \qquad \text{and} \qquad \ell_2 = -\ell_{H_q}, \tag{5.26}$$

   which can be easily verified by means of Eq. 5.22. Finally, we can write the set of solutions as

   $$\ell_1 = \ell_{H_q} + a \cdot n \qquad \text{and} \qquad \ell_2 = -\ell_{H_q} - a \cdot m \tag{5.27}$$

with an arbitrary integer a.

2. $\mathbf{m - n = -1}$

   Here the q^{th} harmonic has the same polarization as the incident $\text{LG}_{\ell_2,0}^{2\omega\circlearrowright}$ beam. The particular solution is given by

   $$\ell_1 = -\ell_{H_q} \qquad \text{and} \qquad \ell_2 = \ell_{H_q}. \tag{5.28}$$

   Similarly we express the set of solutions as

   $$\ell_1 = -\ell_{H_q} + a \cdot n \qquad \text{and} \qquad \ell_2 = \ell_{H_q} - a \cdot m. \tag{5.29}$$

   Again a is an arbitrary integer.

Notably, there are infinitely many solutions for each set (ℓ_1, ℓ_2). However, commonly for experimental applications small values for the OAM are chosen, since beams with small OAM are much easier to generate than those with large OAM.

5.4.3 *Generalization to* $r\omega + s\omega$

So far, we just considered $\omega - 2\omega$ bicircular fields. However, this analysis can be generalized to $r\omega - s\omega$ bicircular fields. We illustrate the electric field for $r\omega - s\omega$ bicircular fields for various values of r and s in Fig. 5.10.

Of course, the harmonics that contribute to the spectrum change according to the frequencies that compose the bicircular field. We can adapt the photon diagrams that we developed for $\omega - 2\omega$ bicircular fields to find the contributing harmonics for general bicircular driving fields. For example, a $\omega - 3\omega$ gives rise to only odd harmonics, while a $2\omega - 3\omega$ suppresses all harmonics, except of all $(5n \pm 2)$ harmonics. However, even for general $r\omega - s\omega$ bicircular fields, it is always possible to tailor the OAM of each harmonic in a precise manner as described in Sec. 5.4.2.

In Tab. 5.1 we present the parameters for the incident beams to generate a q^{th} harmonic with tailored OAM ℓ_{H_q}.

5.5 GENERATION OF NEAR-CIRCULARLY POLARIZED ATTOSECOND PULSE TRAINS

In the previous sections our main focus was to find which harmonic orders are generated and how we can control individual harmonics with respect to their polarization (SAM) and their OAM. However, in experiments usually several harmonics are superimposed and form an attosecond pulse [104] or pulse train [105]. HHG with

FREQUENCIES	HARMONIC ORDER	OAM	m	n	SAM	ℓ_1	ℓ_2
$\omega + 2\omega$	$q = m + 2n$	ℓ_{H_q}	$\frac{q \pm 2}{3}$	$\frac{q \mp 1}{3}$	$m - n = +1$	$\ell_{H_q} + a\,n$	$-\ell_{H_q} - a\,m$
	$q = 1, 2, 4, 5, \ldots$				$m - n = -1$	$-\ell_{H_q} + a\,n$	$\ell_{H_q} - a\,m$
$\omega + 3\omega$	$m + 3n$	ℓ_{H_q}	$\frac{q \pm 3}{4}$	$\frac{q \mp 1}{4}$	$m - n = +1$	$\ell_{H_q} + a\,n$	$-\ell_{H_q} - a\,m$
	$q = 1, 3, 5, 7, \ldots$				$m - n = -1$	$-l_{H_q} + a\,n$	$l_{H_q} - a\,m$
$r\omega + s\omega$	$rm + sn$	ℓ_{H_q}	$\frac{q \pm s}{r + s}$	$\frac{q \mp r}{r + s}$	$m - n = +1$	$\ell_{H_q} + a\,n$	$-\ell_{H_q} - a\,m$
	$q = r,\ s,\ 2r + s,\ 2s + r,\ 3r + 2s,\ 3s + 2r, \ldots$				$m - n = -1$	$-\ell_{H_q} + a\,n$	$\ell_{H_q} - a\,m$

Table 5.1: Parameters of the incident bicircular LG beams to generate high-harmonics with selected OAM ℓ_{H_q}. Apart from the frequency ratio of the counter-rotating beams (first column), we show the harmonic order and the OAM of the emitted harmonic (second and third column). In the forth and fifth column, we calculated m and n, respectively the number of photons from the first and second incident beam which are necessary to obtain the q^{th} harmonic. The column labeled with SAM gives the SAM of the q^{th} harmonic, where we assumed the first driving beam to carry SAM of one and the second driving beam SAM of minus one, respectively. The last two columns can be used to determine the required OAM of the incident beams in order to generate the q^{th} harmonic with an OAM of ℓ_{H_q}. Here a is an arbitrary integer.

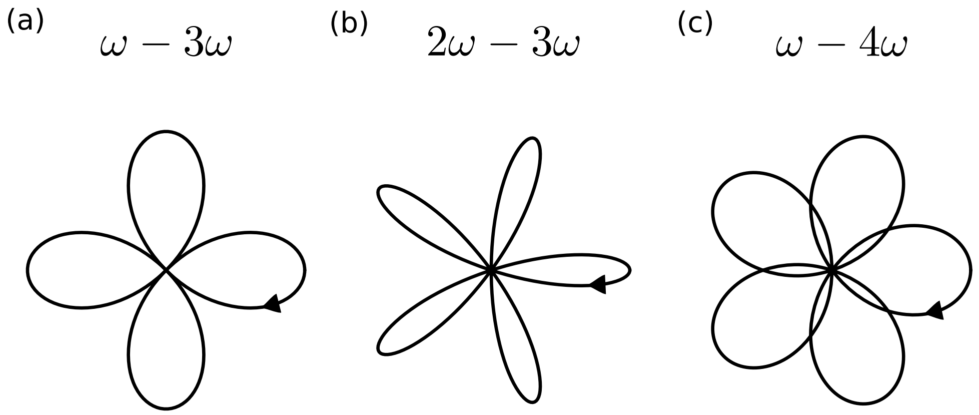

Figure 5.10: Visualization of the electric field of general $r\omega - s\omega$ bicircular fields for various intensity values of r and s in the $E_x - E_y$ -plane.

linearly polarized beams generates linearly polarized harmonics and thus linearly polarized attosecond pulses. As we showed, HHG with bicircular beams generates alternatingly left and right circularly polarized harmonics. However, the resulting attosecond pulses are still linearly polarized, since neighboring harmonics exhibit different polarization. Here, three linearly polarized attosecond pulses, each rotated by 120°, are emitted per cycle, as illustrated in Fig. 5.13a. In this section we will discuss two ways to manipulate the polarization of the generated attosecond pulses.

5.5.1 *Spatial separation with* OAM

We discussed the possibilities to tailor the OAM of the harmonics precisely by the OAM of the driving beams. Since the divergence of the harmonics is affected by the OAM, the divergence of the harmonics can be controlled similarly.

In Fig. 5.11, we show the intensity distributions for several harmonics from the plateau ($10^{\text{th}} - 17^{\text{th}}$). Here we compare three different superpositions of LG beams:

(a) $\text{LG}_{1,0}^{\omega\,\circlearrowleft} \oplus \text{LG}_{1,0}^{2\omega\,\circlearrowright}$,

(b) $\text{LG}_{1,0}^{\omega\,\circlearrowleft} \oplus \text{LG}_{-1,0}^{2\omega\,\circlearrowright}$,

(c) $\text{LG}_{2,0}^{\omega\,\circlearrowleft} \oplus \text{LG}_{-1,0}^{2\omega\,\circlearrowright}$,

where in our simulations each driving beam has a peak intensity of $10^{14}\,\text{W/cm}^2$.

In Fig. 5.11a, we display that the harmonics generated by superposition (a) are emitted at similar divergence. This is the same superposition, which we used in Fig. 5.7.

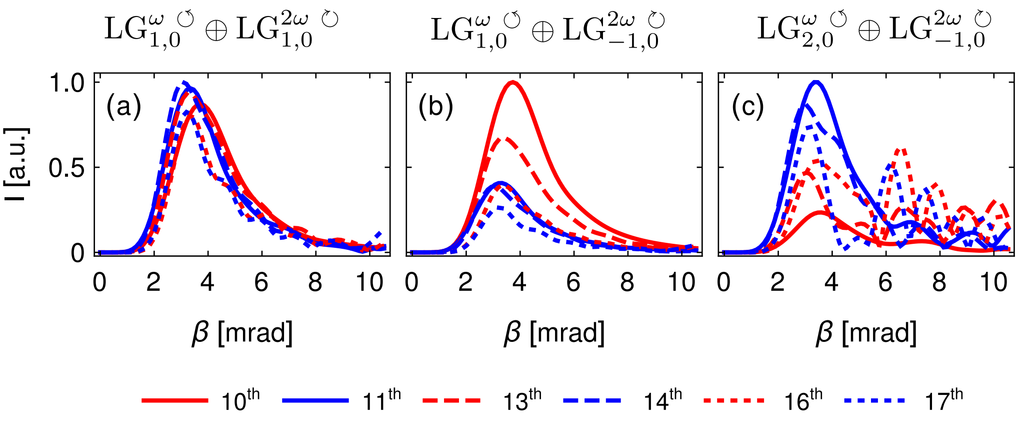

Figure 5.11: Intensity distributions of generated harmonics for three different incident bicircular LG beams. Different colors indicate different polarization of the emitted harmonics. The intensity distributions show that the divergence of the harmonics can be controlled by the OAM of the driving beam. (a) All harmonics, left (red) and right (blue) circularly polarized harmonics, are emitted with similar divergence. (b) The divergence decreases as the harmonic order increases, since all harmonics have the same modulus of OAM. (c) Left and right circularly polarized harmonics can be spatially separated at the detector, by proper choosing of the OAM of the incident beams [66].

As indicated earlier in Fig. 5.9b, all harmonics generated by superposition (b) carry the same modulus of OAM. This implies that divergence decreases for each harmonic order, as shown in Fig. 5.11b.

In Fig. 5.11c, we show that left (red) and right (blue) circularly polarized harmonics have a significantly different divergence if they are generated by superposition (c). This leads to a spatial separation of left and right circularly polarized harmonics at the detector. As a result, we obtain right circularly polarized twisted attosecond pulse trains for low angles of divergence, around $\beta \approx 1\,\mathrm{mrad}$, and left circularly polarized twisted attosecond pulse trains for $\beta \approx 2.5\,\mathrm{mrad}$. This has been theoretically predicted and experimentally confirmed by Dorney *et al.* [66].

5.5.2 *Relative intensity ratio and polarization control*

Until the present, the relative intensity ratio between the two circularly polarized driving components in bicircular beams has been utilized as an easily accessible parameter in theory and experiments in order to control various strong-field processes with plane-wave beams. These include, for example, above threshold ionization [106], non-sequential double ionization [91, 107] and also HHG [108, 109]. For HHG, in particular, it was shown that it is possible to enhance the generation either

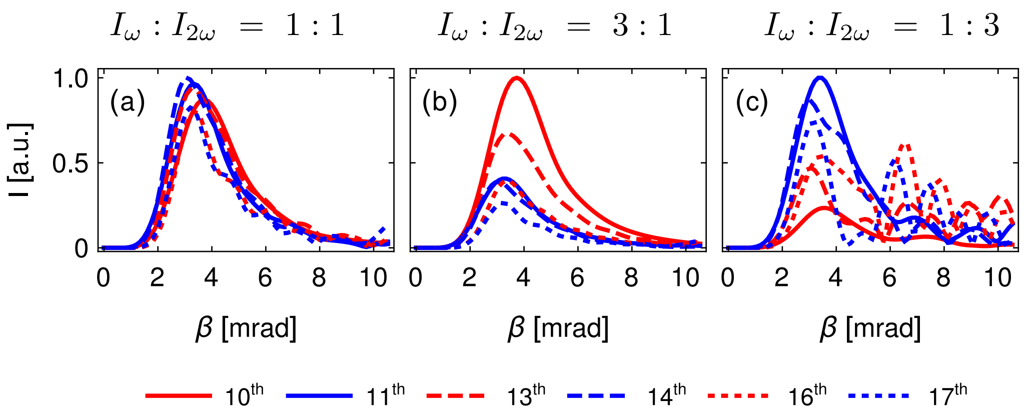

Figure 5.12: Intensity distributions of generated harmonics for three different intensity ratios of the driving beams. Different colors indicate different polarization of the emitted harmonics. For all calculations we used a $\mathrm{LG}_{1,0}^{\omega\,\circlearrowleft} \oplus \mathrm{LG}_{1,0}^{2\omega\,\circlearrowright}$ superposition. (a) Same plot as Fig. 5.11a. Intensity distribution for (b) a dominating ω-beam ($1.5 \cdot 10^{14}$ W/cm²:$0.5 \cdot 10^{14}$ W/cm²) and (c) a dominating 2ω-beam ($0.5 \cdot 10^{14}$ W/cm²:$1.5 \cdot 10^{14}$ W/cm²).

left or right circularly polarized harmonics by adjusting the relative intensity ratio of the ω and 2ω beam. The basic idea is that a suppression of all harmonics of a given polarization gives rise to the generation of circularly polarized attosecond pulses.

In this section, we show that the same scheme can be applied to bicircular LG beams. In Fig. 5.12, we displays the intensity distributions in the far-field for three different intensity ratios of the incident ω and 2ω beams in a $\mathrm{LG}_{1,0}^{\omega\,\circlearrowleft} \oplus \mathrm{LG}_{1,0}^{2\omega\,\circlearrowright}$ superposition. If both incident beams have the same intensity, as shown in Fig. 5.12a, left and right circularly polarized harmonics are emitted with similar intensities and therefore the emitted attosecond pulses will also be linearly polarized. In Fig. 5.12b the incident ω beam is dominant and, therefore, harmonics with the same polarization as the ω beam are preferably emitted. In contrast, Fig. 5.12c shows the intensity distributions when the 2ω beam dominates. Interestingly the latter case not only leads to the preferred emission of harmonics with the same polarization as the 2ω beam, but also to the formation of several maxima in the far-field intensity distribution. We would briefly remind that a $\mathrm{LG}_{\ell,0}$ beam has only one radial maximum, since its radial quantum number p equals zero. However, here the harmonics are not pure $\mathrm{LG}_{\ell,0}$ modes, but a superposition of modes with different radial quantum numbers. The appearance of higher order radial modes has already been observed in HHG with linearly polarized $\mathrm{LG}_{1,0}$ beam. Géneaux *et al.* displaced the atomic target with respect to the focus plane [110]. They explained the occurrence of additional rings to the contributions of the long trajectories [111]. These are more pronounced if the target is placed before the focus, which is also in agreement with our calcu-

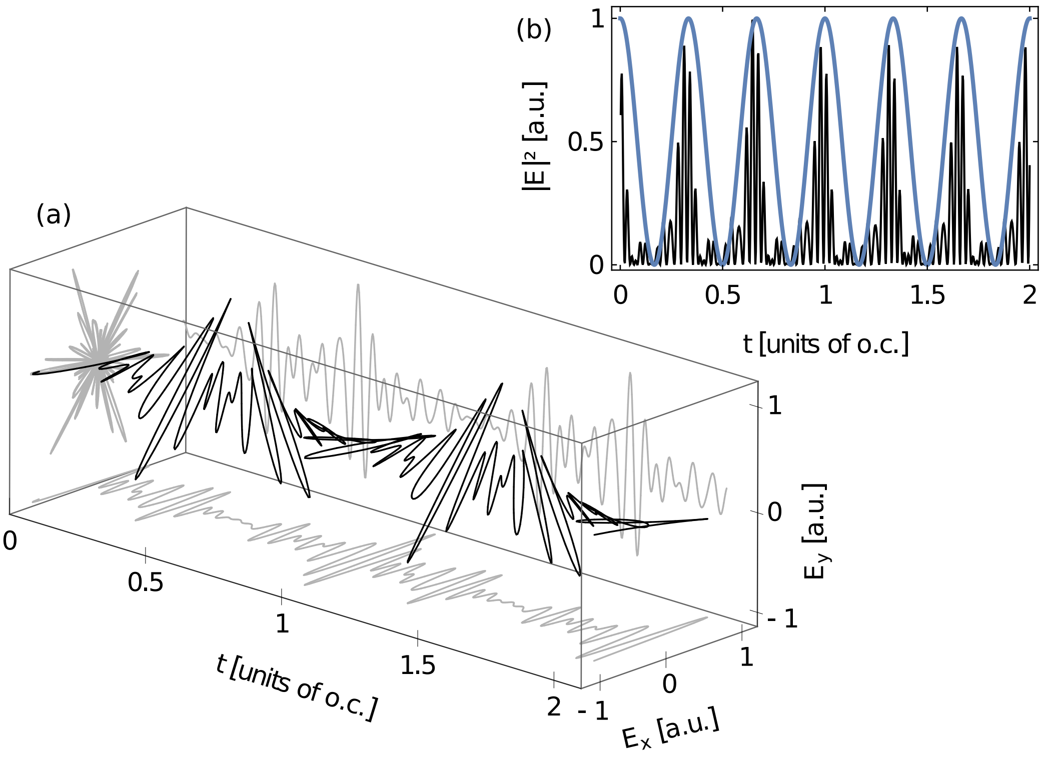

Figure 5.13: Attosecond pulse train generated with a bicircular driving beam. (a) The high harmonic signal consists of three linearly polarized attosecond pulses, each rotated by 120°, per cycle of the driving beam. (b) The envelope (blue) shows the modulus squared of the driving field, while the black curve resembles the modulus squared of the attosecond pulse, respectively the dipole acceleration. For the high-harmonic signal we only considered the harmonics from the 13^{th} to the 23^{th} order.

lations from Sec. 4.3 (c.f. Fig. 4.12 second row). A detailed analysis of the radial intensity profile in HHG with bicircular LG beams in connection with a quantum orbit analysis is still to be made in some forthcoming work [112].

5.6 ATTOSECOND LIGHT SPRINGS IN HHG

Let us now discuss the temporal evolution of the high-harmonic signal in bicircular LG beams. As stated in the previous section, HHG with bicircular beams generates three linearly polarized attosecond pulses per cycle, each rotated by 120° as shown in Fig. 5.13a. The oscillation of the electric field, which is proportional to the dipole acceleration, is maximal if the instantaneous field strength of the driving beam is maximal as well, c.f. Fig. 5.13b.

If we consider extended targets, the harmonics will be generated at different azimuthal positions in the interaction region. Due to the azimuthal phase in LG beams, the electric field is virtually shifted in time at different azimuthal positions. This

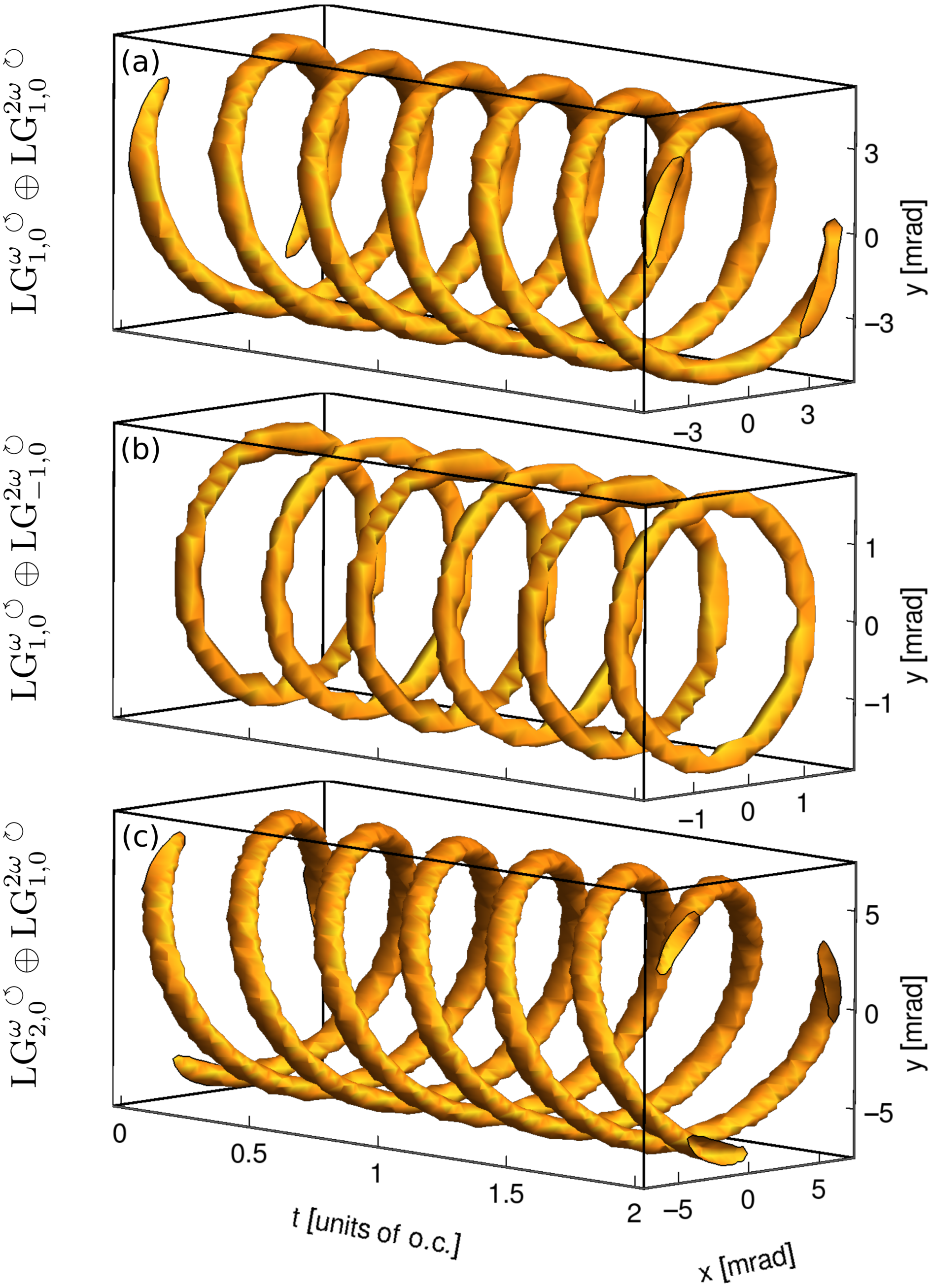

Figure 5.14: Temporal evolution of the high-harmonic signal generated by bicircular LG beams with different combinations of OAM. The three dimensional plot shows a contour at 80% of the maximum electric field of the generated signal. For the high-harmonic signal we only considered the harmonics from the 13th to the 23th order.

has been discussed when we considered the symmetry of bicircular LG earlier in Sec. 5.2.2. The azimuthal time delay implies that the attosecond pulses are generally not generated simultaneously at all azimuthal positions. Therefore the temporal evolution of the harmonic signal typically has the shape of a *light spring*. This has been initially reported by Hernández-García *et al.* [69], when they considered HHG with linearly polarized LG beams and meanwhile confirmed in different articles [88, 113].

Light springs were also reported in a different context by Pariente *et al.* [114]. Here, the authors superimposed several LG beams of different frequencies, spaced by $\delta\omega$, where the OAM of each mode was correlated to its frequency. More precisely, the OAM was increased by $\delta\ell$ as the frequency increases by $\delta\omega$. In particular, they showed that the number of coils in the light spring was affected by the ratio of $\delta\ell$ and $\delta\omega$. Thereby they showed that they can produce "first-order" and "second-order" light springs, respectively light springs with one and two coils.

In this chapter, we will consider the temporal evolution of the high harmonic signal generated by bicircular LG beams and especially how it depends on the OAM of the driving beam.

In Fig. 5.14, we show the temporal evolution of the high-harmonic signal driven by different bicircular LG beams. We used the numerical propagation of the dipole acceleration, which we introduced in Sec. 3.2.2 to calculate the signal at the detector. The three dimensional surface is a contour at 80% of the maximum intensity.

In the upper row, we show the temporal evolution of the high-harmonic signal that has been generated by a $\mathrm{LG}_{1,0}^{\omega\,\circlearrowleft} \oplus \mathrm{LG}_{1,0}^{2\omega\,\circlearrowright}$ superposition. It shows a light spring with two coils, which has also been found in HHG with a linearly polarized $\mathrm{LG}_{1,0}^{\omega\leftrightarrow}$ beam, where both driving beams have a peak intensity of $1.5 \cdot 10^{14}\,\mathrm{W/cm^2}$. Interestingly, a $\mathrm{LG}_{1,0}^{\omega\,\circlearrowleft} \oplus \mathrm{LG}_{-1,0}^{2\omega\,\circlearrowright}$ superposition does not form a light spring in the temporal evolution, c.f. Fig. 5.14b. Here we get some donut-like shape for the harmonic signal. Finally, Fig. 5.14c shows a light spring with three coils that has been generated by a $\mathrm{LG}_{2,0}^{\omega\,\circlearrowleft} \oplus \mathrm{LG}_{1,0}^{2\omega\,\circlearrowright}$ superposition. The illustrations of the temporal evolution clearly indicate that its shape strongly depends on the incoming LG beams, especially on the OAM. An interesting characteristic of these light springs is that we always observe three attosecond bursts per cycle of the near-infrared beam at every azimuthal position, potentially only delayed in time.

Let us now analyze the origin and shape of these light springs in more detail. In the left part of Fig. 5.15, we show the intensity distribution of the driving $\mathrm{LG}_{1,0}^{\omega\,\circlearrowleft} \oplus \mathrm{LG}_{1,0}^{2\omega\,\circlearrowright}$ beam near the focus and how the orientation of the local bicircular field changes along the azimuth. The black dot indicates the electric field at $t = 0$. The right part shows the modulus of the electric field as a function of time for different azimuthal angles. For $\varphi = 0$, the electric field is maximal at $t = 0$, which is also shown by the black dot in the left part at $\varphi = 0$. At different azimuthal angles the electric field will have different values at $t = 0$. This is also demonstrated by the fact that the position of the black dot in the Lissajous figure changes along the azimuth. As explained in Sec. 5.2.2 a change of φ_0 in the azimuthal direction

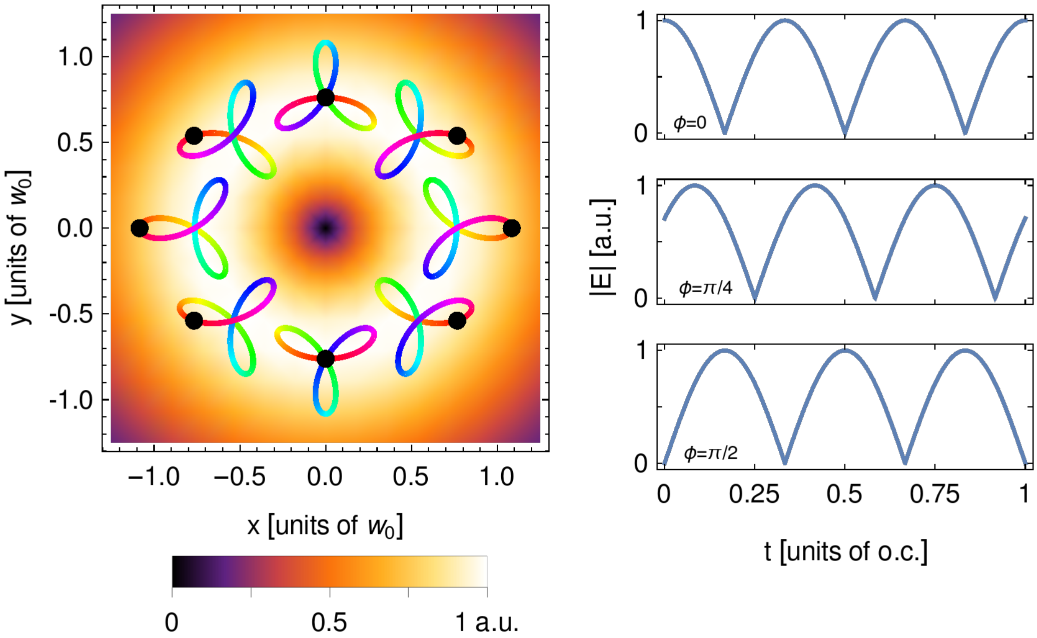

Figure 5.15: Left: Orientation of the Lissajous figures for various azimuthal angles φ in a bicircular LG beam ($LG^{\omega\circlearrowleft}_{1,0} + LG^{2\omega\circlearrowright}_{1,0}$) with the cycle averaged intensity distribution in the background. Right: Modulus of the electric field as a function of time at three different azimuthal positions.

causes a time shift of $\frac{\ell_1+\ell_2}{3\omega}\varphi_0$ in the time domain. Let us, for simplicity, assume that harmonics are only emitted when the modulus of the electric field is maximal. Generally, HHG with bicircular beams leads to three attosecond bursts per cycle, where the maxima of the bursts are separated in time by

$$\triangle t_{\text{burst}} = \frac{T}{3} = \frac{2\pi}{3\omega}. \tag{5.30}$$

If we change the azimuthal angle in a $LG^{\omega\circlearrowleft}_{1,0} \oplus LG^{2\omega\circlearrowright}_{1,0}$ superposition by 2π, we get a time shift of

$$\triangle t^{(1,1)}_{\text{azimuth}} = \tau \cdot 2\pi = \frac{2}{3\omega} \cdot 2\pi, \tag{5.31}$$

where $\tau = \frac{2}{3\omega}$, c.f. Eq. 5.11. There will be exactly two maxima along the azimuth, since

$$\frac{\triangle t^{(1,1)}_{\text{azimuth}}}{\triangle t_{\text{burst}}} = 2. \tag{5.32}$$

At these two maxima attosecond pulses are simultaneously emitted. This ensures that the light spring has two coils.

Similar to Fig. 5.15, we show the local orientation of the bicircular field of a

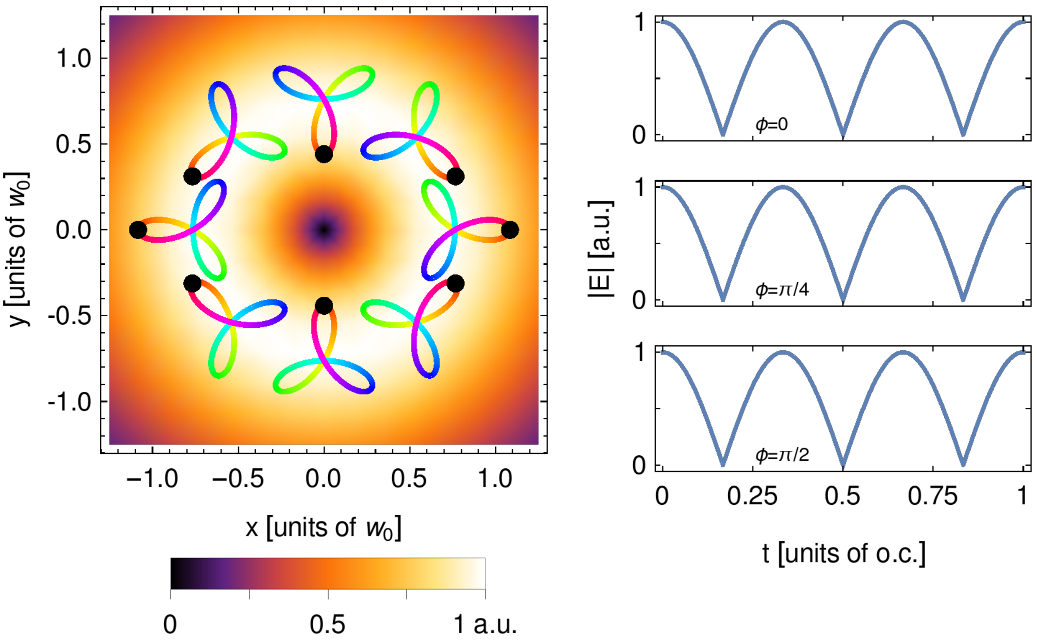

Figure 5.16: Same as Fig. 5.15 but for a $\text{LG}^{\omega\,\circlearrowleft}_{1,0} + \text{LG}^{2\omega\,\circlearrowright}_{-1,0}$ superposition.

$\text{LG}^{\omega\,\circlearrowleft}_{1,0} \oplus \text{LG}^{2\omega\,\circlearrowright}_{-1,0}$ superposition in Fig. 5.16. Interestingly, at $t = 0$ the electric field is maximal at all azimuthal positions, even though the electric field vector is pointing in different directions. Here, the attosecond pulses are emitted simultaneously at all azimuthal positions. As a result, we observe the attosecond pulse trains at the detector without time delay between different azimuthal positions. Therefore the temporal evolution has the donut-like shape instead of a light spring, c.f. Fig. 5.14b. We can easily generalize these findings to $\text{LG}^{\omega\,\circlearrowleft}_{\ell_1,0} \oplus \text{LG}^{2\omega\,\circlearrowright}_{\ell_2,0}$ superpositions. Again, a change of the azimuthal coordinate of φ_0, causes a time shift in the driving field of $\frac{\ell_1+\ell_2}{3\omega}\varphi_0$. Thus a change of 2π induces a time shift of

$$\triangle t^{(\ell_1,\ell_2)}_{\text{azimuth}} = \frac{(\ell_1+\ell_2)}{3\omega}\cdot 2\pi. \tag{5.33}$$

The maxima of the driving field, respectively the maxima of the attosecond bursts are separated by

$$\triangle t_{\text{burst}} = \frac{2\pi}{3\omega}. \tag{5.34}$$

Therefore, there are always

$$\frac{\triangle t^{(\ell_1,\ell_2)}_{\text{azimuth}}}{\triangle t_{\text{burst}}} = \ell_1 + \ell_2 \tag{5.35}$$

maxima along the azimuth. Since each maximum corresponds to one coil in the light spring, we get $\ell_1 + \ell_2$ coils that form the temporal evolution of the high-harmonic signal.

6

SUMMARY AND CONCLUSIONS

In this summary, we will shortly mention the keystones of each chapter. However, we will put more emphasis on possible future work and how it relates to the results presented in this thesis.

We started with a theoretical description of light beams in Ch. 2. After a short introduction to plane waves, we considered Gaussian and LG beams, where the latter ones carry in addition to their SAM a well defined OAM. Moreover, we showed that both are solutions to the paraxial wave equation. For paraxial beams, OAM and SAM are simultaneously well defined. This unique property allows to find precise selection rules for the generation of high harmonics. However, there are also other classes of twisted light beams, such as Bessel beams [115]. These non-diffracting beams fulfill the full wave equation and they do not have a well defined OAM and SAM. Here only the total angular momentum, the sum of SAM and OAM, is well defined. Basically this implies that SAM and OAM are coupled to each other. Investigations of HHG with those Bessel beams will help to understand the transfer of SAM and OAM in nonlinear processes. In particular it shall be interesting to analyze for example the polarization, far-field intensity and phase profiles of the generated harmonics and how they are affected by experimentally accessible parameters such as the opening angle of the Bessel beam. These harmonics could be a new tool for light-matter interaction at the ultra fast time scale.

In Ch. 3 we presented the underlying theory for the analysis of HHG with twisted light beams. We mainly divided this chapter into two parts that address the microscopic and macroscopic side of HHG, respectively.

For the microscopic side, we began with some classical considerations of HHG including the well-known three step model. This simple picture is crucial and builds a great intuition to understand this process. We subsequently presented the so-called quantum mechanical Lewenstein model in the framework of the SFA and showed its relation to the classical picture.

Typically, the continuum states in the SFA are described by Volkov states, which describe an electron in the external laser field, while the Coulomb potential of the parent ion and magnetic (non-dipole) effects are neglected. We therefore developed general Volkov states for spatially structured light fields, such as Bessel and LG beams, in order to account for non-dipole contributions [116]. This might considerably affect the spin polarization of outgoing and returning electron wave packet, when twisted light fields are applied. It will be interesting to apply these Volkov states to HHG with LG beams and compare these results to those of the commonly used Lewenstein model. Here we hope to see some signature of the OAM in the generated harmonics even in the single atom regime.

Another point for improvements is the proper description of the electronic wave functions. Here, most studies apply analytical, hydrogenic single-electron wave functions. It will be interesting to explore how the spectra of the emitted harmonics are affected if realistic orbital wave functions from many-electron approaches are applied. An implementation in the framework of JAC, the *Jena Atomic Calculator*, shall be realized soon [117].

In order to take the macroscopic side of HHG into account, we introduced two different models that consider the superposition of all single atom contributions to HHG at the detector. The first, simpler, model is based on the Fraunhofer diffraction formula. It can be used to approximate a very thin layer of atomic targets parallel to the focus plane. The second model uses the numerical propagation of the emitted harmonic radiation and can be also applied to simulate three dimensional gas jets. This model also automatically takes care of longitudinal phase matching.

We then, in Ch. 4, applied the Lewenstein model in combination with the Fraunhofer diffraction model to linearly polarized LG beams. We first reproduced the known rules for the conservation of OAM, which briefly says that the OAM of a q^{th} harmonic equals q times the OAM of the incident beam. In addition, we introduced our photon diagrams and presented how the OAM of generated harmonics changes if a superposition of two different LG beams are used for the driving laser. We have also analyzed phase matching for linearly polarized LG beams, which has to fulfill two distinct tasks. First, phase matching, basically the summation of harmonic signals from atoms at different positions, in the azimuthal direction accounts for the phase profiles in the far-field that can be associated to the OAM of the harmonics. This has been discussed in the beginning of the chapter. Second, phase matching in longitudinal and transverse direction affects the conversion efficiency and helps to investigate whether harmonics from a certain extended gas target add up constructively or annihilate at the detector. Here, we distinguished between phase matching for short and long trajectories separately. We used a quantum orbit approach to calculate the dipole phase for short and long trajectories. Moreover, we also took the intrinsic phases, the Gouy and the focal phase, of the driving beam into account. In particular, we investigated how the OAM of the driving beam affects the coherence length. We generally found a decreased coherence length for the short trajectories for beams with OAM compared to Gaussian beams, which has been explained due to the increased phase shift of the Gouy phase across the focus. However, we also showed that the OAM of the driving beam can be adjusted such that the phase shift of the Gouy phase compensates the dipole phase for long trajectories behind the focus. This gives rise to a large coherence length for the long trajectories and may help to identify signatures of these trajectories in HHG, potentially also beyond the near-infrared regime.

For further studies, these predictions could be supported by calculations with experiment-like three dimensional targets, for example gas jets. Here the harmonic signal can be computed for different positions of the gas jet with respect to the focus of the beam. This might help to understand phase matching in more detail.

For even higher intensities than those studied in this thesis, ionization and dispersive effects due to free charges have to be considered as well. For example, a highly ionized gas forms a plasma. Since the beams intensity distribution is not uniform, the plasma density will also be spatially dependent. Of course, the plasma density reaches its highest value near the intensity maximum of the beam. Moreover, the index of refraction will change according to the plasma density. In further studies, it should be analyzed how this plasma affects the conversion efficiency in HHG with OAM carrying beams.

At the end of Ch. 4 we presented three ways to enhance control over the OAM in HHG with superpositions of linearly polarized LG beams. We showed, for example that given harmonics can carry multiple values of OAM and that the harmonics can be spatially separated at the detector with respect to their OAM. However, there are still other possible scenarios to manipulate the generated harmonics. For example, a collinear superposition $\mathrm{LG}_{0,0}^{\omega\,\leftrightarrow} \oplus \mathrm{LG}_{2,0}^{2\omega\,\leftrightarrow}$ should give rise to radially varying OAM in the far-field.

In Ch. 5 we investigated HHG with bicircular beams. These beams are a superposition of a circularly polarized beam with its counter-rotating second harmonic. In a short discussion about the single atom response, we showed that every third harmonic is suppressed, while the remaining harmonics exhibit alternatingly left and right circular polarization. We then investigated how the OAM of the circularly polarized driving field components is transferred to the generated harmonics. Here, we found simple selections rules to explain HHG with bicircular LG beams. These selection rules demonstrate that the OAM of each harmonic is exactly determined by the OAM of the incident beams. Moreover, we proved that and how we can utilize the OAM of the incident beams to precisely tailor the OAM of the harmonics to an arbitrary integer. After a detailed analysis of the conservation of OAM in $\omega - 2\omega$ bicircular LG beams, we generalized our findings to $r\omega - s\omega$ bicircular fields.

All these studies have been performed for ideal long and exactly circularly polarized beams. Generally, if HHG is performed with few cycle driving pulses, the harmonic spectrum smears out, which is an immediate consequence of the Heisenberg's uncertainty principle. This implies that for HHG with few cycle bicircular pulses also frequencies occur in the harmonic spectrum that are absent for long driving beams. Here future studies may reveal how the OAM is transferred to these initially forbidden harmonics. It can be expected that these harmonics would not be pure LG modes, with a well defined ℓ, but are a superposition of different LG modes. Moreover, we expect a depolarization of the initially purely circularly polarized harmonics, similar to a recent publication that considered plane wave beams [92].

Another way to disturb the symmetry of long, exactly circularly polarized beams is to change the polarization from circular to slightly elliptical. HHG for bichromatic elliptical beams without OAM has been experimentally analyzed by Fleischer *et al.* [99] and theoretically investigated by Milošević [118]. Two main differences to HHG with bicircular beams have been found. First, no harmonics are suppressed and second there are several possible pathways leading to each harmonic order. Therefore it is promising to investigate the conservation OAM in HHG with bichromatic elliptical LG beams and its intensity distributions in the far-field. Moreover, the OAM affects the divergence of the generated harmonics. This might open up new possibilities to control the generated attosecond pulses. In Sec. 5.5, we discussed two ways to generate (near-)circularly polarized attosecond pulses. The first, which was proposed by Dorney *et al.* [66], takes advantage of the fact that the divergence of the harmonics increases with their OAM. If, for instance, left circularly polarized harmonics have significantly smaller OAM than the right circularly polarized harmonics, they will be separated at the detector by their divergence. In this sense, significantly means that the OAM of neighboring harmonics should differ by at least three. Within the second approach, we varied the intensity ratio between the two circularly polarized drivers to generate circularly polarized attosecond pulse trains. Here, we found in addition a rich annular structure in the far-field intensity profiles, c.f. Fig. 5.12c. A similar annular structure has been reported in HHG with linearly polarized LG beams by Genéaux *et al.* [110], which has been explained by the interplay of short and long trajectories in HHG. Moreover, they showed that it is possible to control this annular structure by a displacement of the atomic target with respect to the focus plane. Here we suggest to investigate this annular profile by an analysis of quantum orbits in bicircular fields [112].

Finally, we discussed the temporal evolution of the high-harmonic signal generated by bicircular LG beams. Here we found that the temporal evolution gives rise to a structure of a so-called light spring. Moreover, we showed possibilities to control the shape of the light springs. In particular, the number of coils can be easily accessed by the OAM of the driving beams.

BIBLIOGRAPHY

---

[1] P. Brookmann. “A Horse’s Motion Scientifically Determined.” In: *Scientific American* 39.16 (1878).

[2] C. E. Webb and J. D. C. Jones. *Handbook of laser technology and applications*. CRC Press, 2004, pp. 1919–1930. DOI: `10.1201/NOE0750309608`.

[3] P. F. Moulton. “Spectroscopic and laser characteristics of Ti:Al_2O_3.” In: *Journal of the Optical Society of America B* 3.1 (Jan. 1986), p. 125. DOI: `10.1364/JOSAB.3.000125`.

[4] Encyclopaedia Britannica. *History of the motion*. URL: `https://www.britannica.com/art/history-of-the-motion-picture/images-videos#/media/1/394161/38217`.

[5] A. McPherson et al. “Studies of multiphoton production of vacuum-ultraviolet radiation in the rare gases.” In: *Journal of the Optical Society of America B* 4.4 (Apr. 1987), p. 595. DOI: `10.1364/JOSAB.4.000595`.

[6] M. Ferray et al. “Multiple-harmonic conversion of 1064 nm radiation in rare gases.” In: *Journal of Physics B: Atomic, Molecular and Optical Physics* 21.3 (Feb. 1988), pp. L31–L35. DOI: `10.1088/0953-4075/21/3/001`.

[7] X. F. Li et al. “Multiple-harmonic generation in rare gases at high laser intensity.” In: *Physical Review A* 39.11 (June 1989), pp. 5751–5761. DOI: `10.1103/PhysRevA.39.5751`.

[8] P. B. Corkum. “Plasma perspective on strong field multiphoton ionization.” In: *Physical Review Letters* 71.13 (Sept. 1993), pp. 1994–1997. DOI: `10.1103/PhysRevLett.71.1994`.

[9] M. Lewenstein et al. “Theory of high-harmonic generation by low-frequency laser fields.” In: *Physical Review A* 49.3 (Mar. 1994), pp. 2117–2132. DOI: `10.1103/PhysRevA.49.2117`.

[10] M. Hentschel et al. “Attosecond metrology.” In: *Nature* 414.6863 (Nov. 2001), pp. 509–513. DOI: `10.1038/35107000`.

[11] P. Antoine, A. L’Huillier, and M. Lewenstein. “Attosecond Pulse Trains Using High–Order Harmonics.” In: *Physical Review Letters* 77.7 (Aug. 1996), pp. 1234–1237. DOI: `10.1103/PhysRevLett.77.1234`.

[12] P. M. Paul et al. “Observation of a train of attosecond pulses from high harmonic generation.” In: *Science (New York, N.Y.)* 292.5522 (June 2001), pp. 1689–92. DOI: `10.1126/science.1059413`.

[13] T. Popmintchev et al. “Bright Coherent Ultrahigh Harmonics in the keV X-ray Regime from Mid-Infrared Femtosecond Lasers.” In: *Science* 336.6086 (June 2012), pp. 1287–1291. DOI: `10.1126/science.1218497`.

[14] P. B. Corkum and F. Krausz. “Attosecond science.” In: *Nature Physics 2007 3:6* 3.6 (June 2007), p. 381. DOI: `10.1038/nphys620`.

[15] J. Itatani et al. “Attosecond Streak Camera.” In: *Physical Review Letters* 88.17 (Apr. 2002), p. 173903. DOI: `10.1103/PhysRevLett.88.173903`.

[16] D. Kielpinski. “Electrons on a winning streak.” In: *Nature Photonics* 8.1 (Jan. 2014), pp. 5–6. DOI: `10.1038/nphoton.2013.352`.

[17] B. Böning, W. Paufler, and S. Fritzsche. “Attosecond streaking with twisted X waves and intense infrared pulses.” In: *Physical Review A* 96.4 (Oct. 2017), p. 043423. DOI: `10.1103/PhysRevA.96.043423`.

[18] D. D. Hickstein et al. “Non-collinear generation of angularly isolated circularly polarized high harmonics.” In: *Nature Photonics* 9.11 (Nov. 2015), pp. 743–750. DOI: `10.1038/nphoton.2015.181`.

[19] O. Kfir et al. “Generation of bright phase-matched circularly-polarized extreme ultraviolet high harmonics.” In: *Nature Photonics* 9.2 (Feb. 2015), pp. 99–105. DOI: `10.1038/nphoton.2014.293`.

[20] P.-C. Huang et al. “Realization of Polarization Control in High-Order Harmonic Generation.” In: *IEEE Journal of Selected Topics in Quantum Electronics* 25.4 (July 2019), pp. 1–12. DOI: `10.1109/JSTQE.2019.2919777`.

[21] P. Lebedew. “Untersuchungen über die Druckkräfte des Lichtes.” In: *Annalen der Physik* 311.11 (Jan. 1901), pp. 433–458. DOI: `10.1002/andp.19013111102`.

[22] E. F. Nichols et al. “The Pressure due to Radiation.” In: *The Astrophysical Journal* 17 (June 1903), p. 315. DOI: `10.1086/141035`.

[23] J. H. Poynting. “The Wave Motion of a Revolving Shaft, and a Suggestion as to the Angular Momentum in a Beam of Circularly Polarised Light.” In: *Proceedings of the Royal Society A: Mathematical, Physical and Engineering Sciences* 82.557 (July 1909), pp. 560–567. DOI: `10.1098/rspa.1909.0060`.

[24] A. H. S. Holbourn. “Angular Momentum of Circularly Polarised Light.” In: *Nature* 137.3453 (Jan. 1936), pp. 31–31. DOI: `10.1038/137031a0`.

[25] R. A. Beth. "Direct Detection of the Angular Momentum of Light." In: *Physical Review* 48.5 (Sept. 1935), pp. 471–471. DOI: `10.1103/PhysRev.48.471`.

[26] R. A. Beth. "Mechanical Detection and Measurement of the Angular Momentum of Light." In: *Physical Review* 50.2 (July 1936), pp. 115–125. DOI: `10.1103/PhysRev.50.115`.

[27] L. Allen et al. "Orbital angular momentum of light and the transformation of Laguerre-Gaussian laser modes." In: *Physical Review A* 45.11 (June 1992), pp. 8185–8189. DOI: `10.1103/PhysRevA.45.8185`.

[28] M. S. Soskin et al. "Topological charge and angular momentum of light beams carrying optical vortices." In: *Physical Review A* 56.5 (Nov. 1997), pp. 4064–4075. DOI: `10.1103/PhysRevA.56.4064`.

[29] M. Beijersbergen et al. "Helical-wavefront laser beams produced with a spiral phaseplate." In: *Optics Communications* 112.5-6 (Dec. 1994), pp. 321–327. DOI: `10.1016/0030-4018(94)90638-6`.

[30] H. M. Scholz-Marggraf et al. "Absorption of twisted light by hydrogenlike atoms." In: *Physical Review A* 90.1 (July 2014), p. 013425. DOI: `10.1103/PhysRevA.90.013425`.

[31] R. A. Müller et al. "Photoionization of neutral atoms by X waves carrying orbital angular momentum." In: *Physical Review A* 94.4 (Oct. 2016), p. 041402. DOI: `10.1103/PhysRevA.94.041402`.

[32] C. T. Schmiegelow et al. "Transfer of optical orbital angular momentum to a bound electron." In: *Nature Communications* 7.1 (Dec. 2016), p. 12998. DOI: `10.1038/ncomms12998`.

[33] D. Seipt et al. "Two-color above-threshold ionization of atoms and ions in XUV Bessel beams and intense laser light." In: *Physical Review A* 94.5 (Nov. 2016), p. 053420. DOI: `10.1103/PhysRevA.94.053420`.

[34] B. Baghdasaryan et al. "Dichroism in two-color above-threshold ionization with twisted XUV beams and intense infrared laser fields." In: *Physical Review A* 99.2 (Feb. 2019), p. 023403. DOI: `10.1103/PhysRevA.99.023403`.

[35] T. Kuga et al. "Novel Optical Trap of Atoms with a Doughnut Beam." In: *Physical Review Letters* 78.25 (June 1997), pp. 4713–4716. DOI: `10.1103/PhysRevLett.78.4713`.

[36] M. P. J. Lavery et al. "Detection of a spinning object using light's orbital angular momentum." In: *Science (New York, N.Y.)* 341.6145 (Aug. 2013), pp. 537–40. DOI: `10.1126/science.1239936`.

[37] J. Wang et al. “Terabit free-space data transmission employing orbital angular momentum multiplexing.” In: *Nature Photonics* 6.7 (July 2012), pp. 488–496. DOI: `10.1038/nphoton.2012.138`.

[38] J. C. Maxwell. “{VIII}. A dynamical theory of the electromagnetic field.” In: *Philosophical Transactions of the Royal Society of London* 155 (1865), pp. 459–512. DOI: `10.1098/rstl.1865.0008`.

[39] L. Gouy. *Sur une propriete nouvelle des ondes lumineuses*. Paris: Gauthier-Villars, 1890.

[40] Z. Chang. *Fundamentals of attosecond optics*. Vol. 1. 2011. DOI: `10.1201/b10402`.

[41] A. M. Yao and M. J. Padgett. “Orbital angular momentum: origins, behavior and applications.” In: *Advances in Optics and Photonics* 3.2 (June 2011), p. 161. DOI: `10.1364/AOP.3.000161`.

[42] M. J. Padgett et al. “Divergence of an orbital-angular-momentum-carrying beam upon propagation.” In: *New Journal of Physics* 17.2 (Feb. 2015), p. 023011. DOI: `10.1088/1367-2630/17/2/023011`.

[43] N. H. Burnett et al. “Harmonic generation in CO2 laser target interaction.” In: *Applied Physics Letters* 31.3 (Aug. 1977), pp. 172–174. DOI: `10.1063/1.89628`.

[44] J. L. Krause, K. J. Schafer, and K. C. Kulander. “High-order harmonic generation from atoms and ions in the high intensity regime.” In: *Physical Review Letters* 68.24 (June 1992), pp. 3535–3538. DOI: `10.1103/PhysRevLett.68.3535`.

[45] S. Ghimire and D. A. Reis. *High-harmonic generation from solids*. 2019. DOI: `10.1038/s41567-018-0315-5`.

[46] S. Ghimire et al. “Observation of high-order harmonic generation in a bulk crystal.” In: *Nature Physics* 7.2 (Feb. 2011), pp. 138–141. DOI: `10.1038/nphys1847`.

[47] L. V. Keldysh. “Journal of Experimental and Theoretical Physics.” In: *JETP* 20.5 (1965), p. 1307.

[48] G. G. Paulus et al. “Plateau in above threshold ionization spectra.” In: *Physical Review Letters* 72.18 (May 1994), pp. 2851–2854. DOI: `10.1103/PhysRevLett.72.2851`.

[49] G. G. Paulus et al. “Rescattering effects in above-threshold ionization: a classical model.” In: *Journal of Physics B: Atomic, Molecular and Optical Physics* 27.21 (Nov. 1994), pp. L703–L708. DOI: `10.1088/0953-4075/27/21/003`.

[50] A. L'Huillier et al. "Multiply Charged Ions Formed by Multiphoton Absorption Processes in the Continuum." In: *Physical Review Letters* 48.26 (June 1982), pp. 1814–1817. DOI: `10.1103/PhysRevLett.48.1814`.

[51] A. L'Huillier et al. "Multiply charged ions induced by multiphoton absorption in rare gases at 0.53 µm." In: *Physical Review A* 27.5 (May 1983), pp. 2503–2512. DOI: `10.1103/PhysRevA.27.2503`.

[52] W. Becker et al. "Above-threshold ionization: From classical features to quantum effects." In: *ADVANCES IN ATOMIC, MOLECULAR, AND OPTICAL PHYSICS* 48 (2002), pp. 35–98.

[53] G. Vampa and T. Brabec. "Merge of high harmonic generation from gases and solids and its implications for attosecond science." In: *Journal of Physics B: Atomic, Molecular and Optical Physics* 50.8 (Apr. 2017), p. 083001. DOI: `10.1088/1361-6455/aa528d`.

[54] G. L. Yudin and M. Y. Ivanov. "Nonadiabatic tunnel ionization: Looking inside a laser cycle." In: *Physical Review A* 64.1 (June 2001), p. 013409. DOI: `10.1103/PhysRevA.64.013409`.

[55] A. N. Pfeiffer et al. "Attoclock reveals natural coordinates of the laser-induced tunnelling current flow in atoms." In: *Nature Physics* 8.1 (Jan. 2012), pp. 76–80. DOI: `10.1038/nphys2125`.

[56] M. Ammosov, N. Delone, and V. Krainov. "Journal of Experimental and Theoretical Physics." In: *JETP* 64.6 (1986), p. 1191.

[57] S. Patchkovskii and H. Muller. "Simple, accurate, and efficient implementation of 1-electron atomic time-dependent Schrödinger equation in spherical coordinates." In: *Computer Physics Communications* 199 (Feb. 2016), pp. 153–169. DOI: `10.1016/J.CPC.2015.10.014`.

[58] V. Mosert and D. Bauer. "Photoelectron spectra with Qprop and t-SURFF." In: *Computer Physics Communications* 207 (Oct. 2016), pp. 452–463. DOI: `10.1016/J.CPC.2016.06.015`.

[59] V. Tulsky and D. Bauer. "QPROP with faster calculation of photoelectron spectra." In: (July 2019).

[60] N. Bleistein and R. A. Handelsman. *Asymptotic expansions of integrals*. Courier Corporation, 1986.

[61] D. B. Milosević, D. Bauer, and W. Becker. "Quantum-orbit theory of high-order atomic processes in intense laser fields." In: *Journal of Modern Optics* 53.1-2 (Jan. 2006), pp. 125–134. DOI: `10.1080/09500340500186099`.

[62] M. B. Gaarde et al. “Spatiotemporal separation of high harmonic radiation into two quantum path components.” In: *Physical Review A* 59.2 (Feb. 1999), pp. 1367–1373. DOI: 10.1103/PhysRevA.59.1367.

[63] P. Salières et al. “Feynman’s path-integral approach for intense-laser-atom interactions.” In: *Science* 292.5518 (May 2001), pp. 902–905. DOI: 10.1126/science.108836.

[64] L. Rego et al. “Ultrashort Extreme Ultraviolet Vortices.” In: *Vortex Dynamics and Optical Vortices*. InTech, Mar. 2017. DOI: 10.5772/64908.

[65] C. Hernández-García et al. “Quantum-path signatures in attosecond helical beams driven by optical vortices.” In: *New Journal of Physics* 17.9 (Sept. 2015), p. 093029. DOI: 10.1088/1367-2630/17/9/093029.

[66] K. M. Dorney et al. “Controlling the polarization and vortex charge of attosecond high-harmonic beams via simultaneous spin–orbit momentum conservation.” In: *Nature Photonics* 13.2 (Feb. 2019), pp. 123–130. DOI: 10.1038/s41566-018-0304-3.

[67] M. Born and E. Wolf. *Principles of optics: electromagnetic theory of propagation, interference and diffraction of light*. Elsevier Science, 2013.

[68] C. Hernández-García et al. “High-order harmonic propagation in gases within the discrete dipole approximation.” In: *Physical Review A* 82.3 (Sept. 2010), p. 033432. DOI: 10.1103/PhysRevA.82.033432.

[69] C. Hernández-García et al. “Attosecond extreme ultraviolet vortices from high-order harmonic generation.” In: *Physical Review Letters* 111.8 (Aug. 2013), pp. 1–5. DOI: 10.1103/PhysRevLett.111.083602.

[70] E. Pisanty. “Electron dynamics in complex time and complex space.” PhD thesis. Imperial College London, 2016. DOI: 10.25560/43538.

[71] M. Zürch et al. “Strong-field physics with singular light beams.” In: *Nature Physics* 8.10 (Oct. 2012), pp. 743–746. DOI: 10.1038/nphys2397.

[72] Y. Toda, S. Honda, and R. Morita. “Dynamics of a paired optical vortex generated by second-harmonic generation.” In: *Optics Express* 18.17 (Aug. 2010), p. 17796. DOI: 10.1364/OE.18.017796.

[73] G. Gariepy et al. “Creating High-Harmonic Beams with Controlled Orbital Angular Momentum.” In: *Physical Review Letters* 113.15 (Oct. 2014), p. 153901. DOI: 10.1103/PhysRevLett.113.153901.

[74] N. M. Temme. *Special functions : An introduction to the classical functions of mathematical physics*. 1996, p. 374. DOI: 10.1002/9781118032572.

[75] P. Salières, A. L'Huillier, and M. Lewenstein. "Coherence Control of High-Order Harmonics." In: *Physical Review Letters* 74.19 (May 1995), pp. 3776–3779. DOI: 10.1103/PhysRevLett.74.3776.

[76] P. Balcou et al. "Generalized phase-matching conditions for high harmonics: The role of field-gradient forces." In: *Physical Review A* 55.4 (Apr. 1997), pp. 3204–3210. DOI: 10.1103/PhysRevA.55.3204.

[77] M. B. Gaarde, J. L. Tate, and K. J. Schafer. "Macroscopic aspects of attosecond pulse generation." In: *Journal of Physics B: Atomic, Molecular and Optical Physics* 41.13 (July 2008), p. 132001. DOI: 10.1088/0953-4075/41/13/132001.

[78] P. Ye et al. "Minimizing the angular divergence of high-order harmonics by truncating the truncated Bessel beam." In: *Physical Review A* 90.6 (Dec. 2014), p. 063808. DOI: 10.1103/PhysRevA.90.063808.

[79] M. Lewenstein, P. Salières, and A. L'Huillier. "Phase of the atomic polarization in high-order harmonic generation." In: *Physical Review A* 52.6 (Dec. 1995), pp. 4747–4754. DOI: 10.1103/PhysRevA.52.4747.

[80] M. B. Gaarde and K. J. Schafer. "Quantum path distributions for high-order harmonics in rare gas atoms." In: *Physical Review A* 65.3 (Mar. 2002), p. 031406. DOI: 10.1103/PhysRevA.65.031406.

[81] L. G. Gouy. "Sur la propagation anomale des ondes." In: *Compt. Rendue Acad. Sci. Paris* 111 (1890), p. 33.

[82] M. A. Porras. "Characterization of the electric field of focused pulsed Gaussian beams for phase-sensitive interactions with matter." In: *Optics Letters* 34.10 (May 2009), p. 1546. DOI: 10.1364/OL.34.001546.

[83] F. Lindner et al. "High-order harmonic generation at a repetition rate of 100 kHz." In: *Physical Review A* 68.1 (July 2003), p. 013814. DOI: 10.1103/PhysRevA.68.013814.

[84] W. Paufler, B. Böning, and S. Fritzsche. "Coherence control in high-order harmonic generation with Laguerre-Gaussian beams." In: *Physical Review A* 100.1 (July 2019), p. 013422. DOI: 10.1103/PhysRevA.100.013422.

[85] L. Chipperfield et al. "Tracking individual electron trajectories in a high harmonic spectrum." In: *Optics Communications* 264.2 (Aug. 2006), pp. 494–501. DOI: 10.1016/J.OPTCOM.2006.03.078.

[86] L. Rego et al. "Nonperturbative twist in the generation of extreme-ultraviolet vortex beams." In: *Physical Review Letters* 117.16 (Oct. 2016), p. 163202. DOI: 10.1103/PhysRevLett.117.163202.

[87] F. Kong et al. “Controlling the orbital angular momentum of high harmonic vortices.” In: *Nature Communications* 8 (Apr. 2017), p. 14970. DOI: 10.1038/ncomms14970.

[88] D. Gauthier et al. “Tunable orbital angular momentum in high-harmonic generation.” In: *Nature Communications* 8 (Apr. 2017), p. 14971. DOI: 10.1038/ncomms14971.

[89] C. Lux et al. “Photoelectron circular dichroism observed in the above-threshold ionization signal from chiral molecules with femtosecond laser pulses.” In: *Journal of Physics B: Atomic, Molecular and Optical Physics* 49.2 (Jan. 2016), 02LT01. DOI: 10.1088/0953-4075/49/2/02LT01.

[90] C. A. Mancuso et al. “Strong-field ionization with two-color circularly polarized laser fields.” In: *Physical Review A* 91.3 (Mar. 2015), p. 031402. DOI: 10.1103/PhysRevA.91.031402.

[91] S. Eckart et al. “Nonsequential Double Ionization by Counterrotating Circularly Polarized Two-Color Laser Fields.” In: *Physical Review Letters* 117.13 (Sept. 2016), p. 133202. DOI: 10.1103/PhysRevLett.117.133202.

[92] L. Barreau et al. “Evidence of depolarization and ellipticity of high harmonics driven by ultrashort bichromatic circularly polarized fields.” In: *Nature Communications* 9.1 (2018). DOI: 10.1038/s41467-018-07151-8.

[93] M. V. Frolov et al. “Control of Harmonic Generation by the Time Delay between Two-Color, Bicircular Few-Cycle Mid-IR Laser Pulses.” In: *Physical Review Letters* 120.26 (2018). DOI: 10.1103/PhysRevLett.120.263203.

[94] D. B. Milošević. “Control of the helicity of high-order harmonics generated by bicircular laser fields.” In: *Physical Review A* 98.3 (Sept. 2018), p. 033405. DOI: 10.1103/PhysRevA.98.033405.

[95] M. Busuladžić, A. Gazibegović-Busuladžić, and D. B. Milošević. “Strong-field ionization of homonuclear diatomic molecules by a bicircular laser field: Rotational and reflection symmetries.” In: *Physical Review A* 95.3 (Mar. 2017), p. 033411. DOI: 10.1103/PhysRevA.95.033411.

[96] A. Jiménez-Galán et al. “Time-resolved high harmonic spectroscopy of dynamical symmetry breaking in bi-circular laser fields: the role of Rydberg states.” In: *Optics Express* 25.19 (Sept. 2017), p. 22880. DOI: 10.1364/OE.25.022880.

[97] E. Pisanty et al. “Conservation of Torus-knot Angular Momentum in High-order Harmonic Generation.” In: *Physical Review Letters* 122.20 (May 2019), p. 203201. DOI: 10.1103/PhysRevLett.122.203201.

[98] D. B. Milošević, W. Becker, and R. Kopold. "Generation of circularly polarized high-order harmonics by two-color coplanar field mixing." In: *Physical Review A* 61.6 (May 2000), p. 063403. DOI: `10.1103/PhysRevA.61.063403`.

[99] A. Fleischer et al. "Spin angular momentum and tunable polarization in high-harmonic generation." In: *Nature Photonics* 8.7 (July 2014), pp. 543–549. DOI: `10.1038/nphoton.2014.108`.

[100] W. Paufler, B. Böning, and S. Fritzsche. "High harmonic generation with Laguerre–Gaussian beams." In: *Journal of Optics* 21.9 (Sept. 2019), p. 094001. DOI: `10.1088/2040-8986/ab31c3`.

[101] W. Paufler, B. Böning, and S. Fritzsche. "Tailored orbital angular momentum in high-order harmonic generation with bicircular Laguerre-Gaussian beams." In: *Physical Review A* 98.1 (July 2018), pp. 1–5. DOI: `10.1103/PhysRevA.98.011401`.

[102] W. Paufler, B. Böning, and S. Fritzsche. "Strong-field ionization with twisted laser pulses." In: *Physical Review A* 97.4 (Apr. 2018), p. 043418. DOI: `10.1103/PhysRevA.97.043418`.

[103] J. Wolfart. *Einführung in die Zahlentheorie und Algebra*. Wiesbaden: Vieweg + Teubner, 2011. DOI: `10.1007/978-3-8348-9833-3`.

[104] I. P. Christov, M. M. Murnane, and H. C. Kapteyn. "High-Harmonic Generation of Attosecond Pulses in the "Single-Cycle" Regime." In: *Physical Review Letters* 78.7 (Feb. 1997), pp. 1251–1254. DOI: `10.1103/PhysRevLett.78.1251`.

[105] P. Agostini and L. F. DiMauro. "The physics of attosecond light pulses." In: *Reports on Progress in Physics* 67.6 (June 2004), pp. 813–855. DOI: `10.1088/0034-4885/67/6/R01`.

[106] C. A. Mancuso et al. "Controlling electron-ion rescattering in two-color circularly polarized femtosecond laser fields." In: *Physical Review A* 93.5 (May 2016), p. 053406. DOI: `10.1103/PhysRevA.93.053406`.

[107] C. A. Mancuso et al. "Controlling Nonsequential Double Ionization in Two-Color Circularly Polarized Femtosecond Laser Fields." In: *Physical Review Letters* 117.13 (Sept. 2016), p. 133201. DOI: `10.1103/PhysRevLett.117.133201`.

[108] K. M. Dorney et al. "Helicity-Selective Enhancement and Polarization Control of Attosecond High Harmonic Waveforms Driven by Bichromatic Circularly Polarized Laser Fields." In: *Physical Review Letters* 119.6 (Aug. 2017), p. 063201. DOI: `10.1103/PhysRevLett.119.063201`.

[109] A. Jiménez-Galán et al. "Control of attosecond light polarization in two-color bicircular fields." In: *Physical Review A* 97.2 (Feb. 2018), p. 023409. DOI: `10.1103/PhysRevA.97.023409`.

[110] R. Géneaux et al. "Radial index of Laguerre-Gaussian modes in high-order-harmonic generation." In: *Physical Review A* 95.5 (May 2017), p. 051801. DOI: `10.1103/PhysRevA.95.051801`.

[111] A. Zaïr et al. "Quantum Path Interferences in High-Order Harmonic Generation." In: *Physical Review Letters* 100.14 (Apr. 2008), p. 143902. DOI: `10.1103/PhysRevLett.100.143902`.

[112] D. B. Milošević. "Quantum-orbit analysis of high-order harmonic generation by bicircular field." In: *Journal of Modern Optics* 66.1 (Jan. 2019), pp. 47–58. DOI: `10.1080/09500340.2018.1511862`.

[113] M. A. Porras. "Attosecond helical pulses." In: *Physical Review A* 100.3 (Sept. 2019), p. 033826. DOI: `10.1103/PhysRevA.100.033826`.

[114] G. Pariente and F. Quéré. "Spatio-temporal light springs: extended encoding of orbital angular momentum in ultrashort pulses." In: *Optics Letters* 40.9 (May 2015), p. 2037. DOI: `10.1364/OL.40.002037`.

[115] J. Durnin, J. J. Miceli, and J. H. Eberly. "Diffraction-free beams." In: *Physical Review Letters* 58.15 (Apr. 1987), pp. 1499–1501. DOI: `10.1103/PhysRevLett.58.1499`.

[116] B. Böning, W. Paufler, and S. Fritzsche. "Nondipole strong-field approximation for spatially structured laser fields." In: *Physical Review A* 99.5 (May 2019), p. 053404. DOI: `10.1103/PhysRevA.99.053404`.

[117] S. Fritzsche. "A fresh computational approach to atomic structures, processes and cascades." In: *Computer Physics Communications* (2019). DOI: `10.1016/j.cpc.2019.01.012`.

[118] D. B. Milošević. "High-order harmonic generation by a bichromatic elliptically polarized field: conservation of angular momentum." In: *Journal of Physics B: Atomic, Molecular and Optical Physics* 48.17 (Sept. 2015), p. 171001. DOI: `10.1088/0953-4075/48/17/171001`.

LIST OF FIGURES

Figure 1.1 Comparison of timescales . . . 2
Figure 1.2 Spiral phase plate . . . 3
Figure 2.1 Phase front and intensity profile of a plane wave . . . 8
Figure 2.2 Longitudinal geometry of a Gaussian beam . . . 10
Figure 2.3 Transverse intensity and phase profiles of LG beams . . . 11
Figure 2.4 Helical phase fronts . . . 12
Figure 3.1 Multiphoton and tunnel ionization . . . 17
Figure 3.2 Three step model . . . 18
Figure 3.3 Classical electron trajectories in a linearly polarized laser field 19
Figure 3.4 Classical return energies . . . 20
Figure 3.5 Photon energy from quantum orbits . . . 28
Figure 3.6 Geometry of the Fraunhofer diffraction formula . . . 31
Figure 3.7 Propagation of high-harmonic radiation . . . 32
Figure 4.1 Characteristic spectrum of HHG . . . 34
Figure 4.2 Suppression of even harmonics . . . 35
Figure 4.3 Far-field phase profiles for HHG with linearly polarized LG beams . . . 37
Figure 4.4 Far-field intensity profiles for HHG with linearly polarized LG beams . . . 39
Figure 4.5 Plane wave phase matching . . . 40
Figure 4.6 Longitudinal and transverse intensity profiles . . . 43
Figure 4.7 Dipole phase for the 21st harmonic . . . 44
Figure 4.8 Longitudinal and transverse phase profiles . . . 45
Figure 4.9 Total phase on maximum . . . 47
Figure 4.10 Coherence length on maximum . . . 49
Figure 4.11 Perfect phase matching on maximum . . . 50
Figure 4.12 Map of coherence length for 21st harmonic . . . 53
Figure 4.13 Map of coherence length for 35st harmonic . . . 54
Figure 4.14 OAM in non-perturbative HHG . . . 55
Figure 4.15 OAM in non-collinear HHG I . . . 56
Figure 4.16 OAM in non-collinear HHG II . . . 57
Figure 5.1 Composition of a bicircular field . . . 61
Figure 5.2 Bicircular field for various intensity ratios . . . 62

Figure 5.3 Rotational symmetry in bicircular fields 63
Figure 5.4 Lissajous figures in bicircular twisted beams 64
Figure 5.5 Characteristic spectrum of high harmonics from bicircular driving fields 65
Figure 5.6 Photon diagrams for HHG in bicircular fields 66
Figure 5.7 Far-field phase profiles for HHG with bicircular LG beams . . . 69
Figure 5.8 Far-field intensity profiles for HHG with bicircular LG beams . 70
Figure 5.9 Photon diagrams for HHG in bicircular LG beams 71
Figure 5.10 Visualization of general bicircular fields. 75
Figure 5.11 Intensity distributions of the generated harmonics for various combinations of OAM of the driving beams 76
Figure 5.12 Intensity distributions of the generated harmonics for various intensity ratios of the driving beams 77
Figure 5.13 Attosecond pulse train generated with a bicircular beam . . . 78
Figure 5.14 Light springs generated by HHG with bicircular twisted LG beams 79
Figure 5.15 Local electric field of $\mathrm{LG}_{1,0}^{\omega}{}^{\circlearrowleft} + \mathrm{LG}_{1,0}^{2\omega}{}^{\circlearrowright}$ beam 81
Figure 5.16 Local electric field of $\mathrm{LG}_{1,0}^{\omega}{}^{\circlearrowleft} + \mathrm{LG}_{-1,0}^{2\omega}{}^{\circlearrowright}$ beam 82

ACRONYMS

HHG	high-harmonic generation
SFA	strong-field approximation
OAM	orbital angular momentum
SAM	spin angular momentum
LG	Laguerre-Gaussian

PUBLICATIONS

The material presented in this thesis was contributed to the following publications:

Tailored orbital angular momentum in high-order harmonic generation with bicircular Laguerre-Gaussian beams
Paufler, W., Böning, B., Fritzsche, S.
PHYSICAL REVIEW A, **98**, 011401(R) (2018)

High harmonic generation with Laguerre–Gaussian beams
Paufler, W., Böning, B., Fritzsche, S.
Journal of Optics, **21**(9), 094001 (2019)

Coherence control in high-order harmonic generation with Laguerre-Gaussian beams
Paufler, W., Böning, B., Fritzsche, S.
PHYSICAL REVIEW A, **100**, 013422 (2019)

The following publications are not part of this thesis:

Attosecond streaking with twisted X waves and intense infrared pulses
Böning, B., Paufler, W., Fritzsche, S.
PHYSICAL REVIEW A, **96**, 043423 (2017)

Strong-field ionization with twisted laser pulses
Paufler, W., Böning, B., Fritzsche, S.
PHYSICAL REVIEW A, **97**, 043418 (2018)

Above-threshold ionization by few-cycle Bessel pulses
Böning, B., Paufler, W., Fritzsche, S.
PHYSICAL REVIEW A, **98**, 023407 (2018)

Dichroism in two-color above-threshold ionization with twisted XUV beams and intense infrared laser fields
Baghdasaryan, B., Böning, B., Paufler, W., Fritzsche, S.
PHYSICAL REVIEW A, **99**, 023403 (2019)

Nondipole strong-field approximation for spatially structured laser fields
Böning, B., Paufler, W., Fritzsche, S.
PHYSICAL REVIEW A, **99**, 053404 (2019)

Strong-Field Ionization with Few-Cycle Bessel Pulses: Interplay Between Orbital Angular Momentum and Carrier Envelope Phase
Paufler, W., Böning, B., Fritzsche, S.
Quantum Collisions and Confinement of Atomic and Molecular Species, and Photons, **Bd. 230**, 274-284 (2019)

EHRENWÖRTLICHE ERKLÄRUNG

Ich erkläre hiermit ehrenwörtlich, dass ich die vorliegende Arbeit selbstständing, ohne unzuässige Hilfe dritter und ohne Benutzung anderer als der angegebenen Hilfsmittel und Literatur angefertigt habe. Die aus anderen Quellen direkt oder indirekt übernommenen Daten und Konzepte sind unter Angabe der Quelle gekennzeichnet. Bei der Anfertigung dieser Arbeit haben mir meine Betreuer und die Koautoren oben genannter Publikationen geholfen.

Weitere Personen waren an der inhaltlich-materiellen Erstellung der vorliegenden Arbeit nicht beteiligt. Insbesondere habe ich hierfür nicht die entgeltliche Hilfe von Vermittlungs- bzw. Beratungsdiensten (Promotionsberater oder andere Personen) in Anspruch genommen.

Niemand hat von mir unmittelbar oder mittelbar geldwerte Leistungen für Arbeiten erhalten, die im Zusammenhang mit dem Inhalt der vorgelegten Dissertation stehen.

Die Arbeit wurde bisher weder im In- noch im Ausland in gleicher oder ähnlicher Form einer anderen Prüfungsbehörde vorgelegt.

Die geltende Promotionsordnung der Physikalisch-Astronomischen Fakultät ist mir bekannt.

Ich versichere ehrenwörtlich, dass ich nach bestem Wissen die reine Wahrheit gesagt und nichts verschwiegen habe.

Jena, 01. Juni 2020

Willi Paufler